Austenite Formation in Low Carbon Microalloyed Pipeline Steels

by

Alejandro Hintze Cesaro

A thesis submitted in partial fulfillment of the requirements for the degree of

Doctor of Philosophy

in

Materials Engineering

Department of Chemical and Materials Engineering
University of Alberta

Abstract

A study of the kinetic and microstructural aspects of austenite formation in low carbon pipeline steels during continuous heating and a model capable to predict the interface velocity are presented in this study. The overall goal of this work is to increase the level of understanding concerning the austenite reversion in low carbon pipeline steels. This work build on top of the theory of solute drag and a Gibbs energy balance approach, and expands this theory to account for the effect of Mn redistribution at slow heating rates.

Due to the unique characteristics of commercial pipeline steels, given by a refined chemical composition and tailored steel processing conditions, the initial microstructure previous to the austenite transformation was carefully studied to ponder all the relevant transformation conditions during continuous heating. Dilatometry experiments were employed to construct a continuous heating transformation (CHT) diagrams and study the kinetics and microstructural aspects of two commercial X80 pipeline steels.

Experimental results suggested that orthoequilibrium calculations are poor predictor of the transformation temperatures and that the mechanisms controlling the transformation kinetics are susceptible to the heating rate. To obtain a better understanding of the transformation kinetics, a Gibbs free energy balance across the interface was employed to calculate the boundary migration rate as a function of the available driving force. This energetic approach was supported by an original methodology to calculate the chemical driving force under paraequilibrium conditions coupled with a modification of the solute drag model. The calculation was applied for continuous heating transformation at 1 °C/s and 200 °C/s.

The results of this work serve to bring a deeper understanding on how austenite is formed during continuous heating. In particular to highlight the differences between slow (conventional heat treatments) and fast (welding) heating rates.

Preface

The materials presented in this thesis comprises the author's research project under the supervision of Dr. Patricio Mendez. This work has been founded by Natural Science and Engineering Research Council (NSERC) of Canada (CRD 507483, NSERC RGPIN-2019-05981 Mendez). Funding was also received from the AWS Foundation and the Roberto Rocca Education Program.

Chapter 2Effect of the heating rate on austenite formation in low carbon microalloyed steelschapter.2 of this work is published as Hintze Cesaro, A., and P. F. Mendez. "Effect of the heating rate on austenite formation during continuous heating on a grade X80 pipeline steel was studied." *Welding Journal* (2021). Alejandro Hintze Cesaro was responsible for conduction of analysis and composition of the paper. Dr. Patricio Mendez was the supervisory author. This article received the William Spraragen Memorial Award for the best research paper printed in the research supplement of the Welding Journal during the twelve-month period December 2020-2021.

Chapter 3Kinetics of austenization during heating accounting for solute drag and Mn redistributionchapter.3 of this work is to be submitted for publication as Hintze Cesaro, A., and P. F. Mendez. "Kinetics of austenization during heating accounting for solute drag and Mn redistribution". Alejandro Hintze Cesaro was responsible for conduction of analysis and composition of the paper. Dr. Patricio Mendez was the supervisory author.

Chapter 4Driving force for phase transformation of microalloyed steels under paraequilibrium conditionschapter.4 of this work is to be submitted for publication as Hintze Cesaro, A., and P. F. Mendez. "Driving Force for phase transformation of microalloyed steels under paraequilibrium conditions". Alejandro Hintze Cesaro was responsible for conduction of analysis and composition of the paper. Dr. Patricio Mendez was the supervisory author. The manuscript intended to submit is a slightly altered version from this chapter. Appendices AMatlab Code for the calculation of the chemical driving forceappendix.A and CMatlab code for the calculation of the Gibbs free energy of ferrite and austenite in a Z-C systemappendix.C are not included in the article intended to submit.

Chapter 5Models to predict hardness in the HAZchapter.5 of this work is published as Hintze Cesaro, A., and P. F. Mendez. "Models to predict hardness in the HAZ." Weld Magazine (2019). Alejandro Hintze Cesaro was responsible for the composition of the paper. Dr. Patricio Mendez was the supervisory author.

The format of this thesis is paper-based.

Acknowledgments

I would like to start thanking Dr. Patricio Mendez for giving me the opportunity to be a part of the Canadian Centre for Welding and Joining (CCWJ). During my time as a graduate student, Patricio guided and encouraged me throughout the course of this work. From his kindness and support, I learned not only about welding but also about core values such as respect, generosity and professionalism. It was my pleasure to work with him.

To Goetz Dapp, thank you for your constant help and sincerity. I also want to thank all my fellow graduate students, for all the time we spent together. I am grateful for all the friendships I made in the last five years.

To all the institutions and organizations that provided funding and support for my education. Specially to the AWS Foundation and the Roberto Rocca Education Program.

To Agnes Marie Perez, my life partner. Your love, support, and understanding during all these years were crucial to help me throughout all the difficulties and challenges of pursuing this degree.

Lastly, to my family, thank you so much for everything. Regardless the distance my mom, dad and sister have been always there supporting me. Without their love, effort, and understanding, I wouldn't have been able to achieve all my goals. I love you more than anything in my life.

Contents

List of Tables

List of Figures

Chapter 1

Introduction

1.1 Introduction

Mechanical properties such as hardness, toughness, tensile strength, etc. are determined by the resulting microstructure after any thermal cycle. During most of the heat treatments or welding processes, steels are subjected to a thermal cycle, which in their most generic form involves a heating cycle, which can implicate either a partial or full austenitization, followed by isothermal hold at a fixed temperature and finally a cooling stage, which will define the resulting microstructures and hence the mechanical properties.

Different microstructures are developed during the cooling stage as a result of the different cooling rates. However, is well known that the kinetics of phase transformation during cooling are strongly influenced by the parent phase. Metallurgical aspects such as precipitation and dissolution of second phases, grain coarsening of austenite, and austenite chemical homogeneity have a strong influence on the hardenability of the steel [1].

Although grain coarsening has been extensively studied, the previous condition for grain growth (i.e. characteristic features of the microstructure immediately after the complete transformation to austenite) is still subject to debate.

In particular, austenite formation upon heating in alloyed steels is a complex process that depends on the microstructural and chemical characteristics of the studied steels but also on the time available for transformation (i.e. heating rate).

Many studies have been conducted to study the austenite transformation from a initial ferritic and/or pearlitic initial microstructure [2–13] and a smaller number focused on an initial martensitic structure [9,14,15]. Finally, other authors focused the study on more complex microstructures, characteristics of thermomechanical processed microalloyed steels [16–18], especially on intercritical austenitization of dual phase (DP) steels [19–23]. Neverthe-

less, very little relevant works have been published specifically on austenitization kinetics of pipeline steels. Due to the complexity and influence of the initial microstructure on the austenite transformation, it is not trivial to extend previous works on the present studied material.

However, the work published up to date can help to understand and explain the kinetics of this solid-state transformation. Therefore, in the next section a small review on austenite formation is presented.

1.1.1 Literature Review

Nucleation of Austenite

Nehrenberg et al. [24] was one of the first to study the morphology of austenite during growth. According to their experimental observations, the authors categorized the moprphology of austenite at early stages of transformation into two different classes. In one case the austenite is said to have an "acicular" shape, in which the new formed grains have a marked direction growth. This type of morphology has been observed when austenite forms from a low temperature transformation products, such as martensite, bainite, or even tempered martensite. Supporting experimental evidence of this particular morphology has been reported by several authors [25–29]. Moreover, Kimmins et al. [27] suggested that the acicular morphology is responsible of the phenomena know as "austenite memory effect".

In the other case, when the initial microstructure is conformed by high temperature transformation products (such as ferrite, pearlite, or spherodized cementite), austenite grows freely in any direction resulting in an equiaxed morphology, usually referred as "globular" austenite.

The morphology of austenite not only depends on the initial microstructure and chemical composition, but also varies with the heating rate. An interest in the austenite transformation for steels with a potential for recrystallization (i.e. cold worked steels) resulted in several works published [10,25]. According to Azizi et al. [25], at low heating rates an extra stage of ferrite recrystallization and spherodization of pearlite lamellae occurs, and the newly formed austenite presents a "globular" morphology. However, the authors also reported that as the heating rate increases, the recrystallization and spherodizaiton process can be nullified or incomplete affecting the structure of the transformed austenite, resulting in "acicular" grains. On the other hand, Matsuda et al. [28] reported an opposite behavior, in which the proportion of "globular" austenite increases with the heating rate when the new phase is formed from a martensitic structure.

Besides the morphology of austenite, nucleation sites are also highly sensitive to the initial microstructure. In ferritic/ pearlitic structures, it has been reported that the austenite nucleates heterogeneously at pearlite/pearlite colony junctions or ferrite/pearlite boundaries [19, 20, 30–34]. Many authors remarked the importance of pearlite features (e.g. interlamellar spacing and the specific interface of pearlitic colonies) on the density for nucleation sites

and hence the pearlite dissolution kinetics [19, 30]. For a ferrite/cementite structure (e.g. spherodized microstructures and heavily tempered martensite) nucleation of austenite occurs at the ferrite/cementite interface [35,36], predominately at the junction between cementite and ferrite grain boundaries. For a complete ferritic structure it was showed that austenite initiated at the ferrite grain boundaries [4, 19, 37].

Austenite formation from low transformation products such as martensite, bainite, and acicular ferrite represent a complex phenomena. If the initial microstructure contains retained austenite, nucleation of new grains are not necessary for the reversion of austenite. However, Yan et al. [38] studied the isothermal reaustenitisation process from microstructures that grow by a diffusionless displacive mechanism (e.g. acicular ferrite, and bainite). Due to the nature of the displacive transformations, the authors showed that the retained austenite composition is given by the T_0 tie line instead of the equilibrium diagram. Therefore, the authors concluded that the reaustenitization process is delayed in the time since austenite transformation starts only when the carbon concentration of the residual austenite (located between the ferrite laths) exceeds its equilibrium carbon concentration.

In the absence of retained austenite, experimental evidence of nucleation at prior austenite grain boundaries and in ferrite lath boundaries [26, 28, 39, 40] has been reported for this type of microstrucutres (if recrystallization or tempering is avoided).

Austenite formation mechanisims

The mechanisms of austenite formation in steels may either involve diffusion of carbon and substitutional alloying elements or it can proceed in a partitionless manner in which no long range diffusion is required.

According to Speich et al. [19], in a ferritic/ pearlitic structure, austenite transformation can be divided into three different stages:

(1) First, the nucleation of austenite on pearlite/pearlite or ferrite/pearlite boundaries followed by a carbon diffusion-controlled growth of austenite into the pearlite colonies. (2) Second, occurs the posterior transformation of the ferrite into austenite, which can involve the partition of carbon or other alloying elements, such as manganese depending on the transformation temperature. (3) In the final step, if required, a redistribution of substitutional alloying elements to achieve equilibrium condition takes place. Nevertheless, these stages are not necessarily dissociated in time and they can appear overlapped in the experimental data [2, 4, 41].

Hot-stage confocal scanning laser microscope experiments in medium carbon steels indicated that boundary migration rate of the γ/pearlite front are roughly twice as those of the γ/α front. And that the measured interface velocities are qualitatively in good agreement with a transformation controlled by diffusion [42].

Abakay et al. [35] for Fe-C steels and later Atkinson et al [43] for Fe-C-X alloys described the isothermal reaustenitization from a ferrite/cementite structure. By assuming local equilibrium and ignoring carbon diffusion in cementite and ferrite, the phase transformation is controlled by diffusion of carbon in austenite. Hence, the process was modeled by solving a diffusion equation with boundary conditions at the austenite/ferrite and austenite/cementite interfaces. Later Reed et al. [12] adapted the model to an anisothermal transformation.

Caballero et al. [4] studied the mechanisms that control the austenitization process during continuous heating with different initial microstructures. The authors developed a model to describe the transformation kinetics from a fully ferritic, fully pearlitic and mixed initial microstructure. According to their work, from a pearlitic microstructure the growth rate of austenite is assumed to be controlled by carbon diffusion through the austenite from the cementite/austenite to the ferrite/austenite interface. But for the ferritic initial microstructure, the growth process is controlled by processes at the interface.

For interstitial free steels, it was suggested that austenization is controlled by processes at the interface; and the measured kinetics are similar to those for pure Fe systems [37, 44] .

However, evidence of interface controlled transformation is not only restricted pure ferritic microstructures. Several works indicated a possible transition from a diffusion to an interface controlled transformation mechanism.

Castro Cerda et al. [45] studied austenite formation in 0.2% C and 0.45% C steels with a ferritic-pearlitic microstructures for various heating rates. The authors suggested that for the case of ultra fast heating rates ($\geq$ 100 °C/s) transformation is initially controlled by diffusion but is later overtaken by a massive mechanism.

In a study of isothermal and nonisothermal austenite formation in case hardneable alloy steels, the transition from a diffusion controlled to a massive like transformation was observed at the T_0 temperature even at low heating rates [46].

Efforts to numerically model the austenite formation at high heating rates considering both controlling mechanisms have been proposed by several authors [47, 48]. Recently, Meccozi et al. [23] developed a semi-analytical model to describe the ferrite to austenite transformation kinetics from a ferritic/pearlitic structure. In this model it is assumed that pearlite dissolves first leaving an austenite grain supersaturated in carbon, where the transformation is assumed to occur under paraequilibrim conditions. The transformation rate is assumed to be controlled by mixed conditions (i.e. governed by carbon diffusion and interface mobility) and therefore the governing equation expresses the relationship between interface motion and carbon diffusion.

The current literature suggest that austenite formation proceeds by a nucleation and growth. However, the processes that control the transformation rate are still la subject of debate. The occurrence of a diffusion or interface control transformation not only depends on the initial microstructure and chemical composition, but it is also dependent on the transformation temperature and heating rate. Hence, mixed mode transformation models represent a promising approach to study this type of austenite reversion in complex microstructutres at high heating rates.

Austenite formation during welding of pipeline steels

In the present work, the objective is to study the re-austenization process in modern pipeline steels. To apply the findings and results of previous works on different steel alloy systems, it is important to consider that due to the unique chemical compositions and processing parameters involved in the fabrication of high strength pipeline grades, the initial microstructure from which austenite will form is quite complex. The modern Thermo Mechanical Controlled Processes (TMCP) involve precipitation of carbo-nitrides and austenite deformation at high temperatures followed by considerable accelerated cooling, resulting in a fine ferritic - bainitic microstructure, which is usually pearlite-free due to the tendency of reduce the carbon content. The small amount of carbon left after precipitation during the TMCP segregates

to second phases such as M/A or carbon rich zones during bainite formation. Then, austenite transformation takes place from a microstructure that consist of a ferritic structure, precipitates with relatively high thermal stability, and a small amount of carbon rich second phases.

During conventional heat treatments, austenite formation is usually disregarded due to the nature of the thermal cycle. These type of heat treatments commonly involve slow heating rates and sufficient time at high temperatures to assure homogeneous austenite conditions prior cooling. However, during quick thermal cycles, such as the ones encountered in welding processes, austenite formation becomes a crucial process to understand and predict the final microstructure and mechanical properties after cooling.

Specifically, during welding of pipelines steels, many current probematics require a particular attention to the austenite formation process.

The extent of heat affected zone (HAZ) depends on the critical transformation temperatures, A_{c1} and A_{c3}. However, thermodynamics are a poor predictor of this temperatures, specially at high heating rates. Then, studying the austenite formation process at heating rates comparable to those found in a welding thermal cycles represents an essential asset to define the HAZ limits.

It has been reported that the softening in the heat affected zone of field girth welds occurs at the FGHAZ/ICHAZ (fine grain heat affected zone/ intercritical heat affected zone) [49–51]. The appearance of the softening zone causes a serious mismatch of the performance between HAZ and the

base metal, affecting the service weld performance. These "softened" zones are characterized by a thermal cycle in which austenite reversion is either scarcely complete or incomplete, then becomes evident that the resulting microstructure is highly influenced by the austenite conditioning at high temperatures.

During the fabrication of electric resistance welding (ERW) pipes, the seam formation involves high heat inputs and significant deformation near the weld joint. After the welding thermal cycle, the bondline zone is typically harder and more brittle than the base material. According to both the American Petroleum Institute (API) and the Canadian Standards Association (CSA), a normalizing post welding heat treatment (PWHT) is required after the weld is produced to improve the joint properties, especially the toughness near the bondline. Lately, the heat treatment techniques and parameters has been matter of research to understand the development of bondline microstructure and improve the weld seam fracture toughness for low temperature applications. It has been proposed that the characteristics of nucleation and growth of austenite during the "normalizing" treatment are greatly influenced by the texture of the as welded microstructure, and hence also the brittle fracture behavior of the ferrite form during cooling [52, 53].

Another common degradation of HAZ toughness in pipeline steels during multipass welds can be attributed to the formation of local brittle zones (LBZ) at the ICCGHA [54]. The reheating of CGHAZ (coarse grain heat affected zone) into a dual phase field temperature, is prone to form harmful

second phases such as M/A constituents due to the characteristics of the microstructure prior reheating of the subsequent welding pass. Then the formation of austenite from a different microstructure then the base material also represents an valuable field to study.

In summary, a thorough understanding of the austenite formation process during continuous heating represents an essential asset to improve weld joints performance. Up to date, the dependence of the re-austenization phenomena with the heating rates and the initial microstructure has not been systematically studied in detail for modern high strength pipelines.

1.2 Objectives

The main objective of this research is to forge the first steps towards a physical understanding of the re austenization process during a rapid continuous heating for high strength pipeline materials. To achieve this goal the following objectives have been established:

- Study in general forms the austenite formation process in low carbon microalloyed steels as a function of the heating rate.
- Investigate microstructural and kinetics aspects the ferrite to austenite transformation.
- Implement a model capable to rationalize the observed differences in transformation kinetics with the heating rate.

1.3 Thesis Outline

This thesis consists of four chapters focusing on achieving the aforementioned goals. After the introduction, the following four chapters consist on articles that are either published or intended to share with the community. Chapter 5Models to predict hardness in the HAZchapter.5 contains an article review to highlight the importance of austenite decomposition. Chapter 6Conclusionschapter.6 include the main conclusions of the research project. At the end of the dissertation, the appendices present additional information about the numerical calculations performed in this study. This section provides an outline of the chapters included in this thesis.

Chapter 2: Effect of the heating rate on austenite formation in low carbon microalloyed Steels

This paper, published in the Welding Journal AWS, covers a study of austenite formation during continuous heating on a grade X80 pipeline steel with an initial ferritic and bainitic microstructure. The results, including a continuous heating transformation diagram for the studied alloy, suggests that transformation kinetics are highly sensitive to the heating rate. Also that transformation occurs at a temperature range in which the redistribution of alloying elements among the product and parent phases is not necessary.

Chapter 3: Kinetics of austenization during heating accounting for solute drag and Mn redistribution

Based on the results obtained in chapter 2, the kinetic differences between slow and fast heated samples were studied in this paper (to be submitted). In this chapter, a Gibbs free energy balance across the interface is proposed to rationalize the systematically observed differences in kinetics.

Chapter 4: Driving Force for phase transformation of microalloyed steels under paraequilibrium conditions

The thermodynamic driving force for transformations represents a essential parameter for any energy based transformation model. In this communication, a methodology to calculate the driving force for transformation in a multicomponent alloy under paraequilibrium is described. The methodology requires to express the alloyed material as a fictitious binary system to later use the Gibbs free energy curves to mathematically (and graphically) calculate the chemical driving force for transformation.

Chapter 5: Models to predict hardness in the HAZ

This article covers a review of the evolution and description of the different empirical models to predict the hardness of the heat affected zone in low carbon steels are presented in this paper. The goal of this work was to enhance the reader awareness about the different and simplicity of these

tools which have been mainly published during 70's and 80's. The accuracy of these empirical models rely on the proper selection according to the steel and welding parameters of interest. This review article, published in the CWBA Welding Journal in the Spring of 2019, serves a guide to understand and select the most convenient model.

Chapter 2

Effect of the heating rate on austenite formation in low carbon microalloyed steels

2.1 Abstract

The extent of the heat affected zone (HAZ) in welding is typically estimated from thermodynamic considerations of austenization; however, thermodynamics is a poor predictor of HAZ location in microalloyed steels. This work addresses this problem through the study of austenite formation during continuous heating on a grade X80 pipeline steel with an initial ferritic and bainitic microstructure. The methodology of analysis involved dilatometry, electron microscopy, and thermodynamic calculations. A continuous heating transformation diagram (CHT) was developed for heating rates varying from 1 to 500°C/s. For the slower heating rates, austenite start transformation temperature is higher than the one dictated by the equilibrium; while for the faster heating rates, start transformation temperature gradually approaches the theoretically calculated temperature at which the ferrite can transform without long-range diffusion into austenite, possibly through a massive transformation. Partial transformation experiments suggested that austenite formation occurs in two stages: (a) First, the transformation of bainitic zones into austenite and later (b) the transformation of polygonal ferritic grains.

2.2 Introduction

The mechanical properties of welded materials are often limited by those of the heat affected zone (HAZ). In the case of ferritic steels, the outer edge of the HAZ is closely associated with beginning of transformation to austenite during heating (A_{c1}). While the effect of cooling on the HAZ is relatively well understood, and much literature has been devoted to it, the effect of heating rate has received scant attention until recently. This lack of attention was justified, because common arc welding operations in traditional steels generate heating rates in which the material transforms qualitatively as expected from thermodynamics; i.e. the transformation temperatures are only slightly affected by the heating rate, and the nature of the transformations during heating or cooling remains similar. The widespread use of microalloyed steels and processes such as LBW, laser cladding, and laser heat treatment has brought attention to phenomena that cannot be explained based on traditional understanding of pure diffusive transformations.

The case of medium carbon and eutectoid steels with a ferritic-pearlitic initial microstructure has been studied in detail. Studies of austenite formation on slightly or fully pearlitic initial microstructures concluded that austenite preferably nucleates at cementite/ferrite interfaces of the pearlite colonies and at conventional heating rates the growth is controlled by carbon diffusion [6, 11, 25, 55–60].

Much less research has been performed for ultra low carbon and interstitial free steels [5, 37, 61, 62], medium Mn steels [63], ferrite and carbide aggregates [44], baintic [56, 64–66] or martensitic structures [9, 16, 57, 67]. Even fewer studies are available in literature concerning thermomechanically controlled processed (TMCP) modern low carbon (<0.1 wt.%) microalloyed steels. Previous research addressing initial microstructures such as ferritic/pearlitic [57], and ferritic/bainitic or ferritic/martensitic structures [18,68] are helpful to begin an understanding of these systems, but not yet comprehensive.

The effect of heating rate has been studied at low and conventional heating rates (<50°C/s), and the general agreement (though not unanimous) is that the transformation into austenite is a thermally activated process in which the transformation temperatures increase with the heating rate. This behavior is generally expected to extend to faster heating rates; however, for fast (50°C/s to 100°C/s) and ultra-fast (>100°C/s) heating rates, recent work on low and medium carbon steels indicated a possible transition from a diffusion controlled to an interface controlled transformation mechanisms in austenite formation [45]. Additional supporting evidence of austenite formation via an interface-controlled reaction, even for low heating rates (1°C/s), has been also provided for medium carbon steels [42], interstitial free steel [5, 44], and low carbon, medium Mn steels [63]. A complete modeling of austenite formation kinetics at high heating rates considering both transformation mechanisms can found in [47, 48].

The characteristics times and wide range of heating rates associated to different welding thermal cycles (depending on the welding process and parameters) demands a comprehensive study of austenite formation during continuous heating. It is well known that critical transformation temperatures, kinetics and mechanisms involved during the austenization are susceptible to the heating rate. Thus, to have a better understanding of all the microstructural changes that will define the HAZ properties (on cooling transformations) it is important to comprehend how the initial conditions prior cooling are achieved. The present work, becomes more relevant specially for the intercritical and the outer region of the HAZ where the peak temperatures are slightly above the transformation finish temperatures and there no time for austenite grain growth.

The aim of this paper is to study the effect of heating rate on austenite formation in TMCP steels, represented by a modern X80 pipeline grade with a ferritic bainitic microstructure. Dilatometry, microscopy, and thermodynamic calculations were used to determine and interpret a continuous heating transformation diagram (CHT) to explore the features of the austenitization process.

Table 2.1: Chemical composition of the X80 alloy studied (wt%).

C	Mn	Si	Cr + Cu + Ni	Mo	Nb	V	Ti	Al	N	Fe
0.035	1.7	0.28	0.66	0.305	0.094	0.003	0.017	0.044	0.0058	bal.

2.3 Experimental Procedure

2.3.1 Material System

Cylindrical solid and hollow samples (10 mm in length and 4 mm in diameter, with a 3 mm hole) were extracted from a 12 mm thickness skelp of commercial X80 steel. Dilatometry specimens were carefully machined from a fixed depth of the skelp surface (along the longitudinal direction) to avoid the extraction of samples with traces of the typical centreline microsegregation zone usually presented in these thermo mechanically processed steels [69,70]. The chemical composition of the steel expressed in weight % is shown in table 3.1Chemical composition of the X80 alloy studied (wt%).table.caption.27.

2.3.2 Dilatometry

Continuous heating experiments were performed with a high-resolution quench L-78 RITA Linseis dilatometer. To study the influence of the heating rate on the austenite formation, fully austenitization cycles followed by an immediate rapid cooling (600°C/s) were performed at different heating rates of 0.1, 1, 10, 30, 70, 100, 200, 300, 500°C/s up to a peak temperature between 950 to 1100°C depending on the heating rate. For low heating rates, <10°C/s, the peak temperature was initially selected as 950 °C and for high heating

rates, >10°C/s, peak temperature was raised up to 1100°C to ensure that transformation was complete prior quench. Additionally, heating cycles with different peak temperatures and different holding times were performed for selected heating rates to study the different stages of austenite formation. For a fixed heating rate of 100 °C/s, samples quenched from 835 and 900 °C were used to study different stages of austenite formation (section 2.4.2Partial Transformation Experimentssubsection.2.4.2). Additional annealing experiments, with a heating rate of 1 °C/s, for 0, 20, 3 00 and 600 s at 750 °C were performed to study the austenitization process below the experimental A_{c1} temperature (section 2.4.3Annealing Experimentssubsection.2.4.3). All tests were performed at a constant pressure of inert gas Helium and the temperature was controlled by a K-type thermocouple spot welded to the midsection of each specimen.

Ideally, before and after the ferrite to austenite transformation, the specimen will expand at a constant rate determined by the coefficient of thermal expansion of each phase; hence the derivative of the elongation change with respect to the temperature will present a constant value. However, the effects of the magnetic transition, recrystallization and carbide dissolution can deviate this linear behavior before and after the structural transformation. Therefore, in the present work, the critical transformation temperatures, A_{c1} and A_{c3}, were determined using the first derivative methodology [71, 72] as

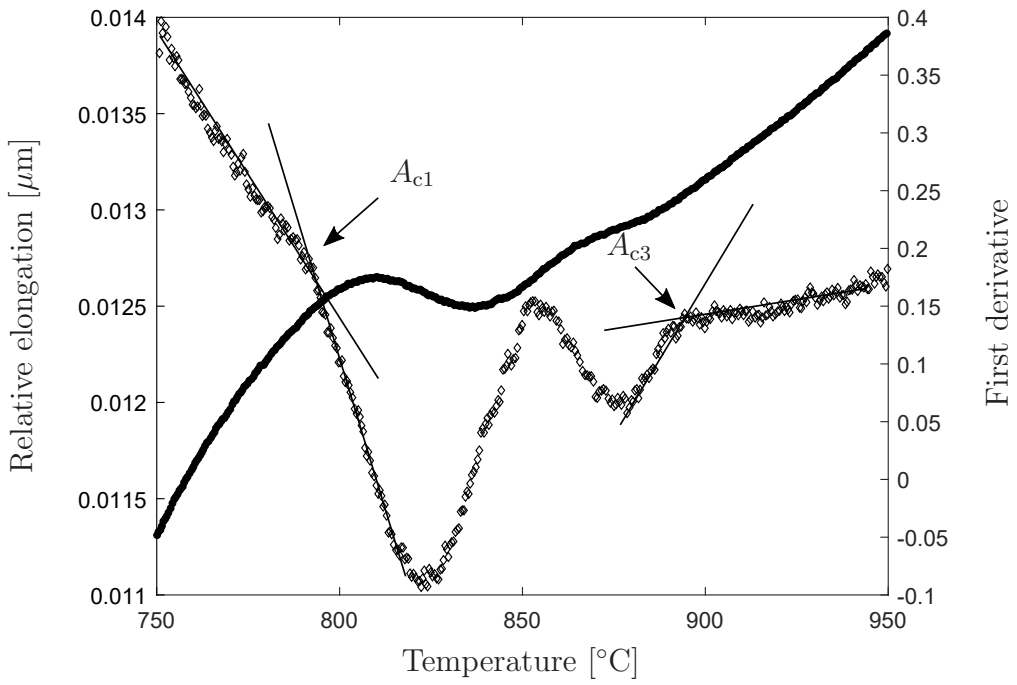

Figure 2.1: Dilatation curve (solid circles) and its first derivative (diamonds), done by the forward finite difference technique and later smoothed using the moving average of 20 points, of the samples fully austenitized at 100 °C/s

it is shown in Figure 2.1Dilatation curve (solid circles) and its first derivative (diamonds), done by the forward finite difference technique and later smoothed using the moving average of 20 points, of the samples fully austenitized at 100 °C/sfigure.caption.15.

To obtain the transformed fraction as a function of the temperature, an improved methodology from the lever rule proposed by Kop et al. [73] was employed. This correction, contrary to the lever rule, accounts for the difference in densities and thermal coefficient expansion between austenite and ferrite.

The Curie temperature, T_c, was also determined from the dilatometric experiments. To identify the onset temperature of the magnetic transformation, the power delivered by the high frequency (HF) module was evaluated. Below the Curie temperature, two different phenomena, Joule heating and hysteresis loss contribute to the heating of the sample. When the Curie temperature is reached, magnetic properties change, and only Joule effect is responsible for the heating. This is manifested in a significant increase in power delivered to keep the heating rate constant. This methodology to evaluate T_c from dilatometry experiments has been successfully employed by several authors [73, 74].

2.3.3 Characterization of microstructure

After the thermal cycles, samples were cross-sectioned, and polished prior to the enchant process. Samples etched with 2% Nital were examined by Optical (OM) and Field Emission - Scanning Electron Microscopy (SEM) Zeiss Sigma 300 VP-FESEM with an operating voltage of 5 to 15 keV.

The ferrite grain size was measured on several SEM micrographs with different magnifications. The average ferrite grain diameter (d_α) was estimated using the mean linear intercept method and the effect of a nonequiaxial structure was eliminated by using lines in different orientations with an approximately equal weight.

2.4 Results

As-Received Material

Optical and SEM micrographs of the as-received material are shown in Figure 2.2(a) Optical and (b) SEM micrographs of granular bainitic zones of the initial microstructure.figure.caption.17 (a) and (b) respectively. The initial microstructure, typical of low carbon thermomechanically processed steels, consists in a complex structure formed of polygonal ferrite (PF) and granular bainite (GB). The larger ferrite grains, transformed at high temperatures, are surrounded by the ferritc bainitic zones which are constituted of much more finer ferrite grains and second phases mainly along the grain boundaries, Figure 2.2(a) Optical and (b) SEM micrographs of granular bainitic zones of the initial microstructure.figure.caption.17 (b).

The average grain size, d_α, and the standard deviation are 2.06 and 0.70 μm respectively.

The second phases are identified as bright zones in the high magnification scanning electron micrograph, Figure 2.3SEM micrograph of an carbon rich zone located between two bainitc ferrite grains.figure.caption.18. Although carbon content is significantly low, exceeds its solubility in ferrite at low temperatures, thus the excess will be located in these second phases. The low carbon content available makes difficult the formation of pearlite dur-

ing austenite decomposition resulting in a microstructure practically free of pearlite. Instead, the residual austenite loacted between the bainitic grains will transform into block - like M/A constituents, carbides, or even retained austenite at room temperature in absence of pearlite formation.

From a previous extensive characterization work, in the same studied alloy and processing conditions, the following precipitates with a NaCl-FCC structure were identified: (i) relatively large (230 - 170 nm) Ti-rich nitrides, (ii) medium size (30 - 80 nm) Nb-rich (with variable amounts of Ti) carbidonitrides, and finally (iii) nanosized (less than 10 nm) Nb-Mo carbides. The Ti and Nb rich nitrocarbides (i and ii) usually precipitate at high temperatures in the γ field while the nano-sized precipitates (containing Mo) formed at lower temperatures, close to the coiling temperature. More detailed information about the precipitates in the as-received condition can be found in work performed by Lu [75].

In summary, from the study of the as-received microstructure it can be concluded that austenite forms from a nearly complete ferritic structure composed by polygonal ferrite, granular bainite with minimal amount of carbon-rich second phases and a variety of MX precipitates where M=(Ti, Nb, Mo) and X=(N,C).

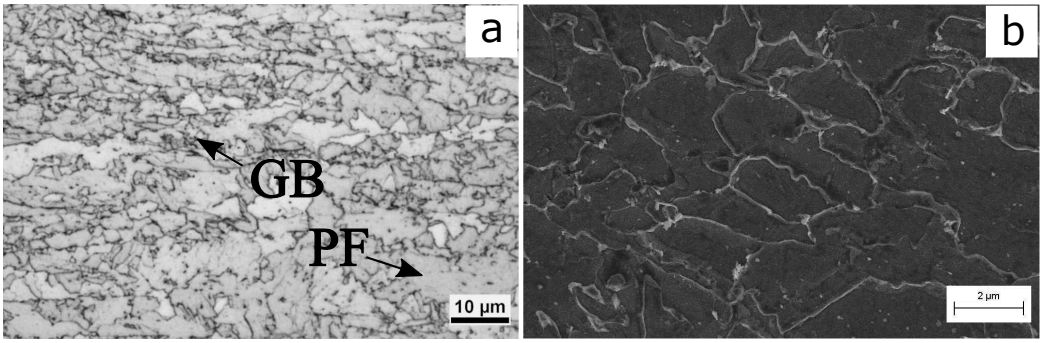

Figure 2.2: (a) Optical and (b) SEM micrographs of granular bainitic zones of the initial microstructure.

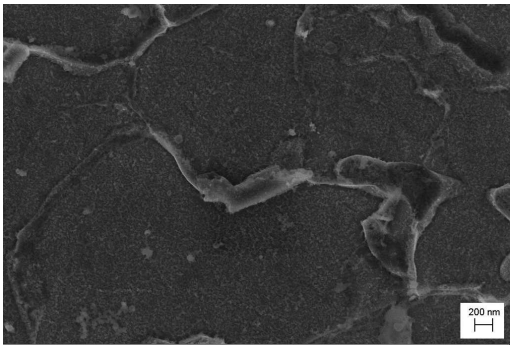

Figure 2.3: SEM micrograph of an carbon rich zone located between two bainitc ferrite grains.

2.4.1 Dilatometry- Fully Transformed Samples

The values of A_{c1}, A_{c3}, and T_c for all dilatometry tests were determined using the procedure outlined above. The results, shown in Table 2.2Critical transformation temperatures determined from dilatometrytable.caption.19, were used to construct the Continuous Heating Transformation (CHT) Diagram shown in Figure 2.4Continuous heating transformation diagram of the studied alloyfigure.caption.20. The experiments revealed systematic trends for A_{c1} and A_{c3}.

The start of austenization temperature, A_{c1}, shows a slightly gradual increase with heating rates, approaching 810°C at the highest rates. In contrast, the end of austenization, A_{c3} exhibits higher susceptibility to the heating rate. The magnetic transition, T_C, is unaffected by the heating rate for all the experiments.

Although there is a significant increase in the transformation range temperatures (A_{c3} - A_{c1}) with the heating rate (hr), the time to complete austenization decreases, calculated as $(A_{c3} - A_{c1})/hr$, significantly with the heating rate, as shown in Figure 2.5Time required for the transformation to complete as a function of the heating ratefigure.caption.21.

At high heating rates (above 10 °C/s), during the structural transformation, the elongation curve against the temperature presents two main different stages which are much more noticeable on the derivative curves. As it is shown in Figure 2.6Derivatives curves for heating rates of (a) 10, (b) 30, (c) 100, and (d) 500 °C/s.figure.caption.22, each derivative curve is

composed by a strong peak at lower temperatures, close to A_{c1}, followed by a weaker peak at higher temperatures, determining the end of the structural change, A_{c3}. From Figure 2.6Derivatives curves for heating rates of (a) 10, (b) 30, (c) 100, and (d) 500 °C/s.figure.caption.22, it can be observed that the first peak, moves slightly towards high temperatures as the heating rate increases, while the second peak presents much higher susceptibility to the heating rate.

Table 2.2: Critical transformation temperatures determined from dilatometry

heat. rate	**°C/s**	**1**	**10**	**30**	**70**	**100**	**200**	**300**	**500**
T_c	°C	729	728	722	725	730	732	728	728
A_{c1}	°C	780	797	798	795	798	810	805	812
A_{c3}	°C	888	875	879	885	892	922	934	957

2.4.2 Partial Transformation Experiments

To explore the sequence of transformations , experiments with intermediate peak temperatures were performed. By having partial austenization, the austenite developed is distinguished from untransformed structure by the presence of a much more finer microstructure characteristic of fast cooling transformations.

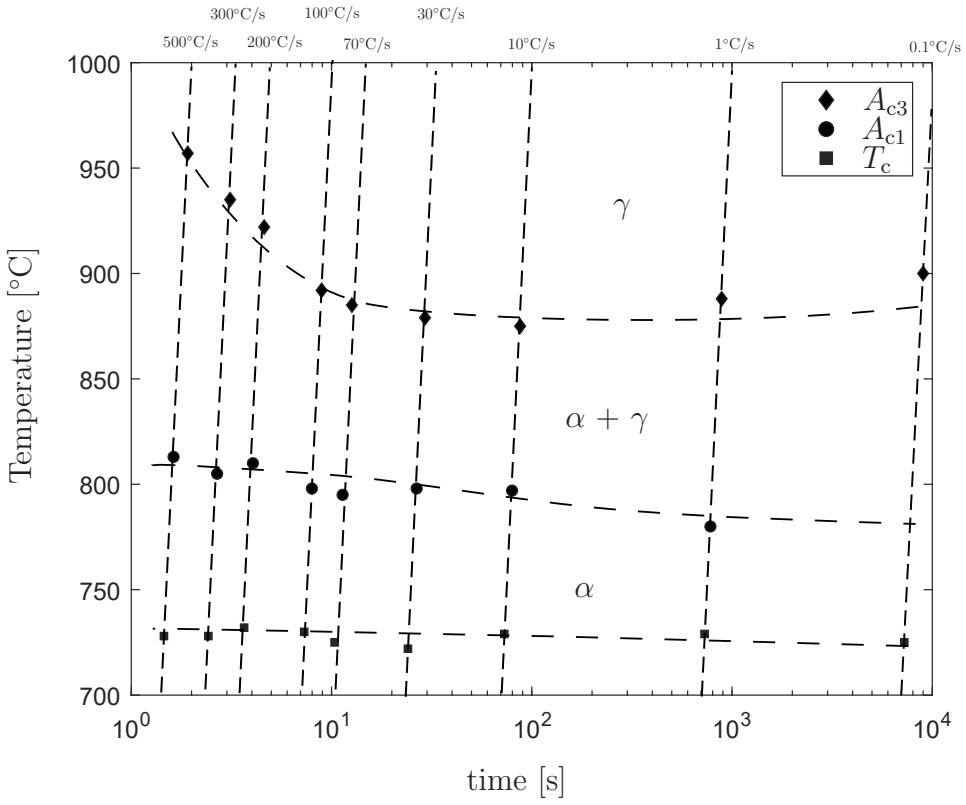

Figure 2.4: Continuous heating transformation diagram of the studied alloy

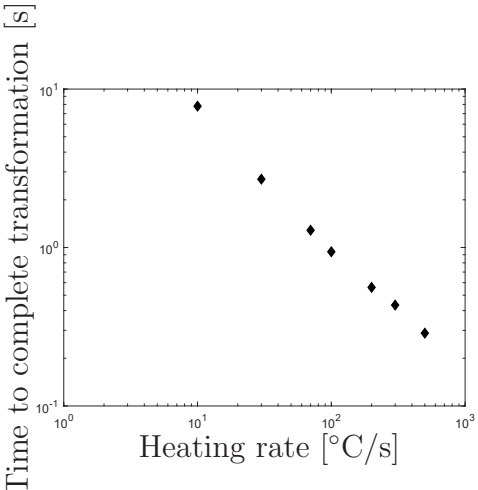

Figure 2.5: Time required for the transformation to complete as a function of the heating rate

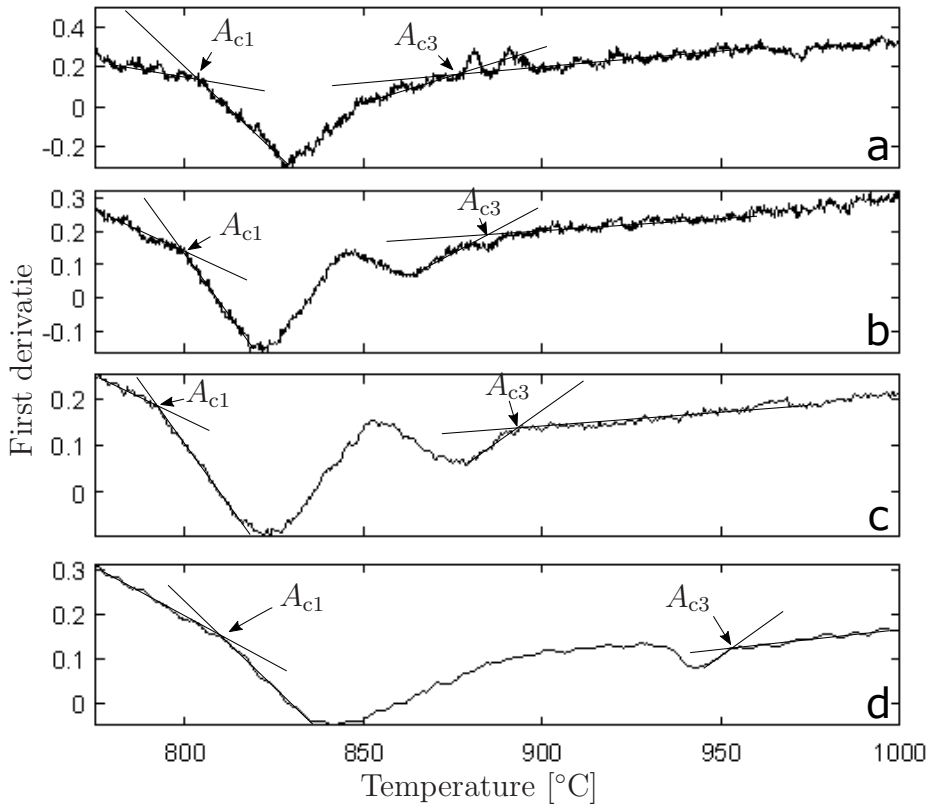

Figure 2.6: Derivatives curves for heating rates of (a) 10, (b) 30, (c) 100, and (d) 500 °C/s.

Three different peak temperatures were explored by heating samples at 100°C/s up to 835°C, 900°C, and 1110°C, followed by a rapid cooling of 600°C/s to room temperature. Figure 2.7SEM micrographs of the samples transformed up to 835°C (a), 900°C (b), and 1100°C (c), followed by a rapid cooling of 600°C/s.figure.caption.23 shows the resulting microstructure of these experiments.

In the sample heated up to 835°C (approximately 25% of transformation according to the dilatometry analysis and after the first peak of the derivative, Figure 2.7SEM micrographs of the samples transformed up to 835°C (a), 900°C (b), and 1100°C (c), followed by a rapid cooling of 600°C/s.figure.caption.23 (a)), only the banitic zones in the surroundings of the larger ferrite grains presented evidence of transformation into austenite, γ'. The polygonal ferrite grains, pointed as PF, still untransformed result in a similar heterogeneous microstructure to the as-received sample.

For the sample heated up to 900°C, right after the second peak where the transformation is completed (Figure 2.7SEM micrographs of the samples transformed up to 835°C (a), 900°C (b), and 1100°C (c), followed by a rapid cooling of 600°C/s.figure.caption.23 (b)), the larger ferrite grains are absent evidencing a growth of austenite into them which later will transform into ferrite and bainite during cooling. The resulting in a more homogeneous microstructure composed by ferritic and banitic zones.

Figure 2.7SEM micrographs of the samples transformed up to 835°C (a), 900°C (b), and 1100°C (c), followed by a rapid cooling of 600°C/s.figure.caption.23 (c) corresponds to heating up to 1100°C, and it shows the resulting microstructure of two phenomena: complete transformation into austenite, and significant austenite grain growth, expected from the high peak temperature reached. During the rapid cooling, the austenite decomposed into a classic upper bainitic structure.

2.4.3 Annealing Experiments

For the continuous heating experiments there is no evidence of transformation below 780°C even at the lowest heating rate (1°C/s); however, the A_{e1} temperature expected from thermodynamics is 640°C.

To investigate the discrepancy between experimental and thermodynamic austenization temperatures, isothermal annealing experiments were carried out in a sample at 750°C for 0, 20, and 300 and 600 s.

In these annealing experiments, the as-received material experienced transformation into austenite after 20 s of the isothermal annealing, and after 300 s reached a volume fraction close to the one predicted by thermodynamics, approximately 15%.

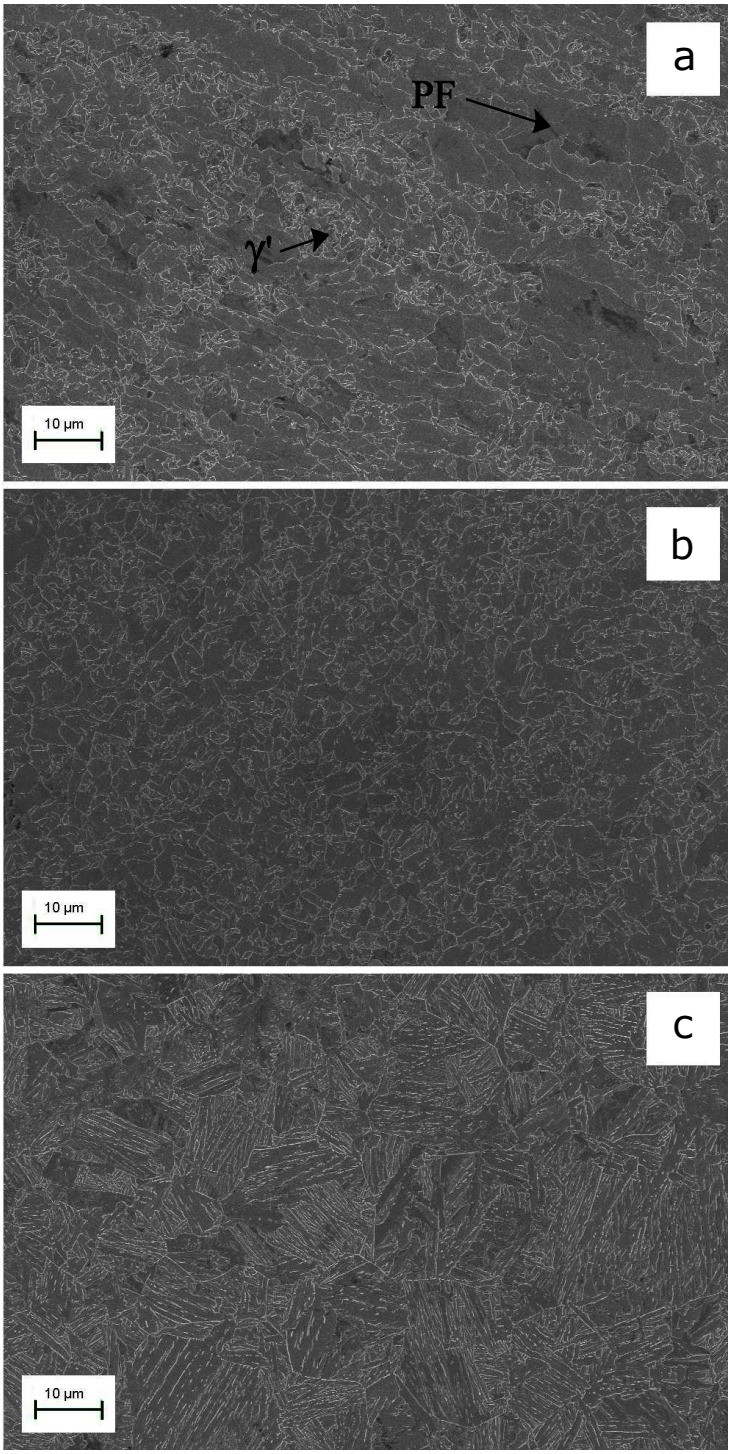

Figure 2.7: SEM micrographs of the samples transformed up to 835°C (a), 900°C (b), and 1100°C (c), followed by a rapid cooling of 600°C/s.

Figure 2.8Optical (a) and SEM (b) micrographs of the annealed sample at 750 C during 600 s and then rapidly cooled down at 200°C/s.figure.caption.24 indicates that austenite grows preferably in the bainitic zones, where most of the carbon rich phases were located. In the SEM micrograph no carbon-rich phases zones are seen, suggesting that they were consumed by the austenite.

From the carbide / martensitic structure formed during cooling at 200°C/s it can be derived that during the annealing at high temperatures there was enough time for a significant alloying element partition into the austenite and hence, an increase on the hardenability compared to the samples quenched intermediately after reaching the peak temperature.

2.4.4 Mass Balance

Thermodynamic calculations were performed using Thermo-Calc (TCFE10 database) to obtain transformation temperatures, A_{e1}, A_{e3}, para-equilibrium boundaries and the T_0 curves for studied steel. The calculated A_{e1} and A_{e3} are 640 and 840°C respectively.

During the thermomechanical controlled processing, titanium, niobium, and vanadium nitrocarbides are intentionally precipitated depleting the austenite (that later transforms into ferrite) from carbon. These precipitates are known to be thermally stable at high temperatures, and they will trap the consumed carbon even at high temperatures above 1100°C, specially for short time periods [18, 76].

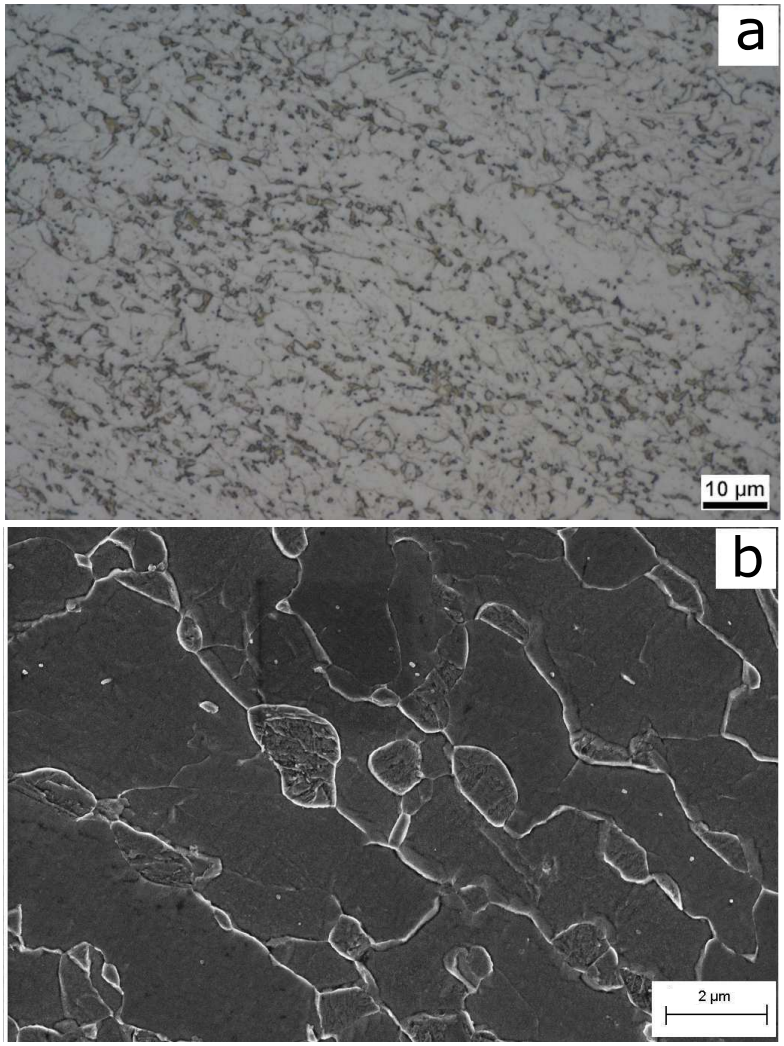

Figure 2.8: Optical (a) and SEM (b) micrographs of the annealed sample at 750 C during 600 s and then rapidly cooled down at 200°C/s.

In the as-received microstructure, the carbon available to take part in the austenite formation during heating will be distributed between the ferrite grains (with very low carbon solubility) and a small volume fraction of second phases (such as M/A or retained austenite) which are richer in carbon and prone to transform at high temperatures.

Neglecting the Ti rich precipitates (which they usually combine with N at high temperatures during the first stages of the thermomechanical processing and do not have further reactions, and considering only Nb rich precipitates (which may contain other alloying elements in solution such as Mo, V and Ti), from now on referred as MX, ; the following mass balance can be used to estimate the carbon content in austenite after precipitation ceased:

$$x_{\mathrm{c}} = x_{\mathrm{c}}^{\gamma} m_{\gamma} + x_{\mathrm{c}}^{\mathrm{MX}} m_{\mathrm{MX}} \tag{2.1}$$

where all fractions are in wt%, x_{c}^{γ} is the carbon content of austenite, $x_{\mathrm{c}}^{\mathrm{MX}}$ is the carbon content in MX, m_{γ} is the mass fraction of austenite, and m_{MX} the mass fraction of MX, such that $m_{\gamma} + m_{\mathrm{MX}} = 1$

Assuming that the amount of MX Nb-rich precipitates is equal to the maximum amount given by thermodynamic calculations (at 700°C), the maximum carbon content of austenite prior its decomposition, x_{c}^{γ}, is estimated as 0.019 wt%. This mass balance compares well with a similar material analyzed in [75], in which the carbon content in austenite was assessed as $x_{\mathrm{c}}^{\gamma} = 0.0207$ wt%.

2.4.5 Analysis of Para - Equilibrium and Diffusion Time Scales

Figure 2.9T_0 and para-equilibrium lines calculated with Thermo-Calc. Where $x_c^{u\gamma}$ is the carbon concentration of the untransformed autenite. figure.caption.25 shows the para-equilibrium and T_0 curves calculated with Thermo-Calc for the studied alloy. The A'_{e1} and A'_{e3} curves represent the ferrite/austenite phase boundaries under para - equilibrium and the T_0 curve defines the conditions at which the Gibbs free energy of the ferrite and austenite (with the same chemical composition) are equal. For a set amount of carbon content, the temperature given by the T_0 line determines the temperature above which austenite can form with the same chemical composition as the parent phase (ferrite), and hence no long-range diffusion is required. The T''_0 curve was calculated with the same basis as T_0 but adding 400 J/mol to the ferrite phase in the thermodynamic calculations to account for the strain energy associated to the displacive character of the bainite formation upon cooling [77].

During last stages of the TMCP austenite decomposes into two different products: At high temperatures, polygonal ferrite; and as the temperature decreases, usually around the coiling temperature (CT), mixed displacive /reconstructive transformations, such as acicular ferrite or bainite, occur. The precipitation of Ti and Nb-rich carbides occur at high temperatures

and the Nb-Mo nano-sized carbides and the bainitic transformation can take place at comparable temperatures. However, the remaining carbon after all precipitation ceases exceeds the solubility in ferrite at low temperatures, $x_c^{\gamma} = 0.0207$ [78, 79].

The transformation of austenite into granular bainite at the coiling temperature, which originally forms from an austenite with a carbon content x_c^{γ}, will not obey the lever rule and will likely exhibit a classical incomplete reaction phenomena [77] in which the reaction ceases when the carbon content of the remaining austenite reaches the T_0'' curve, $x_c^{u\gamma}$. The untransformed austenite, refereed in this work as carbon-rich second phases, will likely transform partially into M/A constituents in absence of carbide precipitation.

The carbon content in ferrite will be assumed to be between 0.007 and 0.003 wt.% which is consistent with the solubility curves of carbon in ferrite for low temperatures. The approximated value is similar the reported values of 0.005 wt.% and 0.008 wt.% for the same material [75] and a similar alloy [80] respectively. Since the coiling temperature is unknown, the carbon content of the untransformed austenite (product of the imcomplete reaction phenomena), $x_c^{u\gamma}$, was estimated assuming an intermediate CT of 600 °C and its intersection with the a T_0'' curve calculated. The value given by $T_0''(CT)$, pointed in Figure $2.9T_0$ and para-equilibrium lines calculated with Thermo-Calc. Where $x_c^{u\gamma}$ is the carbon concentration of the untransformed autenite. figure.caption.25, represents the carbon composition of the untransformed austenite.

The diffusion coefficients of substitutional alloying elements are orders of magnitude lower than that of interstitial elements, and the difference increases as the temperature decreases. With an approximated ferrite grain size of 2 μm, the diffusion coefficient of substitutional elements in the CT range is between 10^{-17} to 10^{-20} m^2/s [79]. For a characteristic diffusion distance $x = \sqrt{Dt}$, it will take days for the substutitional alloying elements to partition and reach orthoequilibrium conditions. Thus, the ferrite inherits the bulk composition of substitutional alloying elements during rapid thermal cycles, and paraequilibrium conditions must be used to and study the ferrite/austenite boundaries upon continuous heating.

To consider a partitionless transformation of ferrite to austenite, it is necessary to use the composition of carbon in the ferrite to estimate the temperature A_M at which this process is thermodynamically possible. The temperature A_M is the intersection of the T_0 curve and the carbon content of ferrite. For x_c^α between 0.007 and 0.003 wt.%, Figure 2.9T_0 and paraequilibrium lines calculated with Thermo-Calc. Where $x_c^{u\gamma}$ is the carbon concentration of the untransformed autenite. figure.caption.25 yields a temperature A_M in the range of 812 to 808°C.

If transformation involves the long rage diffusion of carbon atoms, the carbon-rich second phases will play role during the transformation as they are the only available carbon source. If the untransformed austenite, does not decompose at low temperature or during heating, the temperature at which austenite will start growing will be higher that the one indicated by

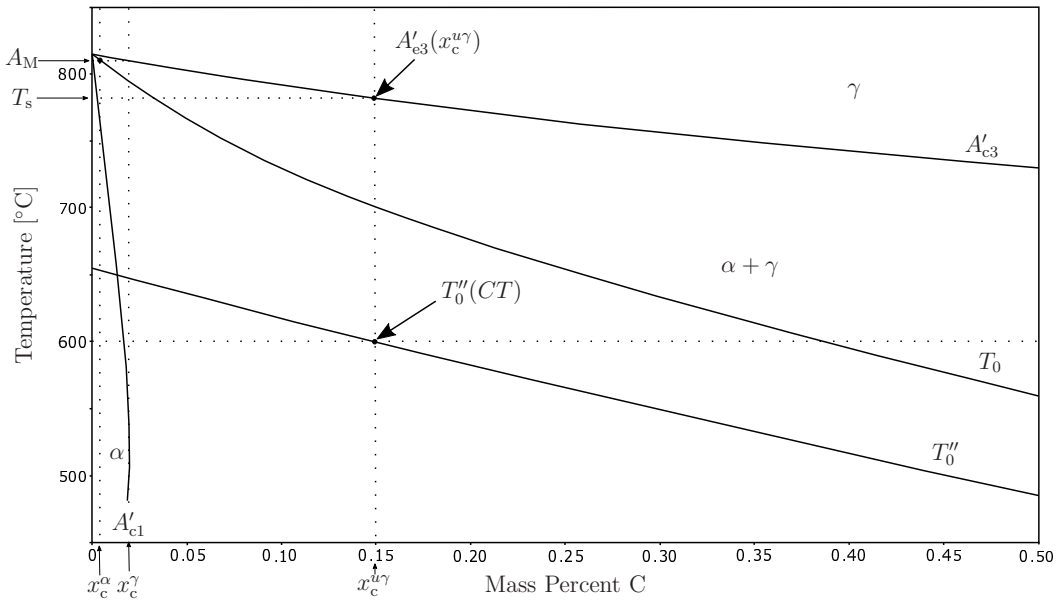

Figure 2.9: T_0 and para-equilibrium lines calculated with Thermo-Calc. Where $x_{\mathrm{c}}^{u\gamma}$ is the carbon concentration of the untransformed autenite.

the equilibrium. According to the theory presented by Yang et. al [65], the incomplete reaction phenomena during the bainitic transformation will result in a higher volume fraction of austenite than the required by the lever rule. Because of this metastable conditions, during heating, the driving force for austenite to trasnform into ferrite will still be negative until the temperature reaches , $T_{\mathrm{s}} = A'_{\mathrm{e3}}(x_{\mathrm{c}}^{u\gamma})$, pointed in Figure 2.9$T_0$ and para-equilibrium lines calculated with Thermo-Calc. Where $x_{\mathrm{c}}^{u\gamma}$ is the carbon concentration of the untransformed autenite. figure.caption.25. Hence, austenite will start to growth only if temperature is above T_{s}. According to the approximations and calculations made above, the T_{s} temperature for a coiling temperature of 600 °C is 785°C similar to the A_{c1} obtained at low heating rates experiments.

2.5 Discussion

Two different stages of the transformation, were observed on dilatation curves for heating rates above 10 °C/s; these two stages are evident on the first derivative curve, Figure 2.6Derivatives curves for heating rates of (a) 10, (b) 30, (c) 100, and (d) 500 °C/s.figure.caption.22. Although these phenomena can overlap in time/temperature, it is accepted that the dilatation curve during austenite formation is a convolution of two separate transformations [2, 25, 81]. For the case of a classic ferritic and pearlitic structures, the different stages of the dilatation curve are associated with pearlite and ferrite transformation into austenite. However, in the present work, the as received material was pearlite free; the initial microstructure was composed by considerably larger polygonal ferrite grains embedded in a much finer granular bainite grains. The two stages observed are likely to be a first transformation of the granular baintic zones, which are finer and adjacent to carbon rich zones, followed by the polygonal ferrite.

Evidence supporting the transformation sequence proposed is in the partial transformation experiments reaching 835 °C (immediately after the peak of the first transformation). In these experiments, the microstructure associated with a transformation during heating is observed only in the granular bainitic zones, leaving the large polygonal ferrite grains untransformed (Figure 2.7SEM micrographs of the samples transformed up to 835°C (a), 900°C (b), and 1100°C (c), followed by a rapid cooling of 600°C/s.figure.caption.23

(a)). A partially transformation experiment reaching 900 °C (immediately after the peak of the second transformation) showed that the polygonal ferrite grains were consumed during heating Figure 2.7SEM micrographs of the samples transformed up to 835°C (a), 900°C (b), and 1100°C (c), followed by a rapid cooling of 600°C/s.figure.caption.23 (b).

The first stage of the transformation showed only a small effect on heating rate, likely because of the faster kinetics involving the higher amount of interfaces and possible nucleation sites for austenite. The transformation of polygonal ferrite, with fewer interfaces and carbon rich zones, is expected to be slower and more influenced by the heating rate.

The finish transformation temperature (A_{c3}) is much more susceptible to the heating rate than A_{c1}. Experimental noise made the determination of A_{c1} more difficult at lower heating rates, making unreliable any determination at 0.1°C/s. The determination of A_{c3} was always reliable. In both cases, the values determined through dilatometry seem to follow consistent trends. For the samples transformed at heating rates above 10°C/s, the A_{c3} temperature shows a gradual increase with the heating rate. However, A_{c3} for the sample heated at 1 and 0.1 °C/s shows the opposite trend. The same trend was reported by Chang et al. [68] for a bainitic microstructure with a similar alloy composition. The trend at fast heating rates was expected based on superheat necessary to drive a faster transformation. Enomoto et al. [48]

indicated that at high heating rates the movement of austenite interface (i.e. growth of austenite into ferrite grains) can be slower than the actual change in temperature resulting in a significant increase in the A_{c3} temperature. The trend at slower cooling rates has no obvious explanation.

The experimentally obtained austenite formation temperatures are significantly higher than the ones predicted by the equilibrium; in particular, A_{c1} differs by more than 100 °C even at heating rates as low as 1 °C/s. In contrast with transformations during cooling that usually start from single-phase austenite, heating transformations involve a much more complex starting microstructure depending on the previous processing, and which might include metastable components. The complex starting microstructure will involve a diversity of transformations during heating with different time scales, and limited by the time available given by the heating rate.

In the present work, the heating experiments initiate from a nearly complete ferritic/bainitic structure. The minor fraction of carbon-rich second phases observed between the bainitic ferrite can be associated with the products of an incomplete transformation to bainite. Although the exact nature of these carbon rich zones has not been identified, according to characterization performed in this work and found in literature [80, 82, 83], these carbon rich zones are believed to be a mixture between M/A constituents and retained austenite containing a significant lower amount of carbon than the predicted by the lever rule at the coiling temperature.

If all the untransformed austenite remains metastable in the initial microstructure, nucleation is not necessary and austenite growth would start when the alloy is heated to the T_{S} temperature calculated above.

On the other hand, if at low temperatures all the austenite transforms into martensite, the reverse transformation upon heating would be energetically favorable a lower temperatures than the previous case. However, the volume fraction of austenite that forms from the martensite, given by the lever rule (considering a system with a carbon content of x_{c}^{γ}), will be lower than the initial volume fraction of martensite (carbon-rich second phases) until the carbon concentration of the new austenite reaches $x_{\mathrm{c}}^{u\gamma}$. Hence, the total fraction of austenite will not overcome the initial volume fraction of austenite until temperatures reach T_{S}.

A more plausible mixed sceneario, where the carbon-rich second phases are constituted by M/A constituents will involve a more complex sequence of austenite formation but the limiting start transformation temperature will lie in between the aforementioned scenarios.

The value of T_{s} is subjected to CT (coiling temperature) and T_0' selected. A change in the coiling temperature or strain energy due to the formation of bainite will have a direct influence on the T_{s} value. However, A_{c3}' slightly changes with the carbon content and a shift of 50 °C of CT or a decrease of 200 J/mol in the energy stored would lead to approximately 20 °C difference on the predicted T_{s}. It is important to remark that the volume fraction of carbon-rich second phases is significantly low, and a partial transformation

into austenite is not be detectable with the current technique. Therefore, the experimental A_{c1} is likely related to the temperature at which austenite is energetically free to grow, T_S. At heating rates as slow as at 1 °C/s, the obtained A_{c1} (780°C) lies between these two scenarios and is in good agreement with the T_S temperature proposed following Yang et al. [65] reaustenitization theory for of acicular ferrite. Values reported in literature of ferrite to austenite formation temperatures for similar alloy compositions but with lower [3, 16, 68, 71, 84] and comparable [61, 62] heating rates show A_{c1} temperatures similar to those observed in this work.

Partial transformation experiments reaching 750°C (below T_s but above A_{e1}) indicated not presence of austenite when the quench followed directly from the heating. For the case when there was a 20 s anneal at the peak temperature, the granular bainitic zones showed evidence of transformation starting at the carbon rich zones. This is consistent with the absence of substitutional alloying elements diffusion during heating, and the presence of enough diffusion during the hold, to drive a transformation through a possible partition mechanism controlled by Mn diffusion, to reach after 300 s an austenite fraction comparable with the ortho-equilibrium conditions calculated at the annealing temperature.

As the heating rate increases, A_{c1} approaches to 810°C which is similar to the estimated A_M. At this temperature, there is no energy restriction for the ferrite to transform into austenite without composition change.

More experimental and theoretical support is necessary to affirm that the transformation occurs through a partitionless mechanism. Nevertheless, the experimental results and literature evidence suggests that to model the kinetics of austenite formation at high heating rates it should be considered at least as a coupled mechanism [42, 45, 85]

2.6 Conclusions

Austenite formation during continuous heating on a grade X80 pipeline steel of composition according to Table 4.1Chemical composition of the X80 alloy studied (wt%).table.caption.47 with an initial ferritic and bainitic microstructure (Figure 2.2(a) Optical and (b) SEM micrographs of granular bainitic zones of the initial microstructure.figure.caption.17) was studied by dilatometric analysis and electron microscopy.

A continuous heating transformation diagram (CHT) was developed for heating rates varying from 1 to 500°C/s (Figure 2.4Continuous heating transformation diagram of the studied alloyfigure.caption.20).

At the slower heating rates tested (below 10°C/s), the austenite start transformation temperature A_{c1} is higher than the one dictated by the equilibrium (A_{e1}) by approximately 100°C. The A_{c1} determined (780°C at 1°C/s) is in good agreement with the transformation temperatures predicted by the

effect of an incomplete transformation to bainite at the coiling temperature (785°C). However, specific information about the processing conditions are need to make more accurate predictions and comparisons with experimental values.

As the heating rate increases, A_{c1} shifts to higher temperatures and gradually approaches the A_M temperature, determined thermodynamically (810 °C).

On the other hand, the finish transformation temperatures are also higher than the one dictated by the equilibrium. A_{c3} not only increases significantly with heating rate, but also showed a modest increase trend for low heating rates.

Above A_M, austenite nucleation and growth is thermodynamically feasible from ferrite without change in composition. The occurrence of transformation near this temperature and the thermodynamic feasibility of a interface controlled phase transformation suggests that these steels of very low carbon might involve significant amounts of massive transformation during fast heating. Current research is evaluating this possibility.

Interrupted transformation experiments with a maximum temperatures of 835°C and above were performed at an intermediate heating rate (100°C/s) followed by fast cooling (600°C/s). In these experiments the bainitic zones surrounding untransformed larger polygonal ferrite grains showed evidence of

transformation during cooling, indicating that the austenitic transformation starts in the bainitic zones of the starting microstructure, followed by transformation of pro eutectoid ferritic grains. And these phenomena, can explain the occurrence of two different stages during the structural transformation.

2.7 Acknowedgements

The authors gratefully acknowledge funding support from the AWS Foundation Graduate Fellowship, the Roberto Rocca Educacion Program, and NSERC, as well as samples donated by EVRAZ Canada. Also acknowledged are much helpful conversations with Dr. T. Lienert, Professors M. Kaufman, F. Castro Cerda, and B. Wiskel.

Chapter 3

Kinetics of austenization during heating accounting for solute drag and Mn redistribution

Abstract

A Gibbs free energy balance (GEB) model was developed to study the non-isothermal austenite reversion in a commercial X80 pipeline steel at heating rates of 1 °C/s and 200 °C/s. The model accounts for the energy dissipated by the friction of the interface, the solute drag of Mn, and the chemical driving force for available transformation. The original solute drag expression was extended to account for Mn redistribution at low interface velocities. A novel methodology was developed to calculate the chemical driving force for transformation under paraequilibrium conditions as a function of the temperature and the transformed fraction. With only one adjustable parameter the transformation kinetics predicted by the GEB model describes the two different kinetic regimens observed with the dilatometric measurement. The new model is able to capture with reasonable accuracy both fast and slow heating rates, and does not require additional fitting parameters beyond the single one required to modify the original solute drag model.

3.1 Introduction

Phase transformations in alloys involves two different processes such as the redistribution of alloying elements between the parent and product phase, and the rearrangement of atoms into a different crystal structure. Depending on which process consumes the available driving force, the transformation rate is said to be diffusion or interface controlled. In the past, plenty of effort has been focused on describing phase transformations with classical models of diffusion [86] or interface controlled [87] models. However, scarcely cases of practical phase transformations in alloyed steel present pure characteristic of one or the other mechanisms, and they usually present combined characteristics of both mechanisms.

The mixed models for α-γ transformation, in which a finite interface mobility and the solute diffusion are considered simultaneously, represent a valuable tool to understand and predict the transformation kinetics for austenite decomposition and formation in carbon steels [88–90]. Recently, Chen et al. [91,92] proposed a novel approach to study mixed mode transformations involving a Gibbs free energy balance (GEB) at the interface. The model is based on a balance of energies consumed by solute diffusion of alloying atoms, the movement of the boundary, and the chemical driving force

available for transformation. Successfully results were obtained modelling kinetics of austenite decomposition into bainite [91, 92] and/or ferrite [93–97]. However, limited number of studies were focused on the reverse transformation [95, 97, 98].

Generally speaking during austenite formation during heating, the chemical driving force increases with temperature. On the other hand, the diffusivity of alloying elements and therefore the capability to redistribute between phases increases as well with the temperature. Then, at high temperatures, a complex interaction between the boundary migration rate and the mobility of solute atoms within and in front of the interface requires a special attention to understand the different energy dissipation sources at the boundary.

In this study, the kinetics of α to γ transformations during continuous heating in a low carbon microalloyed steel will be investigated with dilatometry and later studied with a energy balance approach accounting for the energy dissipated by the diffusion of Manganese within the interface and the energy dissipated by the re arrangement of the crystal structure. To apply a solute drag model, the complex multicomponent material was reduced to a fictitious binary system under the condition that the interface moves sufficiently high for substitutional alloying elements to form a concentration profile in front of the moving interface. Later a modification of the solute drag model is proposed to extend the analysis to interface velocities comparable to Mn mobility in the bulk parent grains. The energy dissipation

components at the interface were combined with a systematic procedure to evaluate the chemical driving force as a function of the transformed fraction to calculate transformation kinetics of austenite formation during continuous heating for two different heating rates.

3.2 Experimental Procedure

The studied material is commercial X80 steel which chemical composition is presented in table 3.1Chemical composition of the X80 alloy studied (wt%).table.caption.27.

Table 3.1: Chemical composition of the X80 alloy studied (wt%).

C	**Mn**	**Si**	**Cr + Cu + Ni**	**Mo**	**Nb**	**V**	**Ti**	**Al**	**N**	**Fe**
0.03	1.7	0.27	0.45	0.297	0.091	0.002	0.017	0.044	0.0098	bal.

Cylindrical hollow dilatometry specimens (10 mm in length and 4 mm in diameter, with a 3 mm hole) were extracted from the provided skelp from a fixed depth of the surface to avoid the extraction of samples with traces of the typical centreline microsegregation [69, 70]. Continuous heating experiments were performed with a high-resolution quench L-78 RITA Linseis dilatometer. To study the influence of the heating rate on the austenite formation, fully austenitization cycles up to 1050 °C followed by an immediate rapid cooling (400°C/s) were performed at two different heating rates, 1 °C/s and 200 °C/s. Additional interrupted heating experiments to peak temperatures of 780 °C, 820 °C, and 850 °C followed by immediately rapid cooling

were performed to study early stages of austenite formation for both studied heating rates. All tests were performed at a constant pressure of inert gas Helium and the temperature was controlled by a K-type thermocouple spot welded to the midsection of each specimen. The kinetics of austenite formation upon heating were derived from the dilatation curves using the lever rule methodology. The average values and the standard deviation of three experiments were used to construct the transformation curves and experimental error respectively at each velocity. The transformation start and finish temperatures were defined as the temperatures at which 4% and 97 % of the transformation is completed respectively.

The samples were cross-sectioned, polished, and etched with 2% Nital to be examined by Optical (OM) and Field Emission - Scanning Electron Microscopy (SEM) Zeiss Sigma 300 VP-FESEM with an operating voltage of 5 to 15 KeV. grain size measurements were performed according to reference [99]. Phase quantification was performed on 5 - 7 micrographs per condition utilizing an image software analysis ImageJ, the volume fraction reported and the error represent the average and the standard deviation respectively.

3.3 Experimental Results

3.3.1 As Received Material

Th microstructure of the as-received condition consists in a complex structure formed by large polygonal ferrite surrounded by smaller bainitic ferrite grains forming a pancake structure, typical from these type of thermomechanical processed steels (X80 grade), Figure 3.1SEM micrograph of the (a) as-received microstructure and (b) magnification of the FC aggregates figure.caption.28 (a). The average ferrite grain size and the standard deviation were 2.45 and 0.8 μm respectively . Additionally to the ferritic structure, block-like zones, no larger than 2 μm in thickness, where identified as ferrite and carbide (FC) aggregates. A detailed characterization via electron back scattered diffraction (EBSD) revealed that the matrix, composed by bcc iron, contains flake-like cementite, (M_3C). Quantification by optical and SEM revealed that the FC zones occupy $\backsim$ 2 % of the initial microstructure. Microalloyed precipitates, from now on referred as MX with M=(Nb, Ti, Mo) and X=(C,N), were found in the as-received material in three main types of MX Ti-rich, Nb-rich and Nb-Mo rich precipitates by Lu [75]. Thus, the available carbon to participate during the reverse transformation to austenite will be given the difference between the initial content and the carbon trapped to the MX precipitates, approximately $x_{\mathrm{c}} = 0.02$ wt.%, according the mass balance [99].

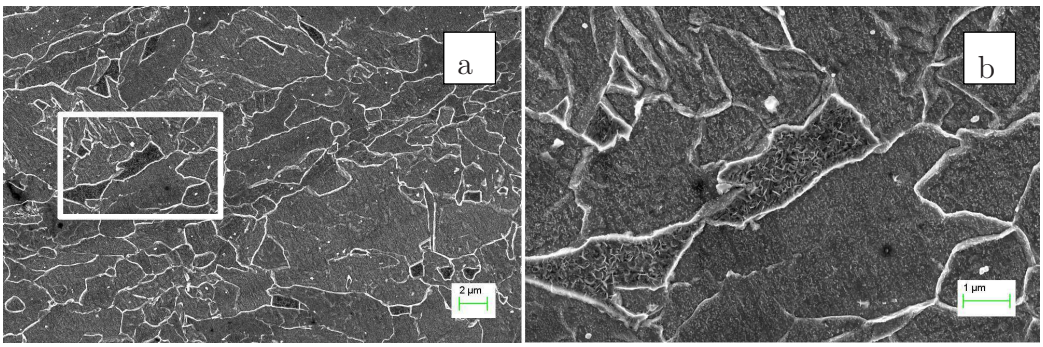

Figure 3.1: SEM micrograph of the (a) as-received microstructure and (b) magnification of the FC aggregates

3.3.2 Dilatometry Experiments

The transformation times and temperatures for both heating rates are presented in Table 3.2Measured austenite transformation temperatures and times for both heating ratestable.caption.29, and the transformed fraction curves are shown in Figure 3.2Austenite fraction as a function of temperature for the para-equilibrium calculations and both experiments. Error bars represent the standard deviation of the transformed fraction at each temperature. Red and black solid circles represent metallographic quantification of partially transformed samples at 1 and 200 °C/s respectively.figure.caption.30. To highlight the kinetic difference between both experiments, the times required to complete each transformation are reported.

HR [°C/s]	A_{c1} [°C]	A_{c3} [°C]	time [s]
1	795 ± 10	885 ± 15	> 100
200	815 ± 15	935 ± 20	< 1

Table 3.2: Measured austenite transformation temperatures and times for both heating rates

In Figure 3.2Austenite fraction as a function of temperature for the para-equilibrium calculations and both experiments. Error bars represent the standard deviation of the transformed fraction at each temperature. Red and black solid circles represent metallographic quantification of partially transformed samples at 1 and 200 °C/s respectively.figure.caption.30 the transformed fraction with the estimated experimental error for each heating rate, and the the calculated para-equilibrium fraction are plotted as a function of the temperature. The red and black solid circles represent the estimated transformed fraction via metallography, for interrupted austenization cycles when possible. Due to the low carbon content, the transformation products of the austenite formed at high temperatures become difficult to discern from the as received microstructure as the transformation progresses, hence no volume fraction was measured for the interrupted cycle at 850 °C for the 1 °C/s experiments.

The microstructural characterization of the sample heated at 1 °C/s and quenched from 780 °C, revealed that γ starts to nucleate below this temperature, Figure 3.3Optical Micrographs of (a) the As-Received microstructure, and samples quenched from 780 °C with heating rates of (b) 1 °C/s, and (c) 200 °C/s. figure.caption.31 (b). Quantification of partially transformed zones

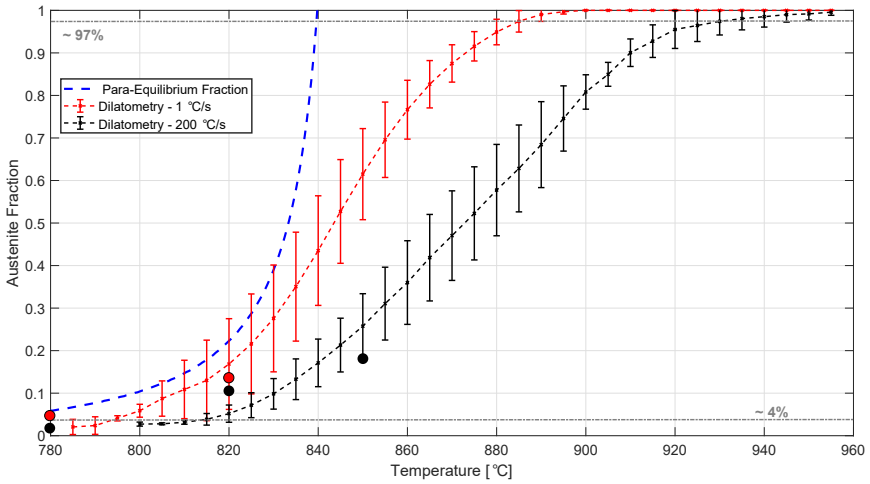

Figure 3.2: Austenite fraction as a function of temperature for the para-equilibrium calculations and both experiments. Error bars represent the standard deviation of the transformed fraction at each temperature. Red and black solid circles represent metallographic quantification of partially transformed samples at 1 and 200 °C/s respectively.

revealed 5 ± 0.6 % of transformation. Although, there is metallographic evidence of nucleation and growth at 780 °C, the current dilatometric technique was no able to detect an elongation change associated to the phase transformation until temperature reached approximately 790 °C. The density of austenite nuclei is larger than the density of the FC zones in the as-received condition. Thus, α grain boundaries and triple point must also serve as nucleation sites for γ at this heating rate, this observation is also supported by the micrographs of sample quenched from 820 °C, Figure 3.4SEM micrograph of the sample partially transformed to 820 °C at (a) 1 and (b) 200 °C/s figure.caption.32 (a). The quantified transformed area is 11 ± 1.4%.

The optical micrographs of sample heated at 200 °C/s and quenched from 780 °C, Figure 3.3Optical Micrographs of (a) the As-Received microstructure, and samples quenched from 780 °C with heating rates of (b) 1 °C/s, and (c) 200 °C/s. figure.caption.31 (c) shows a similar microstructure and distribution of the FC zones located in the ferrite grain boundaries (dark zones) compared to the initial condition, Figure 3.3Optical Micrographs of (a) the As-Received microstructure, and samples quenched from 780 °C with heating rates of (b) 1 °C/s, and (c) 200 °C/s. figure.caption.31 (a). SEM characterization of samples quenched from 820 °C, Figure 3.4SEM micrograph of the sample partially transformed to 820 °C at (a) 1 and (b) 200 °C/s figure.caption.32 (b), revealed that only a partial transformation of the FC zones into austenite at high temperatures for the fast heated sample. Leading to the conclusion that at high heating rates, austenite growth is initially restricted to the former FC zones.

The linear nuclei density, ρ_l, was estimated counting the number of intersected nuclei over a fixed length line. The microstructure of the sample quenched from 780 °C and the as-received microstructure were used to calculate the nuclei density for the transformation at 1 °C/s and 200 °C/s respectively.

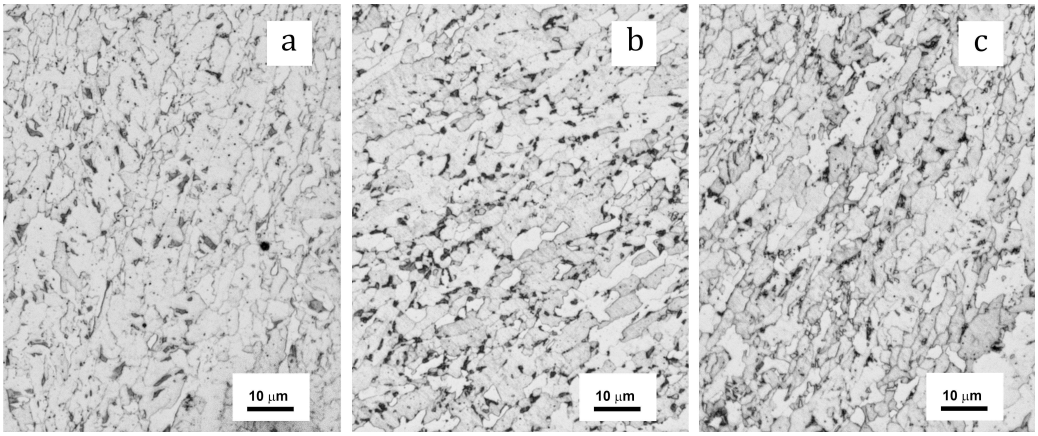

Figure 3.3: Optical Micrographs of (a) the As-Received microstructure, and samples quenched from 780 °C with heating rates of (b) 1 °C/s, and (c) 200 °C/s.

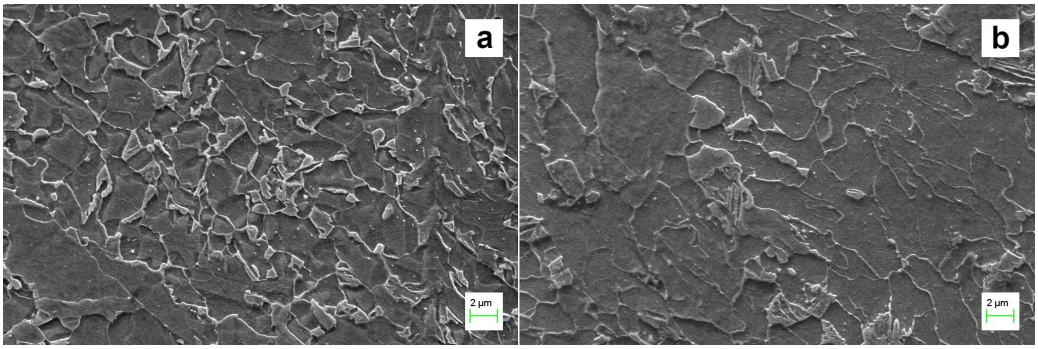

Figure 3.4: SEM micrograph of the sample partially transformed to 820 °C at (a) 1 and (b) 200 °C/s

Estimation of Interface Velocity

The interface velocity during the $\alpha \rightarrow \gamma$ transformation was estimated using Kempen et al. [100] methodology. According to the equations proposed by the authors, the calculated interface velocity as a function of the temperature (or transformed fraction) is sensitive to the impingement model chosen which relates the transformed fraction, f, with $x_e = \frac{V_e}{V_0}$ where V_e and V_0 are the extended and initial volume respectively. In the present work, the results obtained with the impingement model chosen by Kempen ($f = \tanh(x_e)$), equation 3.1Estimation of Interface Velocityequation.3.3.1 and the results using the Austin-Ricketts model [101] ($f = 1 - \frac{1}{1+x_e}$), equation 3.2Estimation of Interface Velocityequation.3.3.2 were calculated to obtain a range of interface velocities as a function of the transformed fraction.

$$df/dt = 3\ (N^* g)^{1/3}\ (1 - f^2)\ v_{\text{int}}\ \ \text{arctanh}^{2/3}(f) \tag{3.1}$$

$$df/dt = 3\ (N^* g)^{1/3}\ (1 - f)^2\ v_{\text{int}}\ [\frac{1}{1-f} - 1]^{2/3} \tag{3.2}$$

where the f is the transformed fraction, N^* is the density of nucleis per volume, g is a growing geometric factor (taken as g=1 cubic growth) and v_{int} is the interface velocity. The transformed fraction and its derivative were obtained from the dilatometric data and the nuclei density was calculated as $N^* = \rho_1^3$. The values obtained for the sample heated at 1 and 200 °C/s are $N^* = 9.9 \times 10^{14}$ and $N^* = 1.3 \times 10^{14}$ [1/m^3] respectively.

3.4 Phase Transformation Model

During any ferrite-austenite transformation in Fe-C systems, Carbon atoms redistributes between both phases. For the case of austenite decomposition during cooling, the interstitial atoms partition into the remaining austenite. However, during the reverse transformation the carbon enrichment of austenite occurs due to the long rage diffusion across ferrite grains from carbon rich zones. Simultaneously, the transformation will involve the jumping of iron atoms across the interface from a one crystal structure to another depending on the transformation direction.

For Fe-C-X systems *(X=substitutional alloying elements)*, additional redistribution of element X may occur. During this process, atoms segregate to the interface also exerting a solute drag effect. This latter effect will consume energy available at the interface for the crystal structure re-arrangement.

For the studied transformation case, due to the low carbon content of the initial microstructure and the high diffusion coefficient of C in ferrite (specially at high temperature) it will be assumed that carbon can rapidly redistribute between both phases as the interface advances. On the other hand, due to the large difference in diffusivities of interstitial and that of substitutional elements (e.g. Mn) it will be initially assumed that Mn does not partition as the interface moves. Then, para-equilibrium conditions will

be adopted to quantify the effect of trans-interface diffusion of Mn (i.e. solute drag) and calculate chemical driving forces. A modification of the model to account for the possible redistribution of Mn is proposed to extend the analysis to relatively low interface velocities.

3.4.1 Gibbs Free Energy Balance at the Interface

A model based on a Gibbs free Energy Balance (GEB) is utilized to describe the kinetics of ferrite to austenite transformation. This approach consists in a energy balance across a control volume that involves the interface. Assuming that the interface has a thickness of $2b$ and it moves with a certain velocity v_{int}, the Gibbs free energy balance over the control volume indicated by the dashed line in Figure 3.5Schematics of the interface and the defined control volume for the energy balance.figure.caption.34, can be written as follows:

$$G_{\text{in}} - G_{\text{out}} + G_{\text{gen}} = G_{\text{st}} \tag{3.3}$$

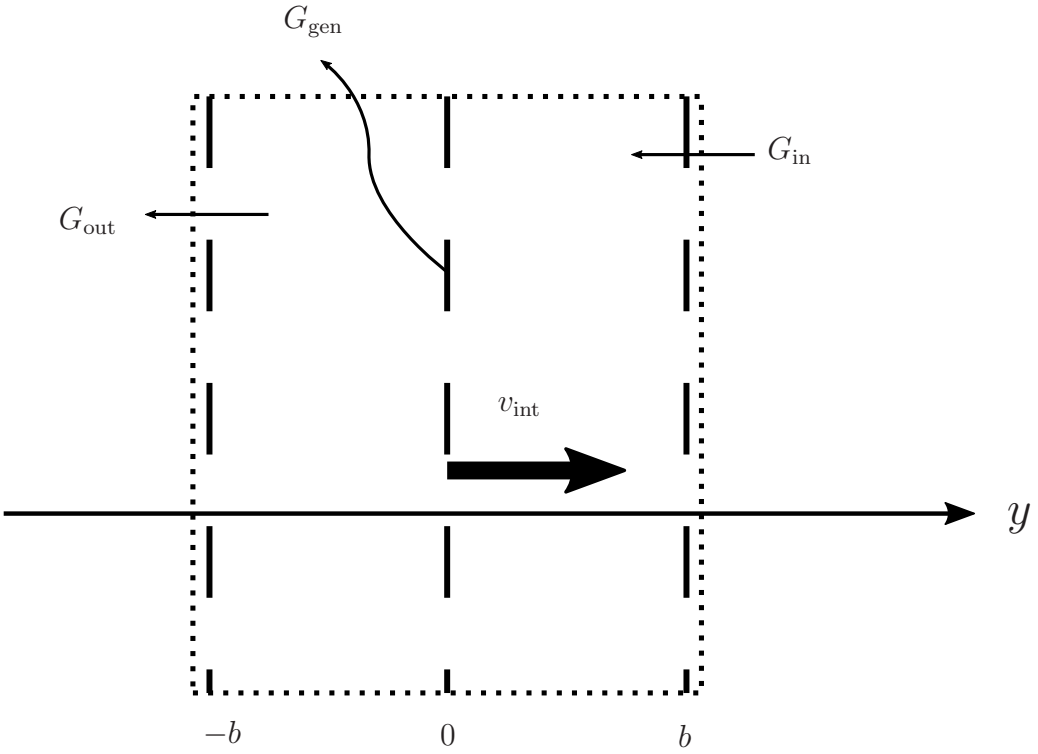

Figure 3.5: Schematics of the interface and the defined control volume for the energy balance.

where the first two terms in the left side of the equation 3.3Gibbs Free Energy Balance at the Interfaceequation.3.4.3 can be related with the available chemical driving force for the transformation (ΔG^{chem}). If the surface energy contributions are neglected, the G_{gen} is composed by two components (a) the energy dissipated by the diffusion of alloying elements (ΔG^{diff}) and (b) the energy consumed by the actual jumps of atoms from one crystalline arrangement to the other (ΔG^{fric}), often referred as energy dissipated by friction. If there is no net stored energy, $G_{\text{st}} = 0$, the balance of Gibbs free

energies will yield the following relationship:

$$\Delta G^{\text{chem}} = \Delta G^{\text{diff}} + \Delta G^{\text{fric}} \tag{3.4}$$

In the following sections, each energy component will be described and calculated to later determine the boundary migration rate using the GEB approach.

Energy Dissipated by Diffusion inside the Interface

The effect of the interaction of solute atoms with moving interfaces was first introduced by Cahn [102] and Lucke and Stuwe [103] as the concept of "solute drag" effect to explain discrepancies between calculated and experimental grain growth kinetics in alloys. Later Purdy and Brechet [104] extended Cahn's theory to moving boundaries for phase transformations.

In the present work, the model proposed by Purdy and Brechet will be used to quantitative describe the interaction of Mn solute with the moving γ/α interface due to its mathematical simplicity. This model assumes that the interface can be represented by a finite region in which the chemical potential of the solute atoms is described by a wedge function which will exert a driving force for atoms to segregate inside the interface while this one moves with a certain velocity, Figure D.1Schematics of the interface and the potential well proposed by reference by the solute drag modelfigure.caption.60

(Appendix DDerivation of the solute drag modelappendix.D). For each temperature (time) step steady state conditions are assumed and the product phase, γ, is considered to inherit the initial Mn content of the alloy (partitionless respect Mn).

The calculation procedure requires first to solve a diffusion equation (equation D.1Derivation of the solute drag modelequation.D.0.1, in Appendix A) inside and adjacent to the interface to later use Cahn's approach to calculate the energy dissipated by solute drag (equation D.10Derivation of the solute drag modelequation.D.0.10). The detailed calculation of ΔG^{diff}, according reference [104], can be found in Appendix DDerivation of the solute drag modelappendix.D.

The concentration profile and hence the value of ΔG^{diff} are sensitive to the interface model parameters. From equation D.1Derivation of the solute drag modelequation.D.0.1 and D.10Derivation of the solute drag modelequation.D.0.10 it can be noted that: the binding energy (E_0), the difference in chemical potentials (ΔE), the diffusion coefficient (D^b), and the interface thickness ($2b = \delta$) are the characteristic parameters of this model and they will have a strong influence on the final ΔG^{diff} value.

Asymptotic Regimes of the Solute Drag Model

At infinitely large interface velocities, the energy associated to the solute drag pressure will tend to zero since the interface will move too fast to interact with the solute atoms. On the other hand, when the interface velocity tends to zero, a stationary interface does not interact with the solute atoms and the energy associated with solute drag must be null. However, the model proposed by Purdy and Brechet is not consistent with the latter asymptotic regimen. It has been shown by Hillert et al. [105, 106] that when ΔE is different from zero (the case of phase transformations), the limit of the energy associated to the solute drag when $v_{\text{int}} \rightarrow 0$ is associated to the diffusion profile in front of the moving interface.

Thus in the present work, a new expression for ΔE is proposed to adapt the solute drag model for when the interface moves slow enough such Mn can partially redistribute. To mathematically describe the diffusion of Mn towards the interface equation 3.5Asymptotic Regimes of the Solute Drag Modelequation.3.4.5 was employed. In Appendix EModification of the solute drag modelappendix.E the derivation of equation 3.5Asymptotic Regimes of the Solute Drag Modelequation.3.4.5 is presented.

$$\Lambda = 1 - [\exp(k_a)\ \text{erfc}(\sqrt{k_a})] \tag{3.5}$$

where Λ is a dimensionless variable that relates the Mn concentration at the interface. k_a is an dimensionless parameter defined in equation 3.6Asymptotic Regimes of the Solute Drag Modelequation.3.4.6, that contains the interface velocity, the characteristic length of a parent grain size and interface, the diffusion coefficients of Mn in austenite and in the boundary and a adjustable parameter β. The solution suggested in equation 3.5Asymptotic Regimes of the Solute Drag Modelequation.3.4.5 was proposed due to the similarities with the physical problem of a semi infinite solid with surface convection solution.

$$k_a = \frac{(D^b)^2 \; L_c \; (\beta)^2}{(\delta)^2 \; D^{\gamma}_{\mathrm{Mn}}} \tag{3.6}$$

The asymptotic limits of this solution satisfies that Λ tends to zero when $v_{\mathrm{int}} >> 1$ μm/s (Mn diffusion is negligible) and to the unity when $v_{\mathrm{int}} <<< 1$ μm/s, equilibrium concentrations at the interface are satisfied.

Then the corrected ΔE_c can be expressed with the following equation, as a function of Λ and ΔE_0, calculated as if the transformation does not involve Mn redistribution.

$$\Delta E_c = \Delta E_0 \; (1 - \Lambda) \tag{3.7}$$

According to equation 3.7Asymptotic Regimes of the Solute Drag Modelequation.3.4.7, at high interface velocities ΔE_c approaches to ΔE_0. And as the v_{int} decreases, ΔE_c will tend to zero which is the limit for diffusion controlled transformations.

Finally, the energy dissipated by the solute drag effect can be calculated with Purdy's model using the methodology described in Appendix A, but introducing the new expression of ΔE_c.

3.4.2 Chemical Gibbs Free Energy

In the present work, para-equilibrium conditions have been adopted to calculate thermodynamic chemical driving force, ΔG^{chem}, when the interface velocity sufficiently large compared to Mn diffusivity in the parent phase. Then ΔG^{chem} is a function of the Gibbs free energy of each phase which depends on the the temperature and transformed fraction *(i.e. carbon content at the interface)*.

To quantify the thermodynamic functions of α and γ under this constrained form of equilibrium an intervention of the ThermoCalc data base was perform to describe the system as a fictitious binary Z-C, where Z contains all the thermodynamic information of the substitutional alloying elements. The mathematical procedure can be found somewhere else [107].

In Figure 4.3Equilibrium Z-C binary diagram illustrating the calculation of ΔG^{chem} figure.caption.46 the binary diagram Z-C is plotted for a given temperature inside the two phase field. The carbon composition of ferrite and austenite is determined by the tangent lines to the free energy curves such that the chemical potentials of carbon in both phases are equal and the amount of phases (given by the lever rule) satisfy the experimental condition. As the transformation proceeds, austenite and ferrite composition will change such that the tangent lines will shift to match a unique equilibrium tangent. Then, for any given transformation fraction the chemical driving force is for the ferrite to austenite transformation is given by equation 3.8Chemical Gibbs Free Energyequation.3.4.8.

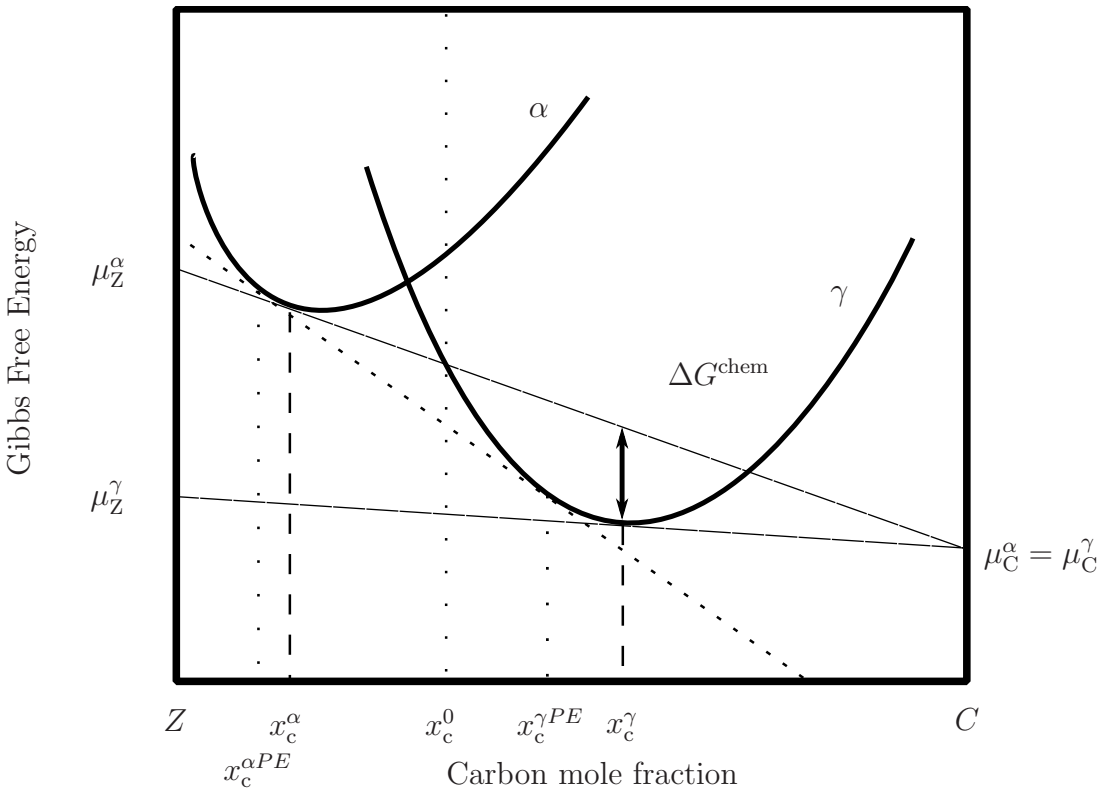

Figure 3.6: Equilibrium Z-C binary diagram illustrating the calculation of ΔG^{chem}

$$\Delta G^{\mathrm{chem}} = x_{\mathrm{C}}^{\gamma}\,[\mu_{\mathrm{c}}^{\gamma} - \mu_{\mathrm{c}}^{\alpha}] + (1 - x_{\mathrm{C}}^{\gamma})\,[\mu_{\mathrm{Z}}^{\gamma} - \mu_{\mathrm{Z}}^{\alpha}] = (1 - x_{\mathrm{C}}^{\gamma})\,[\mu_{\mathrm{Z}}^{\gamma} - \mu_{\mathrm{Z}}^{\alpha}] \quad (3.8)$$

Similarly to ΔE_c, the Gibbs free energy available for the transformation will also have an asymptotic behavior. At sufficiently high in interface velocities, the para-equilibrium condition is satisfied and the value of ΔG^{chem} is given by equation 3.8Chemical Gibbs Free Energyequation.3.4.8. How-

ever, as the interface velocity decreases, substitutional alloying elements may redistribute such that at at extremely low migration rates the equilibrium conditions are satisfied and the driving force tends to zero. Similarly to the correction employed in equation 3.7Asymptotic Regimes of the Solute Drag Modelequation.3.4.7, the available Gibbs free energy for the transformation as a function of the interface velocity is given by the following equation:

$$\Delta G_{\mathrm{c}}{}^{\mathrm{chem}} = \Delta G^{\mathrm{chem}} \, (1 - \Lambda) \tag{3.9}$$

where Λ is defined in equation 3.5Asymptotic Regimes of the Solute Drag Modelequation.3.4.5.

3.4.3 Energy Dissipated by Friction

According to the theory of interface controlled processes [87], the energy dissipated by friction of the interface is given by the following equation:

$$\Delta G^{\mathrm{fric}} = v_{\mathrm{int}}/M \tag{3.10}$$

where v_{int} is the interface velocity and M is the mobility of the α/γ interface. It is generally accepted that M exhibits a Arrhenius dependence with temperature as equation 3.11Energy Dissipated by Frictionequation.3.4.11 suggests.

$$M = M_0 \exp(-Q/RT) \tag{3.11}$$

where M_0 is the pre-exponential factor, and Q is the activation energy. Similarly to the characteristic parameters of the solute drag effect, M_0 and Q will have a strong influence of the energy balance. The activation energy value does not present much controversy in literature, and its yield values between 135 - 150 kJ mol^{-1} according to [108, 109].

On the other hand, reported M_0 values in literature vary between 0.05 - 3 m mol / J s [94,95,110,111]. In the present work, the intrinsic value of M_0 will be calculated, according to the theory of interface controlled transformations [87]:

$$M_0 = \delta\omega/R\ T \tag{3.12}$$

where $\delta = 0.5$ [nm] is the thickness of the interface and $\omega = k\ T/h$ is the frequency for the atoms jumping over the interface (function of the temperature, Planck and Boltzmann constants). Equation 3.12Energy Dissipated by Frictionequation.3.4.12 yields a value of $M_0 = 1.38$ m mol / J s. Then the energy dissipated by the friction of the interface can be calculated as function of the velocity for different temperatures with equation 3.10Energy Dissipated by Frictionequation.3.4.10.

3.5 Model Results

3.5.1 Characteristic Parameters

To reduce fitting variables of the model, the diffusivity of the interface, D^b was taken as the geometric average between the bulk diffusion coefficient of Mn in both phases. The diffusion coefficients of austenite and para-magnetic ferrite were obtained from reference [112]. The interface thickness $2b$ was set as 0.5×10^{-9} m [95, 96, 98, 111] and the initial characteristic length of the parent phase, L_c, as 1.2×10^{-6} m according to the results obtained in previous section. Various binding energy values varying between 5 - 10 kJ/mol have been reported in literature [91, 92, 97, 98]. Alternative studies suggested a linear dependence of E_0 with the temperature, where the value of the binding energy is in the order of RT, the product of the gas constant R and the temperature [94, 96]. In the present work, the E_0 was taken as 8 kJ/mol, which represents an intermediate value among the reported ones.

To calculate ΔE_0, the chemical potentials were obtained with Thermo-Calc software (database TCFE10). The value of $\mu_{\mathrm{Mn}}^{i/int}$ $(i = \alpha, \gamma)$ is a function of the temperature and chemical composition. Thus, for each temperature step the value was re-calculated considering the amount of carbon content in both phases given by the transformation progress and para-equilibrium constrains. The ΔE_0 calculated with the chemical potentials decreases with temperature and yield values from 3 to 2 kJ/mol between 800 °C and 950 °C respectively.

The activation energy of the intrisic mobility , Q, was taken as 140 kJ mol $^{-1}$ according to the reported ones in literature [108, 109], and the value of the pre-exponential factor was calculated according equation 3.12Energy Dissipated by Frictionequation.3.4.12, $M_0 = 1.38$ m mol / J s.

Then, β from equation 3.6Asymptotic Regimes of the Solute Drag Modelequation.3.4.6 is the only adjustable parameter in the present model. As it was mentioned in previous section, equation 3.5Asymptotic Regimes of the Solute Drag Modelequation.3.4.5 describes the solute concentration at the interface in terms of the boundary migration rate with respect of the diffusion in the parent phase and across the interface. In Appendix EModification of the solute drag modelappendix.E the derivation of the parameter k_a is presented. In the present work the adjustable variable, β, was taken as 0.002.

3.5.2 Gibbs Free Energy Balance

A description of the kinetics of the $\alpha \rightarrow \gamma$ transformation was obtained with the described model. The blue solid curve of Figure 3.7Total dissipated (blue) and chemical Gibbs free energy as a function of the interface velocity at (a) 820 °C, (b) 860 °C, (c) 905 °Cfigure.caption.38 shows the total energy dissipated ($\Delta G^{\mathrm{T}} = \Delta G^{\mathrm{diff}} + \Delta G^{\mathrm{fric}}$), the black and red curves represent the chemical Gibbs free energies (ΔG^{chem}) for 1 and 200 °C/s experiments respectively as a function of the interface velocities. Figures 3.7Total dissi-

pated (blue) and chemical Gibbs free energy as a function of the interface velocity at (a) 820 °C, (b) 860 °C, (c) 905 °Cfigure.caption.38 a, b, and c were calculated for the following temperatures 820, 860, and 905 °C which illustrates different solutions of the energy balance .

According to the GEB approach, the interface velocity will given by equation 3.4Gibbs Free Energy Balance at the Interfaceequation.3.4.4 (*i.e. the intersection between* ΔG^T *and* ΔG^{chem}).

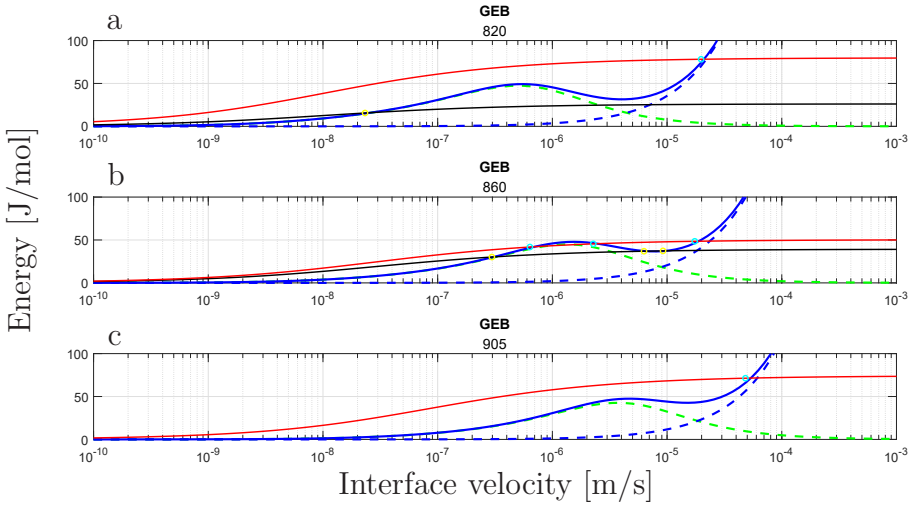

Figure 3.7: Total dissipated (blue) and chemical Gibbs free energy as a function of the interface velocity at (a) 820 °C, (b) 860 °C, (c) 905 °C

At 820 °C, for the samples heated at 200 °C/s, the intersection of the total dissipated and the chemical energy yield values of interface velocity in the order of 20 μm/s. The sample heated at 1 °C/s presents three different solutions. It has been demonstrated somewhere else [113] that the intermediate value of v_{int} represents an instability point, and any perturbation on

ΔG^{chem} would lead the system towards one of the other two stable interface velocity solutions. In section 3.3.2Dilatometry Experimentssubsection.3.3.2, it was shown that at low heating rates transformation starts before the measured A_{c1} temperature with sluggish kinetics and the transformed fraction is close to the equilibrium predictions. Then, the GEB balance with a initially small driving force and low interface velocity will adopt values according the first intersection between ΔG^{T} and ΔG^{chem}, approximately 0.025 μm/s.

In Figure 3.7Total dissipated (blue) and chemical Gibbs free energy as a function of the interface velocity at (a) 820 °C, (b) 860 °C, (c) 905 °Cfigure.caption.38 (b), the energy balance at 860 °C for the fast heating rate sample now yields three solutions as the previous mentioned case at 820 °C for the sample heated at 1 °C/s. However, in this case as the temperature increases, the interface is already moving at a rate given by the solution found of case similar to Figure 3.7Total dissipated (blue) and chemical Gibbs free energy as a function of the interface velocity at (a) 820 °C, (b) 860 °C, (c) 905 °Cfigure.caption.38 (a). Then there are no physical justification for the solution to abruptly adopt the other stable possible solution. The calculated velocity for the fast heating rate is approximately 20 μm/s. The solution for the slow heated sample does not change and the model predicts values of 0.26 μm/s.

At 920 °C, Figure 3.7Total dissipated (blue) and chemical Gibbs free energy as a function of the interface velocity at (a) 820 °C, (b) 860 °C, (c) 905 °Cfigure.caption.38 (c) the transformation for the slowly heated samples is completed. And the energy balance for the fast heating rate sample yields again only one solution for the interface velocity of 48 μm/s.

Figure 3.8experimental and calculated interface velocities for both heating rates.figure.caption.39 compares the estimated interface velocities according to equations 3.1Estimation of Interface Velocityequation.3.3.1 and 3.2Estimation of Interface Velocityequation.3.3.2 in section 3.3.2Dilatometry Experimentssubsection.3.3.2 with the calculated ones as a function of the transformed fraction for each experiments.

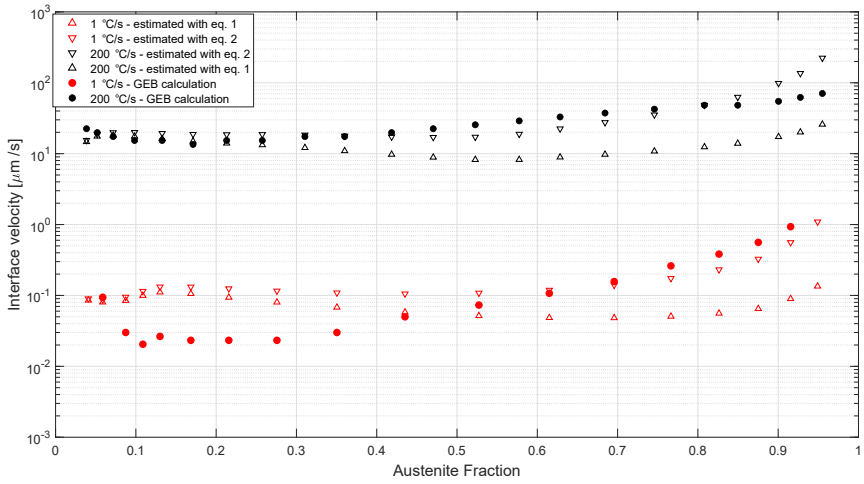

Figure 3.8: experimental and calculated interface velocities for both heating rates.

3.6 Analysis

3.6.1 Early Stages & Kinetics of Austenite Formation

It has been shown that austenite nucleation is sensitive to the heating rate. While at 200 °C/s nucleation is mostly confined to the carbon rich second phases, at low heating rates presumably the partial decomposition of the FC zones lead to the nucleation to take place also at local enriched zones such as grain boundaries, and triple points. This latter phenomena take place below the measured A_{c1} temperature by dilatoemtry and has associated stagnant kinetics which are not captured by the employed experimental technique.

From figure 3.2Austenite fraction as a function of temperature for the para-equilibrium calculations and both experiments. Error bars represent the standard deviation of the transformed fraction at each temperature. Red and black solid circles represent metallographic quantification of partially transformed samples at 1 and 200 °C/s respectively.figure.caption.30 it can be seen that dilatometry experiments present great variation within the same type of experiments, and that transformation temperatures are somehow similar between the studied heating rates. However, the times associated with the transformation are significantly different. The distinct nucleation sites and times required for the transformation to complete, suggests that the growing rate (i.e. interface velocity) of the sample heated at 200 °C is orders of magnitude higher than the experiments at 1 °C/s.

The estimated interface velocities were calculated with equations 3.1Estimation of Interface Velocityequation.3.3.1 and 3.2Estimation of Interface Velocityequation.3.3.2 which involve the derivatives of f with respect of the time obtained with the dilatometry data and a impingement model. The calculated values are reported avoiding early and late stages of transformation where mathematically df/dt does not tend to zero. The estimated velocity values were found to be sensitive to the impingement model chosen. While the factor ($f = \tanh(x_e)$) in equation 3.1Estimation of Interface Velocityequation.3.3.1 considers nucleation at the grain boundaries and hard impingement (a partitionless transformation), the Austin-Rickett correction in equation 3.2Estimation of Interface Velocityequation.3.3.2 accounts for the impingement of diffusion fields. Thus the results according the two models, which represent two different transformations mechanisms, are presented in order to show a range of estimated velocities.

Nevertheless, the calculation of a microscopic variable (such as interface velocity) from a macroscopic measurement like dilatometry relies on the accuracy of the transformation model to describe the actual phase transformation. Thus, the obtained values should be treated as estimations to emphasize the kinetic differences between both heating rates. The calculated interface positions for each set of estimated interface velocities, after the experimentally measured transformation time, are in the order of magnitude of half of the average initial ferrite grain size.

3.6.2 Predicted Kinetics of the Model

General Aspects of the Gibbs Free Energy Balance

From the total energy dissipated curves of Figure 3.7Total dissipated (blue) and chemical Gibbs free energy as a function of the interface velocity at (a) 820 °C, (b) 860 °C, (c) 905 °Cfigure.caption.38, three regimens with different kinetics can be identified. The calculated concentration profiles according to the original solute drag model are plotted for three different velocities at 860°C Figure 3.9Calculated Mn concentration profile across the interface for different boundary migration rates according to the original solute drag model [104].figure.caption.41, to visualize the different regimen.

At high interface velocities, the solution to the diffusion equation yields a flat Mn profile across the parent grain and interface, solid black line in Figure 3.9Calculated Mn concentration profile across the interface for different boundary migration rates according to the original solute drag model [104].figure.caption.41. This suggests that Mn does not interact with the moving boundary and the energy is solely consumed by the re arrangement of the crystal structure (ΔG^{fric}).

At intermediate velocities, due to the difference in diffusion coefficients and characteristic lengths of the boundary and the parent grains, the model yields a Mn profile inside the interface but the concentration profile in front of the boundary is only a few times the thickness of the interface which is negligible compared to parent grain size, dashed profile in Figure 3.9Calculated

Mn concentration profile across the interface for different boundary migration rates according to the original solute drag model [104].figure.caption.41. Then, there will be energy dissipated by trans-interface diffusion (solute drag) or friction, but partition of Mn in the parent grain is negligible.

As the interface velocity decreases, the Mn profile in front of the boundary becomes comparable with the initial grain size and redistribution of Mn should be taken into account. And at extremely low interface velocities, the effect of solute drag is negligible and the energy dissipation will occur solely ahead of the boundary. In this extreme case the transformation is controlled by the diffusion of Mn, and stagnant kinetics are anticipated, dotted like in Figure 3.9Calculated Mn concentration profile across the interface for different boundary migration rates according to the original solute drag model [104].figure.caption.41.

In the original solute drag model, when the interface velocity approaches to zero the energy dissipated tends a finite value becasue the model cannot mathematically discern between the energy dissipated by diffusion ahead and within the interface. However, as the interface velocity decreases the negligible partition assumption cannot be satisfied and the validity of the model is compromised.

In the present work, in an effort to extend the model to lower interface velocities, the dimensionless number Λ (defined in equation 3.5Asymptotic Regimes of the Solute Drag Modelequation.3.4.5) describes the interface conditions as a function of the P_{e} number and factor k. Then the values of ΔE_{c} and ΔG^{chem}, originally calculated under para-equilibrium, are adjusted as a function of Λ to satisfy the asymptotic behavior for when solute redistribution is not negligible.

The interface velocities calculated with the present model, with only one adjustable parameter $\beta = 0.02$, are in good agreement with the experimentally estimated velocities. Additionally, the fitted k yield values of Λ such that when the interface velocity is infinitely fast compared the bulk diffusion of Mn in ferrite ($P_{\mathrm{e}} \gg 1$), transformation occurs under para-equilibrium conditions and Λ tends to zero (such that ΔE_{c} and ΔG^{chem} are calculated under para-equilibrium conditions). Then, the original solute drag model is applied and the energy will be dissipated either by ΔG^{fric} or ΔG^{diff}.

On the other hand, when the interface moves infinitely slowly ($P_{\mathrm{e}} \ll 1$), the solute drag model is modified such that the ΔE_{c} tends to zero together with ΔG^{chem}. Then, the modified model anticipates a null solute drag dissipation and the interface velocity adopt values according a diffusion controlled process.

The intermediate velocities are described by a blend of both regimens, for which the behavior is given by the value of Λ.

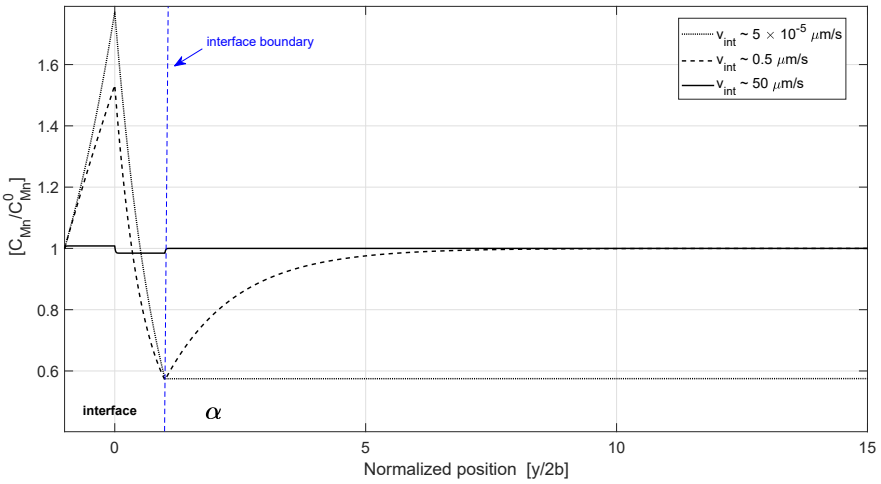

Figure 3.9: Calculated Mn concentration profile across the interface for different boundary migration rates according to the original solute drag model [104].

Slow Heating Rate - 1 °C/s

The proposed energy balance, combined with the modified solute drag model can successfully describe the boundary migration rate for all the transformation range.

At low heating rates, metallographic evidence indicates that transformation starts before the indicated temperature by dilatometry. Results from section 3.3.2Dilatometry Experimentssubsection.3.3.2 showed that nucleation and partial growth of austenite occurs at grain boundaries and triple points and that the transformed fraction at 780 °C is close to the one estimated by paraequilibrium calculations. However, the sluggish boundary migration rate

prior the measured A_{c1} temperature is not captured by the present experiments. The proposed model can successfully anticipate that the interface velocity tends to zero when the driving force is close to zero, presumable under diffusion controlled scenario.

As the transformation proceeds, the transformed fraction starts to deviate from equilibrium predictions and the intersection between the available driving force and the total energy dissipated at the interface yields values of boundary migration rates that are in good agreement with the estimated ones by dilatometry.

The considerable deviation on the measured transformed fraction as a function of the temperature must be taken into consideration when the calculated and estimated interface velocities are compared. Since, differences in the volume fraction of austenite will ultimately affect the energy balance by modifying the available chemical energy.

Fast Heating Rate - 200 °C/s

The estimated interface velocity range from the dilatometry experiments are in very good agreement with the calculated values with the proposed model. At early stages of transformation, the transformed fraction is significantly lower compared to the estimated one by equilibrium calculations, and thus driving force is large enough to overcome the local maximum of the energy dissipated due the solute drag of Mn and the Gibbs free energy balance yields a unique solution for the interface velocity given by the intersection with the

energy dissipated by friction. As the transformation proceeds, there is a temperature range in which the GEB approach presents multiple solutions for v_{int}, but there is no physical explanation for the system to abruptly change velocities. Thus, v_{int} at each temperature is given by the solution $\Delta G^{\text{chem}} = \Delta G^{\text{T}} \approx \Delta G^{\text{fric}}$. At high temperature, the driving force increases further more and the system again yields only one solution for the interface velocity.

Due to the very steep curve of energy dissipated by friction as a function of the interface velocity, a variation of the available chemical driving force will have a small effect on the energy balance. On the other hand, the temperatures at which the energy balance presents multiple solutions can also be elucidated with the errors associated to the calculation of ΔG^{chem} when there is a considerable uncertainty of the transformed fraction as a function of the temperature.

Overall, the model indicates that at high heating rates the interface velocity is given by the mobility of the interface rather than the solute drag effect. For all the transformation range, the energy balance yields interface velocities that are in good agreement with the estimated ones by dilatometry.

3.7 Conclusions

Continuous heating experiments were performed at two different heating rates to study the kinetics of austenite formation from a mostly ferritc structure in a commercial X80 steel. The measured transformation temperatures are comparable, but the time required for the transformation to complete is significantly lower at high heating rates. Metallographic observations of partially transformed samples revealed that at low heating rates austenite nucleates at second phases (ferrite and carbide aggregates), grain boundaries and triple points, while at high heating rates nucleation is restricted to the second phases present at the starting microstructure. The difference in the amount of nucleation sites per unit volume and the time necessary for transformation to complete is consistent with the fact that the interface velocities are highly sensitive to the heating rate.

A Gibbs free energy balance was performed to model the boundary migration rate of austenite formation during continuous heating as a function of the chemical driving force. For the energy balance, the energy dissipated by (a) the friction of the interface and (b) the solute drag effect of Mn was balanced with the available driving force for the transformation. In the present work, a modification of the solute drag expression is proposed to extend the model to low interface velocities.

From the experimental and theoretical calculations, the following observation can be made.

For the high heating rate experiment (200 °C/s) the model predicts a negligible interaction between the solute atoms and the moving interface, then the boundary migration is mainly controlled by the interface mobility and the driving force available for transformation. The intrinsic pre-exponential factor M_0 calculated with equation 3.12Energy Dissipated by Frictionequation.3.4.12 successfully describes the order of magnitude and the trend of the interface velocity estimated in the experiments.

For slow heating rate experiments (1 °C/s), below the measured transformation start temperature (A_{c1}) extremely low interfaces velocities were inferred with metallographic evidence. At temperatures above A_{c1}, the estimated interface velocity via dilatometry was at least two orders of magnitude lower than the high heating rates samples. The Gibbs free energy balance, successfully predicts stagnant boundary migration rates when the volume fraction is close to the required by equilibrium and as the chemical driving force increases the interface velocity is given by the balance with the energy consumed by the diffusion of solute atoms within the interface.

Chapter 4

Driving force for phase transformation of microalloyed steels under paraequilibrium conditions

4.1 Abstract

Under the Gibbs free energy balance approach, the chemical driving force represents an essential thermodynamic parameter to study the kinetics of the interface.

In the most generic form, the value of the driving force is given by the difference of Gibbs free energies at the interface between the product and the parent phase which are function of the content and chemical potential of each alloying element.

This chapter presents, a systematic procedure to calculate the chemical driving pressure at the interface for a multi component system with respect of para-equilibrium conditions is presented.

The methodology consists in reducing a Fe-X-C system to a fictitious binary Z-C system, calculating the composition of each side of the interphase according the assumed equilibrium constrains to later obtain the Gibbs free energy of each phase. The calculation of the interface composition and chemical driving pressure has been synthesized such that it is a result of a geometrical construction of the Gibbs free energy curves.

4.2 Introduction

4.2.1 Paraequilibrium Treatment

Austenite-ferrite transformations in alloyed steels involve the diffusion of interstitial and substitional alloying elements. The mobility of interstitial species, such as carbon, are orders of magnitude higher than that of substitutional ones. Then, depending on the interface velocity, the transformation can proceed under different conditions at the interface.

In particular, paraequilbrium, represents a constrained form of equilibrium in which the boundary migration rate is such that diffusivity of substutional elements in negligible but the partition of interstitial species is kinetically possible. If the product phase inherits the substitutional alloying content, their thermodynamic behavior can be expressed by one fictitious element Z. Then, a multi component system Fe-X-C under para equilibrium can be now characterized by a pseudo binary system Z-C. The derivation of the thermodynamic properties of the elements Z and C requires a thermodynamic data base, such as ThermoCalc.

With the molar Gibbs free energy expression of each phase, the driving force per mole of newly produced γ phase with respect of paraequilibrium conditions for the multicomponent system, can be calculated based on the binary Z-C.

4.2.2 Thermodynamic properties of the Z-C system

The procedure detailed in references [114–116] consists in re-write the expanded form of the molar Gibbs free energy of each phase for a binary system Z-C as a function of thermodynamic parameters of the actual multicomponent system.

According to the sublattice model and the contributions of excess of Gibbs free energy of mixing (Reldich-Kister-Muggianu model), magnetic, and atomic ordering the molar Gibbs free energy of a phase j in a binary system Z:C can be written as follows [117]:

$$G_{\mathrm{m}}^{j} = y_{\mathrm{c}} G_{\mathrm{Z:C}}^{0,j} + y_{\mathrm{VA}} G_{\mathrm{Z:VA}}^{0,j} + y_{\mathrm{C}} y_{\mathrm{VA}} L_{\mathrm{Z:C:VA}}^{0,j} + y_{\mathrm{C}} y_{\mathrm{VA}} (y_{\mathrm{C}} - y_{\mathrm{VA}}) L_{\mathrm{Z:C:VA}}^{1,j} + G_{\mathrm{Z:C:VA}}^{mag,j} \tag{4.1}$$

where y_{c} and y_{VA} are the site fractions of carbon and vacancies respectively. And the magnetic contribution is expressed as [118]:

$$G_{\mathrm{Z:C:VA}}^{mag,j} = RT \ln\left(\beta^{j} + 1\right)\, f(\tau^{j}) \tag{4.2}$$

where β^j is the average Bohr magneton of phase j and its dependence with the chemical composition is defined in Equation 4.3Thermodynamic properties of the Z-C systemequation.4.2.3. And the function f is expressed as a truncated polynomials of the variable $\tau^j = T/Tc$, which depends on the curie temperature, Tc, defined in Equation 4.4Thermodynamic properties of the Z-C systemequation.4.2.4 [118].

$$\beta^j = y_{\mathrm{C}}\beta^{0,j}_{\mathrm{Z:C}} + y_{\mathrm{VA}}\beta^{0,j}_{\mathrm{Z:VA}} + y_{\mathrm{C}}y_{\mathrm{VA}}\beta^{0,j}_{\mathrm{Z:C:VA}} + y_{\mathrm{C}}y_{\mathrm{VA}}(y_{\mathrm{C}} - y_{\mathrm{VA}})\beta^{1,j}_{\mathrm{Z:C:VA}} \quad (4.3)$$

$$Tc^j_{\mathrm{Curie}} = y_{\mathrm{C}}Tc^{0,j}_{\mathrm{Z:C}} + y_{\mathrm{VA}}Tc^{0,j}_{\mathrm{Z:VA}} + y_{\mathrm{C}}y_{\mathrm{VA}}Tc^{0,j}_{\mathrm{Z:C:VA}} + y_{\mathrm{C}}y_{\mathrm{VA}}(y_{\mathrm{C}} - y_{\mathrm{VA}})Tc^{1,j}_{\mathrm{Z:C:VA}} \quad (4.4)$$

Then, to calculate the molar Gibbs free energy of phase j as a function of the temperature and composition in the Z-C system, it is necessary to know thermodynamic parameters of equations 4.1Thermodynamic properties of the Z-C systemequation.4.2.1 - 4.4Thermodynamic properties of the Z-C systemequation.4.2.4 for that phase. To calculate the values of these parameters, it is required to extract from the Gibbs Energy System (GES)

files the thermodynamic parameters of the multicomponent alloy of each participating phase. Then, compute the thermodynamic parameters of the fictitious Z-C system using the site fractions of each alloying element, as is illustrated in the equations of Appendix B.

4.2.3 Driving Force at the interface with respect of paraequilibrium

Considering the binary system Z-C where Z atoms can arrange in two different crystal structures forming α and γ phases with particular contents of solute C. For the $\alpha \rightarrow \gamma$ transformation, the chemical driving force per mole of newly γ phase, ΔG^{chem}, is derived from the difference of chemical potentials related to the local composition on each side of the interface [106, 119]:

$$\Delta G^{\text{chem}} = x_{\text{C}}^{\gamma} \left[\mu_{\text{C}}^{\gamma} - \mu_{\text{C}}^{\alpha}\right] + (1 - x_{\text{C}}^{\gamma}) \left[\mu_{\text{Z}}^{\gamma} - \mu_{\text{Z}}^{\alpha}\right] \tag{4.5}$$

Under the paraequilibrium treatment, the carbon redistribution is assumed to be instantaneous such that the carbon composition at the interface of the parent and product phase satisfies Equation 4.6Driving Force at the interface with respect of paraequilibriumequation.4.2.6 (i.e. null difference in the chemical potential of carbon across the interface).

$$\mu_{\text{C}}^{\alpha} = \mu_{\text{C}}^{\gamma} \tag{4.6}$$

Combining equations 4.5Driving Force at the interface with respect of paraequilibriumequation.4.2.5 and 4.6Driving Force at the interface with respect of paraequilibriumequation.4.2.6, the driving force can be expressed as

$$\Delta G^{\text{chem}} = (1 - x_{\text{C}}^{\gamma}) \ [\mu_{\text{Z}}^{\gamma} - \mu_{\text{Z}}^{\alpha}] \tag{4.7}$$

Then, for any transformed fraction, the driving pressure for transformation can be evaluated from the local chemistry at the boundary by Equation 4.7Driving Force at the interface with respect of paraequilibriumequation.4.2.7.

The molar Gibbs free energy diagram in Figure 4.1Equilibrium Z-C binary diagram illustrating the calculation of ΔG^{chem} figure.caption.44 shows the schematics of the calculation. For a given temperature, if the transformed fraction (f_1) is below that required by the paraequilibrium condition, the interface composition is still unequivocally defined by the tangent lines to the energy curves that satisfy the lever rule, Equation 4.8Driving Force at the interface with respect of paraequilibriumequation.4.2.8, and the condition from Equation 4.6Driving Force at the interface with respect of paraequilibriumequation.4.2.6.

$$f_1^{\alpha} = \frac{x_{\text{f1}}^{\gamma} - x_0}{x_{\text{f1}}^{\gamma} - x_{\text{f1}}^{\alpha}} = 1 - f_1^{\gamma} \tag{4.8}$$

The driving force for transformation can then be graphically obtained from the distance of the tangents at the product phase composition. With sufficient time, the transformation will proceed such that the tangents are shifted until the common tangent is reached (i.e. equilibrium compositions are achieved in Z-C).

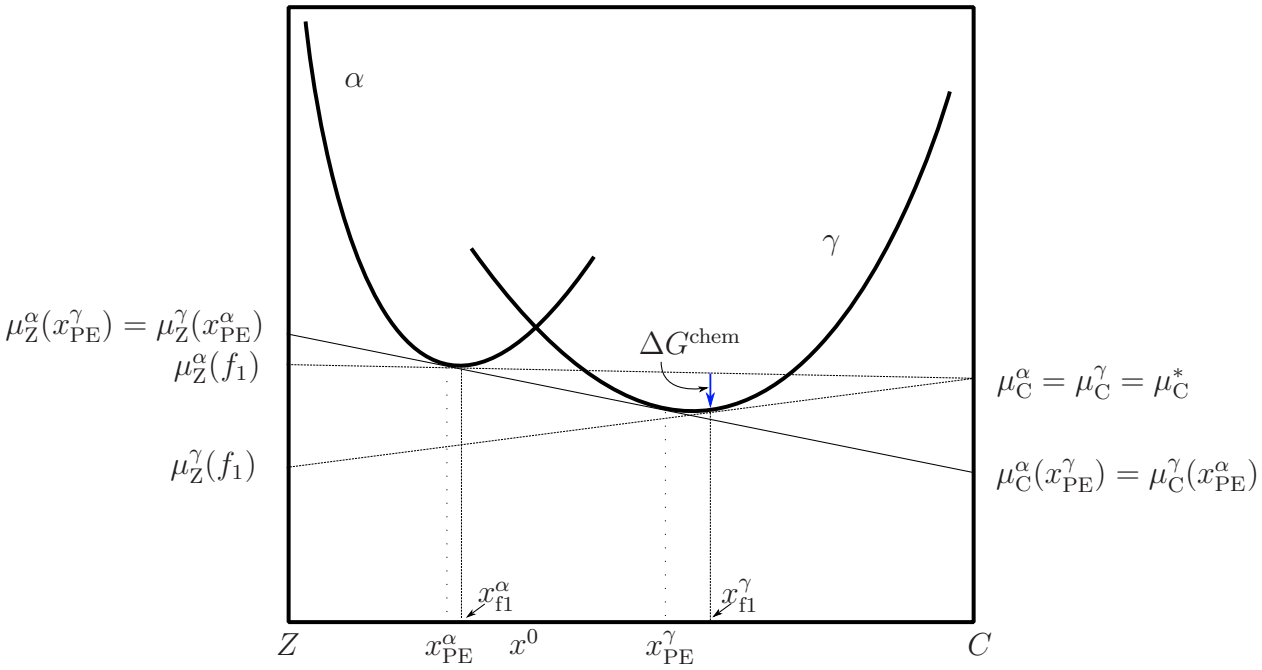

Figure 4.1: Equilibrium Z-C binary diagram illustrating the calculation of ΔG^{chem}

4.3 Calculation Procedure to obtain the Chemical Driving Force

According to Equation 4.7Driving Force at the interface with respect of paraequilibriumequation.4.2.7, to calculate the chemical driving force at a given temperature, it is necessary to determine the interface composition of austenite and ferrite to later calculate the difference in chemical potentials of Z in both phases. The steps of the methodology, are illustrated in Figure 4.2Process flow to calculate the chemical driving forcefigure.caption.45, are based on a geometric construction from the values of the Gibbs free energy of each phase at the bulk composition. The procedure involves the determination of all the possible interface concentrations that ensures the continuity of the chemical potential of C across the interface to later define the unique set of compositions that also satisfies the transformed fraction. Then, ΔG^{chem} is defined as a function of the temperature and transformation progress.

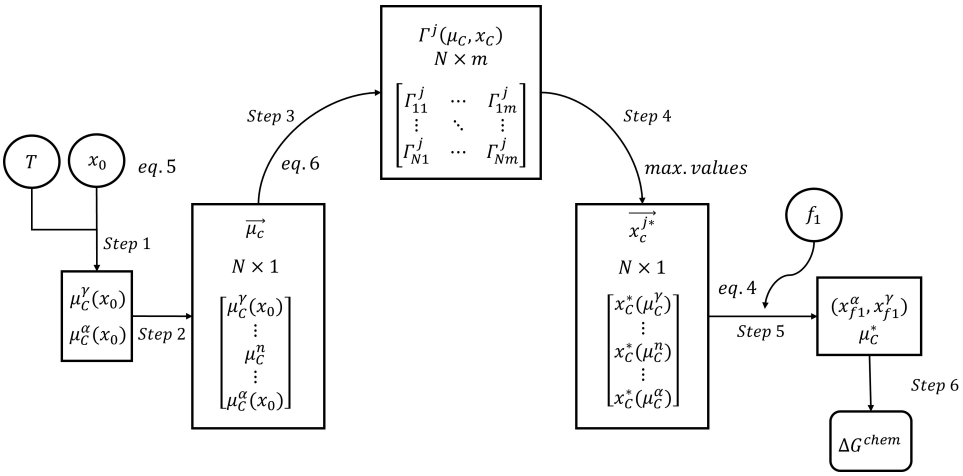

Figure 4.2: Process flow to calculate the chemical driving force

In the first step, the chemical potentials of carbon in both phases for $x = x_0$, are given by the intersection of the tangent curves t_A and t_F with $x_\mathrm{C} = 1$ in Figure 4.3Equilibrium Z-C binary diagram illustrating the calculation of ΔG^chem figure.caption.46, resulting in the following equation:

$$\mu^j_\mathrm{C} = G^j(x^0_\mathrm{C}) + (1 - x^0_\mathrm{C}) \left.\frac{\partial G^j}{\partial x}\right|_{x=x^0_\mathrm{C}} \tag{4.9}$$

where the value of $G^j(x_c, T)$ must be evaluated at the bulk carbon concentration and in its surroundings to calculate the tangent line. Each variable with the superscript j must be calculated for both phases, α and γ.

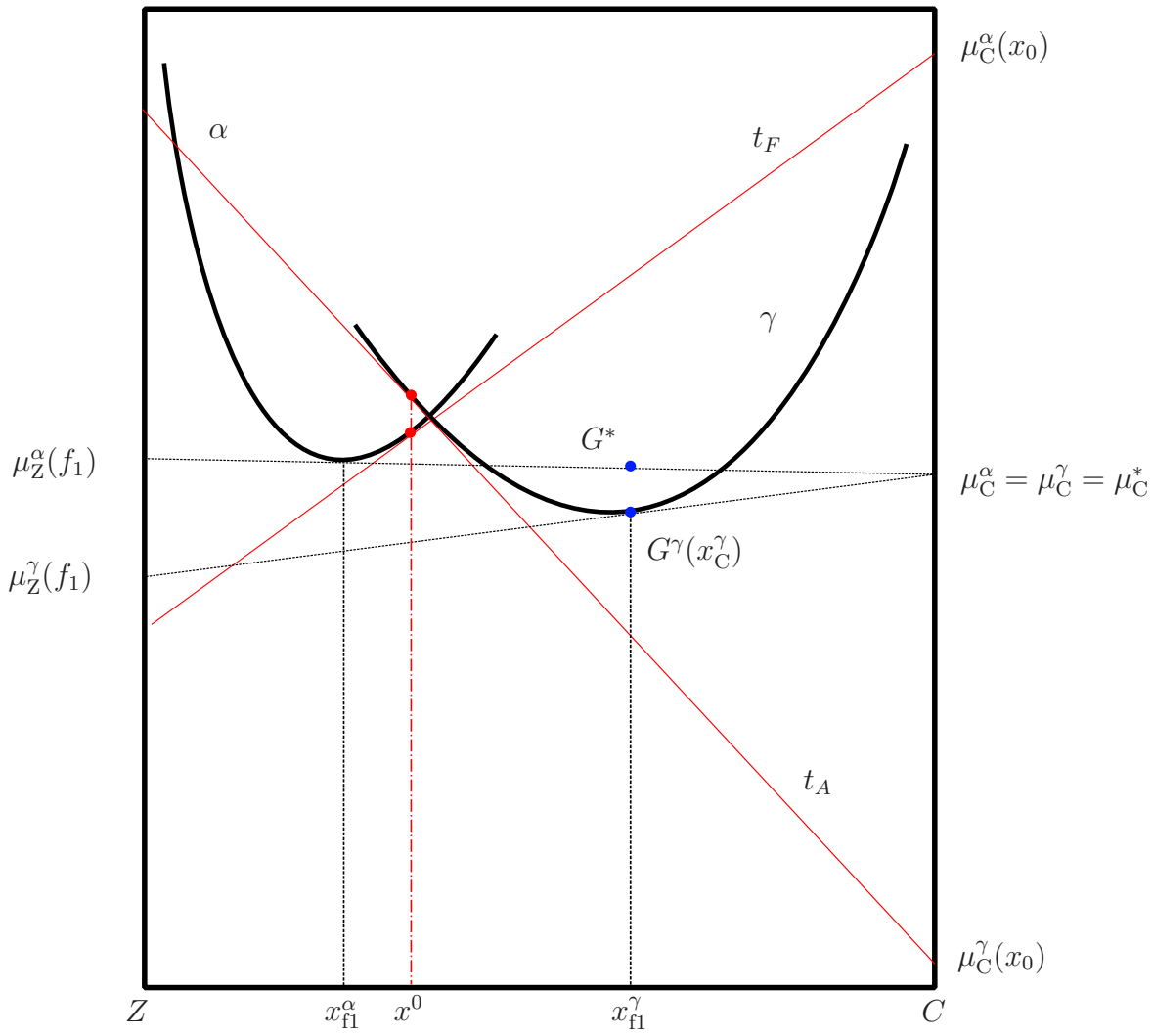

Figure 4.3: Equilibrium Z-C binary diagram illustrating the calculation of ΔG^{chem}

As is illustrated in Figure 4.3Equilibrium Z-C binary diagram illustrating the calculation of ΔG^{chem} figure.caption.46 the value of μ^*_{C} lies between the two calculated chemical potentials. In Step 2, the range $\mu^{\gamma}_{\text{C}}(x^0_{\text{C}})$ - $\mu^{\alpha}_{\text{C}}(x^0_{\text{C}})$ is divided in N equal intervals to obtain one array $\vec{\mu} = [\mu^{\gamma}_{\mathbf{C}}....\mu^{n-1}_{\mathbf{C}}\mu^{\alpha}_{\mathbf{C}}]$. The greater is the N number, the higher will be the accuracy at expense of calculation time. For the present work, a value of N=100 was found to be optimal.

In Step 3, each value of μ^n_{C} in equation 4.10Calculation Procedure to obtain the Chemical Driving Forceequation.4.3.10 is evaluated as a function of the carbon content for each phase. The operation results in two arrays (one for each phase) of size $N \times m$ where m represents the number of times that the Γ^j function was evaluated (i.e. the length of the carbon content array used in the numerical evaluation).

In Step 4, the values of x_{C} that yield the maximum value Γ^j for each element of $\vec{\mu}$ are stored to create two arrays $\vec{x}^j_{\mathbf{C}}$ which contain all the possible values of x^j_{C} such that the first constrain of Equation 4.6Driving Force at the interface with respect of paraequilibriumequation.4.2.6 is satisfied.

$$\Gamma^j(x_C) = \frac{\mu^n_{\text{C}} - G^j(x_C)}{1 - x_C} \tag{4.10}$$

Finally in Step 5, the elements of $\vec{x_{\mathbf{C}}^{j}}$ (the C content at the interfaces) that yield $f^{\gamma} = f_1$ and the associated value of $\vec{\mu}$ (the chemical potential of carbon for both phases) are employed to obtain the chemical Gibbs free energy combining the linear relationships presented in equations 4.11Calculation Procedure to obtain the Chemical Driving Forceequation.4.3.11 and 4.12Calculation Procedure to obtain the Chemical Driving Forceequation.4.3.12.

$$\Delta G^{\text{chem}} = G^{\gamma}(x_{\text{C}}^{\gamma}) - G^{*} \tag{4.11}$$

where

$$G^{*} = G^{\alpha}(x_{\text{C}}^{\alpha})\frac{1 - x_{\text{C}}^{\gamma}}{1 - x_{\text{C}}^{\alpha}} + \mu_{\text{C}}^{*}\ \frac{x_{\text{C}}^{\gamma} - x_{\text{C}}^{\alpha}}{1 - x_{\text{C}}^{\alpha}} \tag{4.12}$$

Equation 4.12Calculation Procedure to obtain the Chemical Driving Forceequation.4.3.12 enables the calculation of G^{*} for a given temperature, transformed fraction (f_1), and the nominal carbon content (x_0).

4.4 Case Study: Driving force for Austenite formation under paraequilibrium conditions in low microalloyed steels

This case study focuses on the formation of austenite in paraequilibrium conditions during continuous heating at two very different rates: 1 °C/s and 200 °C/s.

The steel used had the composition listed in Table 4.1Chemical composition of the X80 alloy studied (wt%).table.caption.47 and the dilatometry results are presented in Figure 4.4Austenite fraction as a function of the temperature for heating rates at 1 °C/s (red) and 200 °C/s (black).figure.caption.48. The dilatometry experiments were performed with a high-resolution quench L-78 RITA Linseis dilatometer and the transformation temperautres and fraction transformed were determined using the tangent line and lever rule methods respectively. Further information on the experimental setup is in chapter 2Effect of the heating rate on austenite formation in low carbon microalloyed steelschapter.2.

Table 4.1: Chemical composition of the X80 alloy studied (wt%).

C	**Mn**	**Si**	**Cr + Cu + Ni**	**Mo**	**Nb**	**V**	**Ti**	**Al**	**N**	**Fe**
0.03	1.7	0.27	0.45	0.297	0.091	0.002	0.017	0.044	0.0098	bal.

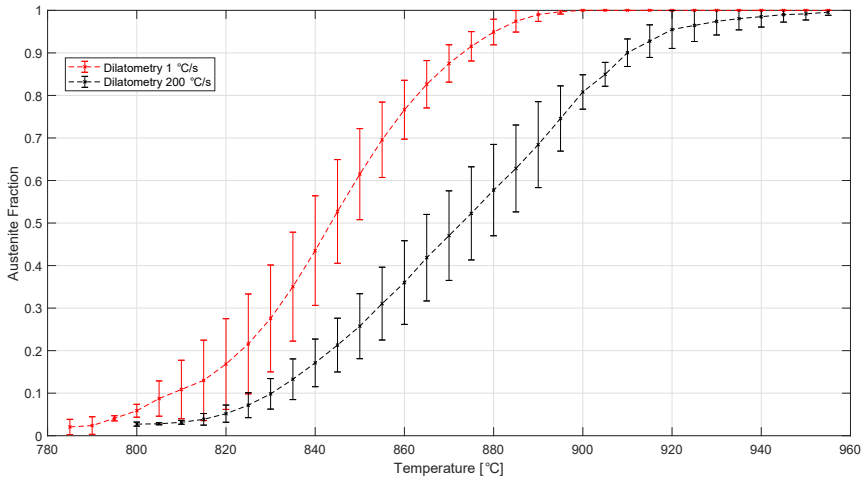

Figure 4.4: Austenite fraction as a function of the temperature for heating rates at 1 °C/s (red) and 200 °C/s (black).

The Gibbs free energy functions for α and γ were constructed using equations 4.1Thermodynamic properties of the Z-C systemequation.4.2.1 - 4.4Thermodynamic properties of the Z-C systemequation.4.2.4 (Section 4.2.2Thermodynamic properties of the Z-C systemsubsection.4.2.2) and equations C.1Gibbs Free Energy of Austeniteequation.C.0.1 - C.12Gibbs Free Energy of Austeniteequation.C.0.12 . The calculations where performed with a simplified chemical compositions of 0.02C-1.7Mn-0.29Si-0.27Mo, according to the considerations made in chapter 3Kinetics of austenization during heating accounting for solute drag and Mn redistributionchapter.3. The data base utilized to obtain the GES files of

the multicomponent system was SSOL4. The Matlab script containing the numerical calculation procedure can be found in Appendix CMatlab code for the calculation of the Gibbs free energy of ferrite and austenite in a Z-C systemappendix.C.

From the transformation - temperature curves for each experiments and Gibbs free energy functions, the chemical driving force was calculated at each temperature step using Equation 4.11Calculation Procedure to obtain the Chemical Driving Forceequation.4.3.11. Figure 4.5Calculated ΔG^{chem} for the heating of microalloyed steels at 1 °C/s and 200 °C/s.figure.caption.49 shows the values of ΔG^{chem} for both experiments.

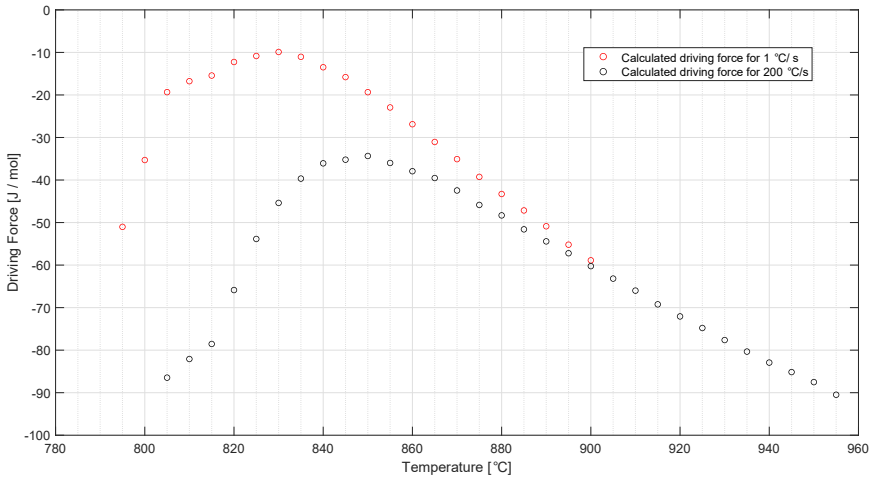

Figure 4.5: Calculated ΔG^{chem} for the heating of microalloyed steels at 1 °C/s and 200 °C/s.

The methodology presented was validated by comparing its predictions of austenite fraction under paraequilibrium conditions against a full thermodynamic calculation in paraequilibrium using ThermoCalc. The results are illustrated in Figure 5. For the proposed methodology, the volume fraction of autenite in paraequilibrium at each temperature, according to the binary Z-C construction, was obtained by finding the values of f_γ that yields $\Delta G^{\text{chem}} = 0$

.

Both calculations provide comparable results, with a maximum error of 5 °C at any austenite fraction, and the differences might be due to the usage of a different database or the slightly simplification of the chemical compositions.

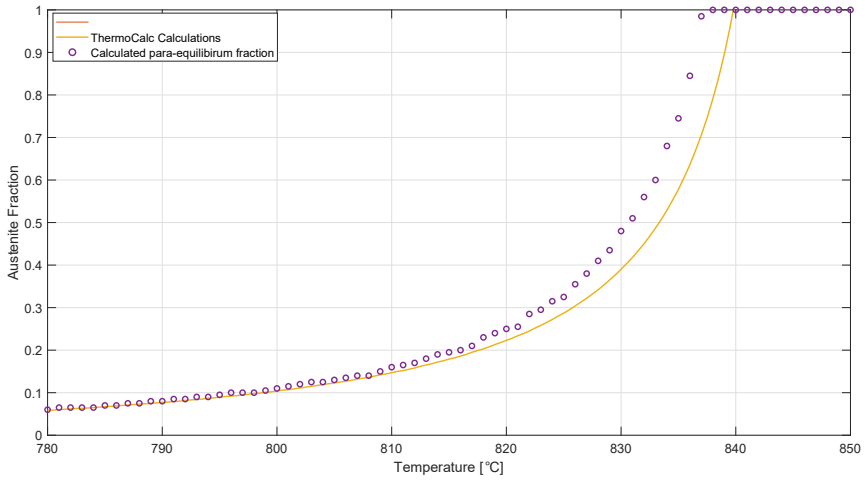

Figure 4.6: Austenite fraction under paraequilibrium conditions according to: (a) ThermoCalc calculations (TCFE10) and (b) the pseudo binary Z-C construction

4.5 Conclusion

A methodology for calculating the driving force during phase transformations in paraequilibrium is presented. It enables to transform rigorously a complex alloy such as a microalloyed steel into a much more treatable binary Z-C system.

The procedural steps are detailed in Figure 4.2Process flow to calculate the chemical driving forcefigure.caption.45, and the associated Equation 4.12Calculation Procedure to obtain the Chemical Driving Forceequation.4.3.12.

The methodology has been validated by calculating the austenization during heating of a microalloyed steel at 1 °C/s and 200 °C/s and comparing again paraequilibrium calculations in ThermoCalc, with a maximum error of 5 °C in predictions.

This methodology is the foundation for further predictions of the kinetics of austenization of steels, and it is, in principle, applicable to other alloy systems.

Chapter 5

Models to predict hardness in the HAZ

5.1 Abstract

The evolution and briefly description of the different empirical models to predict the hardness of the heat affected zone in low carbon steels are presented in this paper. Different approaches have been published during the 70's and 80's addressing different allloy composition and welding scenarios with great accuracy and simplicity. The models described rely on a statistical fitting of experimental data to obtain a empirical formula to predict the hardness as a function of the chemical composition and cooling rate (or usually as a function of the carbon equivalent and $t_{8/5}$).

5.2 Introduction

The toughness, hydrogen cracking susceptibility, stress corrosion cracking resistance, and feasibility (weldability) of a steel weld are strongly related to the hardness of the heat affected zone (HAZ). This hardness is determined by the steel composition and microstructure, and the microstructure is related to the thermal history of the weld. The microstructure of the HAZ typically involves a small set of microconstituents such as martensite, some form of bainite, and in some cases ferrite structures. This microstructure varies greatly within the HAZ, even though the nominal composition is the same.

Because of its importance, hardness of the HAZ is often limited by codes, standards, and good practice. The hardness associated with a welding procedure is typically anticipated only from experience, and in the lack of experience, from trial and error, at a considerable expense and time delay. For this reason, techniques were developed to predict this hardness from information known before performing the weld. The main approaches to predicting hardness in the HAZ include physical and mathematical models.

The physical modes aim to reproduce the welding thermal cycle in a laboratory often in a dilatometer. In addition to hardness, physical models often yield continuous cooling transformation (CCT) diagrams, for example those compiled in the exhaustive [120].However, due to the many different alloys and possible thermal cycles, it is common that the CCT needed for a particular procedure is absent, especially for newer alloys, such as those for pipelines.

The mathematical models aim to reproduce the effects of welding using calculations. Mathematical modes can be classified into two different types. The first type (" fundamental" approach) is based on fundamental equations of thermodynamics and kinetics of phase transformations [121–123]The second type of models ("fitting approach") attempts to capture the relationship between key variables and hardness by fitting formulae to large amounts of

experiments. Key variables include nominal alloy composition, cooling rate and in some cases the effects of the heating cycle. On the other hand, the experimental data can be also employed to develop a prediction system with a relatively new computational tool such as artificial neural networks [124–126]

The fitting approach is not as fundamental and general as the one based on thermodynamic and kinetics, but it is accurate enough in practice, and much easy to use by practitioners. This approach received considerable attention around the world in the 1970's and 1980's and enormous progress was accomplished. Somehow, after the 80's these models saw little use, although they were not replaced with a similar and practical approach. Nowadays many of the results of this research have been forgotten, and potential applications have suffered. The present paper will discuss this approach of empirical equations, their accuracy, their range of application and trade-offs.

5.3 Development of HAZ microstructure

During the thermal cycle of a welding process, most of the HAZ experiences austenitization and grain coarsening during heating, and austenite decomposition during cooling, resulting in various microstructures, depending on the prior austenite grain size, peak temperature, and cooling rate.

The transformations during cooling can be classified as (a) purely displacive (martensite) (b) purely reconstructive (ferrite and pearlite), and (c) combined displacive and reconstructive (e.g. acicular ferrite, widmanstatten ferrite, and others. In the models described all these transformations are grouped unde the label of "bainite").

5.4 Types of Fitting Models for HAZ hardness

The fitting approach models can be classified into two different groups. In the first group ("direct fitting"), the HAZ hardness is calculated directly from the composition and the cooling rate. In the second group ("indirect fitting"), the hardness is calculated from a predicted microstructure, and the microstructure is predicted from the nominal alloy composition and cooling rate. This second approach allows for the consideration of the effect of prior austenite grain size and different peak temperatures, in some cases leading to the prediction of hardness profiles, not just maximum value. For the case of "direct fitting", the hardness value is based on a interpolation of two characteristic values, a maximum hardness value (for a 100% martensite structure) and a minimum hardness value often related to a 100% "bainite" structure (i.e. 0 % martensite).

5.5 Direct Fitting Models

The direct fitting models rely on a statistical approach of a high quantity of experimental data to fit the gradual change of hardness of the HAZ as a function of the cooling rate (or $t_{8/5}$) and chemical composition, usually expressed by the carbon equivalent. The models assume that the martensite hardness is an upper limit given by the chemical composition of each steel. And on the other hand, the lower limit is given by the minimum hardness obtained from the experimental data, which coincides with a structure free of martensite. All the models address the prediction of the maximum hardness of the heat affected zone next to the fusion line since it is the point with the highest hardenability. Therefore, the lower limit is not necessarily related to the base material hardness but usually with a bainite (a mixed displacive-reconstructive) structure. Once the hardness of the two points are obtained (as a function of the chemical composition) a fitting function is proposed to define the final maximum hardness of the HAZ as a function of the cooling rate and chemical composition

5.5.1 Beckert, 1973

In 1973, Beckert was one first ones in relating the cooling rate and chemical composition to predict the maximum HAZ hardness [127]. The author developed a carbon-equivalent formula, CE_b, and estimated the hardness using the equation 5.2Beckert, 1973equation.5.5.2.

$$CE_b = \mathrm{C} + \frac{\mathrm{Mn}}{2.9} + \frac{\mathrm{Si}}{11} + \frac{\mathrm{Cr}}{3.2} + \frac{\mathrm{Cu}}{3.9} + \frac{\mathrm{Mo}}{3.4} + \frac{\mathrm{Ni}}{17} \tag{5.1}$$

$$HV = a \exp{(-bt)^2} + c \tag{5.2}$$

Where all the concentration are in weight percent, $t = t_{8/5}$ (in seconds) and a, b, and c are constants that depend on the chemical composition given by equations 5.3Beckert, 1973equation.5.5.3, 5.4Beckert, 1973equation.5.5.4, and 5.5Beckert, 1973equation.5.5.5. In Beckert's model, the constant $a+c$ is the maximum hardness when the structure is fully martensitic, while c refers to the minimum hardness of the microstructure.

$$a + c = 939\mathrm{C} + 284 \tag{5.3}$$

$$c = 167(CE_b)^{2.42} + 137 \tag{5.4}$$

$$b = \exp{(-0.013c + 0.8)} \tag{5.5}$$

In the original work, there is no specific range of chemical composition in which the model is consistent. However, it is mentioned that the equations address the family of low alloy carbon steels with a carbon content below 0.3 wt pct.

5.5.2 Arata, 1979

Later, in 1979, Arata et al. [128] proposed a two empirical formulas based on a "cooling rate function" and an "alloying element content function" to predict the hardness vs $t_{8/5}$ diagram, which the authors call as continuous cooling structure hardness (CCSH) diagram. The authors calculated characteristic values of the CCSH diagrams using regression data analysis of several CCT diagrams of different alloy steels. Arata assumed that these values depend only on the alloying elements and the influence of each element is linearly independent from each-other. As shown in Figure 5.1Relationship of the characteristic values A, B, and C in the CCSH diagram [128]figure.caption.51, the characteristics values A, B, and C are the corresponding values of hardness and $t_{8/5}$ associated to 100% martensite, 0% martensite, and intermediate point, f, respectively. Point A correspond to the coordinate $(\tau_{m100}, H_v(\tau_{m100}))$, B to $(\tau_{m0}, H_v(\tau_{m0}))$ and C to $(\tau_{mf}, H_v(\tau_{mf}))$. Later, the author assumed that for cooling times shorter than τ_{m100}, hardness has a constant value of $H_v(\tau_{m100})$ and that the change of hardness with $t_{8/5}$ between points A and B can be described with an inverse exponential function.

For the regression analysis the authors divided the study into two different types of steels, conventional welding steels (C-Si-Mn) and high strength (HT) Steels (the alloying elements such as Ni, Cr, V, Mo, B are considered) and gave expressions for points A, B, and C for each group. For example, equations for characteristics values A, B and C for C-Mn steels are presented

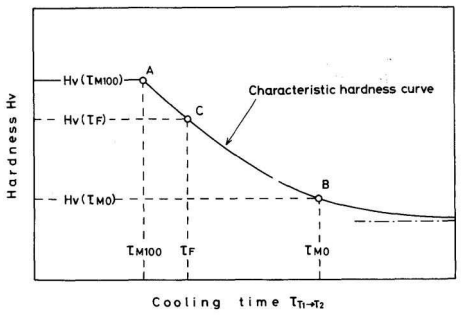

Figure 5.1: Relationship of the characteristic values A, B, and C in the CCSH diagram [128]

in equations 5.6Arata, 1979equation.5.5.6 - 5.11Arata, 1979equation.5.5.11.

$$\log \tau_{m100} = 2.55(\mathrm{C} + \frac{1}{6.3}\mathrm{Mn} + \frac{1}{3.6}\mathrm{Si}) - 0.92 \tag{5.6}$$

$$Hv(\tau_{m100}) = 835\mathrm{C} + 287 \tag{5.7}$$

$$\log \tau_{m0} = -0.37(\mathrm{C} - \frac{1}{1.1}\mathrm{Mn} - \frac{1}{0.44}\mathrm{Si}) + 1.02 \tag{5.8}$$

$$Hv(\tau_{m0}) = 237(\mathrm{C} + \frac{1}{13}\mathrm{Mn} + \frac{1}{9.7}\mathrm{Si}) + 133 \tag{5.9}$$

$$\log \tau_f = 5.77(\mathrm{C} + \frac{1}{17}\mathrm{Mn} + \frac{1}{14}\mathrm{Si}) - 0.88 \tag{5.10}$$

$$Hv(\tau_f) = -277(\mathrm{C} - \frac{1}{12}\mathrm{Mn} - \frac{1}{2.4}\mathrm{Si}) + 339 \tag{5.11}$$

The formulas of the characteristics values for HT Steels take into account the content of alloying elements as Ni, Cr, V, Mo, B and they can be founded in ref [128].

The two equations, α and β, that describe the CCHS diagrams in Arata's model are presented in equations 5.12Arata, 1979equation.5.5.12 and 5.13Arata, 1979equation.5.5.13 respectively. When the structure is fully martensitic, the equation 5.14Arata, 1979equation.5.5.14 is applicable for the two types of steel.

$$\tau > \tau_{m100} : H_v = \frac{b}{e^{\log(\tau)+a}} + 150(160) \tag{5.12}$$

$$\tau > \tau_{m100} : H_v = \frac{1}{e^{c' \log(\tau)+a'}} + 160(217) \tag{5.13}$$

$$\tau < \tau_{m100} : H_v = 835\mathrm{C} + 287 \tag{5.14}$$

Constants a', a, b, and c' are calculated fitting the equation to the characteristic values. The constant terms in equations 5.12Arata, 1979equation.5.5.12 and 5.13Arata, 1979equation.5.5.13, implies that when τ is large, hardness of conventional steels and (HT steels) have an asymptotic value given by the constant. The author mentions that formula β has higher accuracy to predict the hardness in the heat affected zone on high strength steels.

5.5.3 Terasaki 1979, 1984

Similar to Arata's model, Terasaki proposed simplified equations to predict the hardness of the HAZ as function of the carbon-equivalent and the cooling time [129, 130]. For cooling times, t, associated to a fully martensitic structure ($t < \tau_{m100}$) hardness is given by equation 5.15Terasaki 1979, 1984equation.5.5.15

$$HV_{max} = 812\mathrm{C} + 323 \tag{5.15}$$

Where τ_{m100} is related with the Terasaki's carbon-equivalent by equation 5.16Terasaki 1979, 1984equation.5.5.16

$$\log \tau_{m100} = 2.5 CE_T - 1.27 \tag{5.16}$$

And

$$CE_T = \mathrm{C} + \frac{\mathrm{Mn}}{3} + \frac{\mathrm{Cu}}{4} + \frac{\mathrm{Ni}}{8} + \frac{\mathrm{Cr}}{10} + \frac{\mathrm{Mo}}{3} + 5\mathrm{B} \tag{5.17}$$

When $t > \tau_{m100}$, hardness is given by equation 5.18Terasaki 1979, 1984equation.5.5.18

$$HV = HV_0 + (HV_0 - HV_{max}) \exp(-0.2(\frac{t}{\tau_{m100}} - 1)) \tag{5.18}$$

Where HV_0 is the hardness of the microstructure with 0 pct martensite, given by equation 5.19Terasaki 1979, 1984equation.5.5.19 and t is the $t_{8/5}$ in seconds.

$$HV_0 = 164(\mathrm{C} + \frac{\mathrm{Si}}{2} + \frac{\mathrm{Cr}}{7} + \frac{\mathrm{Mo}}{2} + \mathrm{V} + \mathrm{Nb} + 7\mathrm{B}) + 153 \tag{5.19}$$

5.5.4 Lorenz and Duren, 1981

In the early 1980's, in order to describe the new generation of High Strength steels, Lorenz and Duren developed a specific carbon-equivalent for pipeline steels (PSL). Using several welding tests results, Lorenz and Duren developed a formula to correlate the hardness of the HAZ with the $t_{8/5}$ for a given chemical composition. The PSL expression is presented in equation 5.20Lorenz and Duren, 1981equation.5.5.20

$$PSL = \mathrm{C} + \frac{\mathrm{Si}}{30} + \frac{\mathrm{Mn} + \mathrm{Cu}}{16} + \frac{\mathrm{Cr}}{20} + \frac{\mathrm{Ni}}{60} + \frac{\mathrm{Mo}}{40} + \frac{\mathrm{V}}{15} \tag{5.20}$$

To develop a equation for hardness vs cooling time, the authors divided the diagram in three different regions, as is shown in Figure 5.2Relationship between maximum hardness and cooling time for different microstructures [131].figure.caption.52. In the first region, when the structure is fully martensitic, the hardness in given by equation 5.21Lorenz and Duren, 1981equation.5.5.21.

$$HV_M = 802\mathrm{C} + 305 \tag{5.21}$$

For longer cooling times, the authors assumed that the microstructure is entirely bainitic and the hardness is given by equation 5.22Lorenz and Duren, 1981equation.5.5.22.

$$HV_B = 305\,CE_B + 101 \tag{5.22}$$

Where the term CE_B, given by equation 5.23Lorenz and Duren, 1981equation.5.5.23, refers to the carbon equivalent for a structure that consists only of bainite.

$$CE_B = \mathrm{C} + \frac{\mathrm{Si}}{11} + \frac{\mathrm{Mn}}{8} + \frac{\mathrm{Cu}}{9} + \frac{\mathrm{Cr}}{5} + \frac{\mathrm{Ni}}{17} + \frac{\mathrm{Mo}}{6} + \frac{\mathrm{V}}{3} \tag{5.23}$$

And for cooling times associated to a mixed structure of martensite and Bainite, the hardness is given by equation 5.24Lorenz and Duren, 1981equation.5.5.24

$$HV_x = 2019(\mathrm{C}[1 - 0.5\log t_{8/5}] + 0.3\,CE_B) + 66[1 - 0.8\log t_{8/5}] \tag{5.24}$$

Finally, the authors used equations 5.21Lorenz and Duren, 1981equation.5.5.21, 5.22Lorenz and Duren, 1981equation.5.5.22, and 5.24Lorenz and Duren, 1981equation.5.5.24 to propose a general expression for hardness as function of the cooling time, shown in equation 5.25Lorenz and Duren, 1981equation.5.5.25

$$HV = 802\mathrm{C} - (452\mathrm{C})A + 350A(CE_B - C) + 305(1 - 0.67A) \tag{5.25}$$

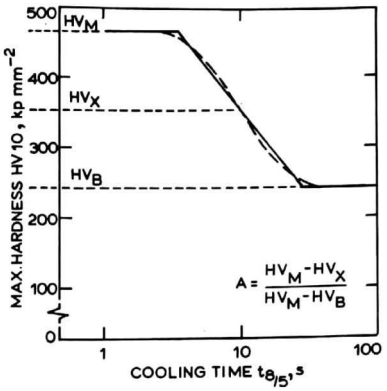

Figure 5.2: Relationship between maximum hardness and cooling time for different microstructures [131].

Where A, defined in equation 5.26Lorenz and Duren, 1981equation.5.5.26, takes into account the fraction of martenstite and bainite present in the microstructure for a given $t_{8/5}$, Figure 5.2Relationship between maximum hardness and cooling time for different microstructures [131].figure.caption.52.

$$A = \frac{HV_m - HV_x}{HV_m - HV_b} \tag{5.26}$$

5.5.5 Cotrell, 1984

In 1984, Cotrell [132] faced the challenge of developing a new hardness formula as a function of the cooling time and the chemical composition. The author started by correlating the boundary conditions of the hardness vs $t_{8/5}$ diagram with a physical metallurgy point of view using experimental data from different CCT diagrams. The formula presented by Cotrell proposes that the hardness as $t_{8/5} \to 0$ or $CE \to 1$ (i.e a fully martenstic structure)

should be given by equation 5.27Cotrell, 1984equation.5.5.27.

$$HV = 80 + 800(\mathrm{C} + 3N + 0.29) \tag{5.27}$$

In this equation, significant importance in given on the the effect of Nitrogen on the hardness of martensite.

When $t_{8/5}$ increases, Cotrell proposed that the equation 5.27Cotrell, 1984equation.5.5.27 should be multiplied by a correction factor that tends to 1 as CE increases or $t_{8/5}$ decreases and tends to 0 for lower CE or high $t_{8/5}$. To describe this behaviour, the author used an exponential function as a correcting factor shown in equation 5.28Cotrell, 1984equation.5.5.28.

$$HV = 80 + 800(\mathrm{C} + 3N + 0.29)e^{-(0.25r^K + \frac{\mathrm{Ni}}{\mathrm{Mn}^2})^{-1}} \tag{5.28}$$

$$K = 1.5[\mathrm{C} + \frac{\mathrm{Mn}}{6} + \frac{\mathrm{Cr}}{5} + + \frac{\mathrm{Mo}}{6} + \frac{\mathrm{V}}{3} + \frac{\mathrm{Nb}}{4C} + \frac{0.0001}{\mathrm{Si}}] \tag{5.29}$$

where r is the cooling rate (in °C / s) and K is an exponential factor of r that accounts for the effect of the alloying elements on hardenability. One of the unique aspects of this model is that the authors took into account using metallurgical principles the combined effect of alloying elements like Nb, Mn, and C.

5.5.6 Boothby, 1985

In 1985, Boothby presented a method to predict conditions for safe welding, in terms of hydrogen cracking (i.e HAZ hardness values) [133]. Firstly, the author established an empirical relationship between welding parameters (heat input, preheat temperature, and plate thickness) and cooling rate at 300 °C, shown in equation 5.30Boothby, 1985equation.5.5.30.

$$\frac{1}{\sqrt{R}} = \left[\frac{6.2\mathrm{C}}{T(1+0.001T)(0.335C+1.06)} + 0.044\right] + \left[\frac{1}{T(1+0.001T)(0.335C+1.06)} - 0.00001\right] E \tag{5.30}$$

Where R is the cooling rate at 300 °C (°C/s), E is the arc energy (J/mm), C is the combined plate thickness of joint (mm) and T is given by $T = 300 - P$, and P is the preheat temperature of the plate in °C.

Secondly, from the statistical treatment of several CCT diagrams Boothby related the cooling rate to achieve certain level of hardness in the HAZ with the carbon-equivalent formula. Finally using the deviation and dispersion of the first formulas and taking an upper bond limit, the author expressed the critical cooling rates to give a probability of 1 in 200 of exceeding 450, 400, 375, 350, and 325 HV by equations 5.31Boothby, 1985equation.5.5.31, 5.32Boothby, 1985equation.5.5.32, 5.33Boothby, 1985equation.5.5.33, 5.34Boothby, 1985equation.5.5.34, 5.35Boothby, 1985equation.5.5.35 respectively.

$$\frac{1}{\sqrt{Rc_{450}}} = 1.72(CE + 0.045) - 0.61 \tag{5.31}$$

$$\frac{1}{\sqrt{Rc_{400}}} = 1.93(CE + 0.045) - 0.63 \tag{5.32}$$

$$\frac{1}{\sqrt{Rc_{375}}} = 1.97(CE + 0.045) - 0.61 \tag{5.33}$$

$$\frac{1}{\sqrt{Rc_{350}}} = 1.72(CE + 0.045) - 0.59 \tag{5.34}$$

$$\frac{1}{\sqrt{Rc_{325}}} = 1.72(CE + 0.045) - 0.57 \tag{5.35}$$

Where the carbon-equivalent formula proposed by Boothby, given by 5.36Boothby, 1985equation.5.5.36, is a modification of the C_{eq}^{IIW} where the term $\frac{\mathrm{Si}}{6}$ is added to take into account the effect of Si on Si-killed steels.

$$CE = \mathrm{C} + \frac{\mathrm{Mn} + \mathrm{Si}}{6} + \frac{\mathrm{Cr} + \mathrm{Mo} + \mathrm{V}}{5} + \frac{\mathrm{Ni} + \mathrm{Cu}}{15} \tag{5.36}$$

Ultimately, to account for the effect of preheat temperature on the critical cooling rate of low alloy steels where transformation start temperatures (for certain hardness levels) might be higher than 300 °C , the following correction was suggested.

$$\frac{1}{\sqrt{R'}} = \frac{1}{\sqrt{R}} \frac{(300 - P)(T_s - 20)}{280(T_s - P)} \tag{5.37}$$

Where T_s is the transformation start temperature and P is the preheat temperature. An empirical correlation between $t_{8/5}$ and the cooling rate at 300 °C is presented at the end of Boothby's work.

5.5.7 Suzuki, 1982

Between 1982 and 1986, Suzuki proposed a new formula, named BL70, to estimate the HAZ maximum hardness [134]. The method, based on a backward regression, describes the maximum hardness (H_m) vs cooling rate with equation 5.38Suzuki, 1982equation.5.5.38.

$$H_m = H_{bm} + \frac{K}{1 + \exp a(Y - Y_5)} \tag{5.38}$$

Where $H_{bm} = 884\mathrm{C} + 287 - K$ is the hardness of the base metal, $Y = \log t_{8/5}$ ($t_{8/5}$ in seconds) and the constants K, Y_5, and aK are given by the following equations. The constants can be expressed as function of the carbon-equivalent formula, P_{cm}, developed by Bessyo in 1968 [135].

$$\begin{aligned} K = 269 + 454\mathrm{C} - 36\mathrm{Si} - 79\mathrm{Mn} - 57Cu \\ -12Ni - 53\mathrm{Cr} - 122Mo - 169Nb - 7089B \end{aligned} \tag{5.39}$$

$$\begin{aligned} Y_5 = -0.085 + 2.070\mathrm{C} + 0.459\mathrm{Mn} + 0.655\mathrm{Cu} \\ +0.122\mathrm{Ni} + 0.222\mathrm{Cr} + 0.788\mathrm{Mo} + 30\mathrm{B} \end{aligned} \tag{5.40}$$

$$aK = 478 + 3364\mathrm{C}256\mathrm{Si} + 66\mathrm{Ni} - 408\mathrm{Mo} - 1321\mathrm{V} - 1559\mathrm{Nb} \tag{5.41}$$

5.5.8 Yurioka, 1987

After several works, in 1987 the Nippon Steel company described the HV vs $t_{8/5}$ curve with the inverse of trigonometrical function. Similar to Arata's model, hardness prediction is based on a function (in this case an $arctan(x)$ function) that satisfies two characteristic values M and Z, shown in Figure 5.3Relationship between cooling time and hardness of the HAZ according to Yurioka's model [136]figure.caption.53.

Figure 5.3: Relationship between cooling time and hardness of the HAZ according to Yurioka's model [136]

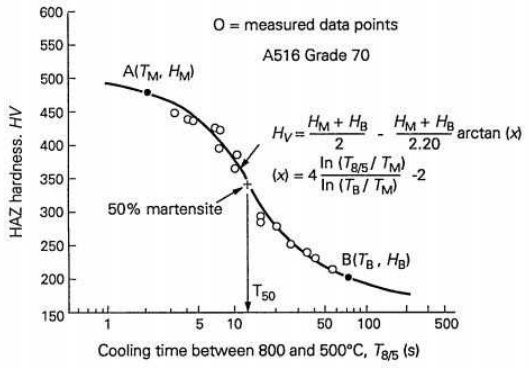

The point M is the critical point at which martensite volume fraction is 100 pct (value A in Arata's model), therefore the HAZ hardness value will be only function of the Carbon content of the steel. For times shorter than τ_m, martensite is the only phase present and the HV values should not drastically change. Point Z represents the point at which martensite is no longer present in the microstructure (i.e 0 pct, value B in Arata's model). Beyond this time value, hardness values will depend on the bainite

hardness. According to the authors, since these calculations are made for the portion of the HAZ that experimenced the highest austenization temperature (approximately $1400C$), hardenability is high due to the coarsened austenite grains, ferrite and pearlite phases are not consider for the cooling time range proposed for the HAZ. The four coordinates values (τ_m, τ_b, HV_m and HV_b) depend on the chemical composition and are defined from the analysis of experimental data by the following equations:

$$\tau_m = \exp 10.6\,CE_1 - 4.8 \tag{5.42}$$

$$\tau_b = \exp 6.2\,CE_3 - 0.74 \tag{5.43}$$

$$H_m = 884C(1 - 0.3\mathrm{C}^2) + 294 \tag{5.44}$$

$$H_b = 145 + 130 \tanh 2.65CE_3 - 0.69 \tag{5.45}$$

$$CE_1 = \mathrm{C}_p + \frac{\mathrm{Si}}{24} + \frac{\mathrm{Mn}}{6} + \frac{\mathrm{Cu}}{15} + \frac{\mathrm{Ni}}{12} + \frac{\mathrm{Mo}}{4} + \frac{\mathrm{Cr}(1 - 0.16\sqrt{\mathrm{Cr}})}{8} + \Delta H \tag{5.46}$$

Where C_p is the effective carbon and adopts values of $\mathrm{C}_p = C$ when $\mathrm{C} < 0.3$ wt pct and $C_p = \frac{\mathrm{C}}{6} + 0.25$ when $\mathrm{C} > 0.3$ wt pct.

$$CE_2 = \mathrm{C} + \frac{\mathrm{Si}}{24} + \frac{\mathrm{Mn}}{5} + \frac{\mathrm{Cu}}{10} + \frac{\mathrm{Ni}}{18} + \frac{\mathrm{Mo}}{2.5} + \frac{\mathrm{Cr}}{5} + \frac{\mathrm{V}}{5} + \frac{\mathrm{Nb}}{3} \tag{5.47}$$

$$CE_3 = C_p + \frac{\mathrm{Mn}}{3.6} + \frac{\mathrm{Cu}}{20} + \frac{\mathrm{Ni}}{9} + \frac{\mathrm{Mo}}{4} + \frac{\mathrm{Cr}}{5} \tag{5.48}$$

The authors considered the effect of boron on hardenability by introducing a correction factor ΔH into the carbon-equivalent I equation. The factor, takes the following values:

When $B < 1ppm$

$$\Delta H = 0 \tag{5.49}$$

when $B = 2ppm$

$$\Delta H = 0.03 f_n \tag{5.50}$$

when $B = 3ppm$

$$\Delta H = 0.06 f_n \tag{5.51}$$

And finally when $B > 4ppm$

$$\Delta H = 0.09 f_n \tag{5.52}$$

Where $f_n = \frac{0.02-N}{0.02}$ represents the tendency of Nitrogen to reduce the effect of Boron on hardenability. Once these values are obtained the maximum hardness of the HAZ as function of the cooling time $t_{8/5}$ is calculated, according to this model, by equation 5.53Yurioka, 1987equation.5.5.53.

$$HV = \frac{H_m + H_b}{2} - \frac{H_m - H_b}{2.2} \arctan x \tag{5.53}$$

where x is given by equation 5.54Yurioka, 1987equation.5.5.54

$$x(rad) = 4\frac{\log \frac{t_{8/5}}{t_m}}{\log \frac{t_b}{t_m}} - 2 \tag{5.54}$$

5.5.9 Abson, 2008

More recently, in 2008, Abson et al. [137] proposed a hybrid method combining Loren and Duren [131] and Yurioka's [138] models to predict the hardness of the heat affected zone in C-M and low alloy steels. Using over 300 data points, different methods for predicting the HAZ hardness were compared with experimental data. The hybrid method developed by Abson presented much better correlation with experimental data (compared with Yurioka, Lorenz, Terasaki, and Suzuki models) and a standard deviation of 28 HV.

The model it self, is a combinations between to former empirical models. Similar as other models (Arata, Yurioka, Suzuki, etc.), the equations for hardness were divided in three cases depending on the microstructure of the heat affected zone. When $t_{8/5} < \tau_m$, the structure is fully martensitic and hardness is given by equation 5.55Abson, 2008equation.5.5.55.

$$\begin{aligned} HV_m =& 0.5(802\mathrm{C} + 305 + 406\mathrm{C} + 164\,CE_I + 183 \\ & - (369\mathrm{C} - 149\,CE_I + 100)\arctan\frac{\log\tau_m - 2.822\,CE_{II} + 0.262}{0.526 - 0.19\,CE_{II}}) \end{aligned} \tag{5.55}$$

where τ_m was calculated from Lorenz and Duren work and is given by equation 5.56Abson, 2008equation.5.5.56

$$\tau_m = 10^{(\frac{611.3C+605.7CE-239}{1009.5C+52.8})} \tag{5.56}$$

For longer cooling times, $t_{8/5} > \tau_b$, according to the authors the structure will be fully bainitic and the hardness will be given by equation 5.57Abson, 2008equation.5.5.57

$$\begin{aligned} HV_b =& 0.5(305\,CE_{eq} + 101 + 406C + 164\,CE_I + 183 - \\ & - (369C - 149CE_I + 100)\arctan\frac{\log t_{8/5} - 2.822\,CE_{II} + 0.262}{0.526 - 0.19CE_{II}}) \end{aligned} \tag{5.57}$$

where

$$\tau_b = 10^{(\frac{1413.3C+300.7CE-35}{1009.5C+52.8})} \tag{5.58}$$

Equation 5.57Abson, 2008equation.5.5.57 accounts for a decrease on hardness of the bainite with longer cooling times due to, according to the authors, grain growth. And for $\tau_b < t_{8/5} < \tau_m$, hardness is given by equation 5.59Abson, 2008equation.5.5.59

$$\begin{aligned} HV =& 0.5(2019[\mathrm{C}(1 - 0.5\log t_{8/5}) + 0.3(CE_{eq} - \mathrm{C})] + \\ & 66(1 - 0.8\log t_{8/5}) + 0.5(406C + 164CE_I + 183 - \\ & (369C - 149CE_I + 100)\arctan\frac{\log t_{8/5} - 2.822CE_{II} + 0.262}{0.526 - 0.19CE_{II}}) \end{aligned} \tag{5.59}$$

Where the carbon equivalent formulas are defined as:

$$CE_{eq} = \mathrm{C} + \frac{\mathrm{Si}}{11} + \frac{\mathrm{Mn}}{8} + \frac{\mathrm{Cu}}{9} + \frac{\mathrm{Ni}}{17} + \frac{\mathrm{Cr}}{5} + \frac{\mathrm{Mo}}{6} + \frac{\mathrm{V}}{3} \tag{5.60}$$

$$CE_I = \mathrm{C} + \frac{\mathrm{Si}}{24} + \frac{\mathrm{Mn}}{6} + \frac{\mathrm{Cu}}{15} + \frac{\mathrm{Ni}}{40} + \frac{\mathrm{Cr}}{6} + \frac{\mathrm{Mo}}{4} + \frac{\mathrm{V}}{5} + \frac{\mathrm{Nb}}{5} + 10\mathrm{B} \tag{5.61}$$

$$CE_{II} = \mathrm{C} - \frac{\mathrm{Si}}{30} + \frac{\mathrm{Mn}}{5} + \frac{\mathrm{Cu}}{5} + \frac{\mathrm{Ni}}{20} + \frac{\mathrm{Cr}}{4} + \frac{\mathrm{Mo}}{6} + 10\mathrm{B} \tag{5.62}$$

5.6 Indirect Fitting Models

The following two models presented in this section split the challenge of predicting the hardness into two different steps. The final hardness of any point of the HAZ is calculated using the rules of mixtures.In which the hardness of each microconstituent is calculated as a function of the chemical composition and cooling. On the other hand, the type and volume fraction of each microconstituent is calculated separately and it also depend on the al-

loying composition and thermal cycle. Separating the problematic into two independent steps allows the user to use any model to predict the volume fraction of the microcontituents. Moreover, Anelli et al [125] trained an Artificial Neural Network to predict the amount of microstructural constituents after quenching. Later, to predict the final hardness the empirical model for microstructure hardness was employed [139].

5.6.1 Maynier, 1977

In 1978, the Le Creusot laboratory presented a set of empirical equations to predict the influence of alloying elements on the hardness and mechanical properties after a heat treatment. The work published involved a prediction of the microstructure [140] and a correlation of empirical formulas for the mechanical properties of the basic structures (martensite, bainite, and ferrite + pearlite) to predict the value of the mechanical properties using an additive rule [139]. Although the work presented in these papers is originally addressed to heat treatments, the results obtained by the Le Creusot model can be applied to typical welding thermal cycles.

In order to predict the microstructure after a heat treatment, the authors developed formulas for the critical cooling rates at which the resulting microstructure consists in different proportions of the basic phases (martensite, bainite, and ferrite + pearlite). In Figure 5.4Different critical cooling rates related to the percent of transformation [139]figure.caption.54 a schematic illustration of the critical cooling rates is shown.

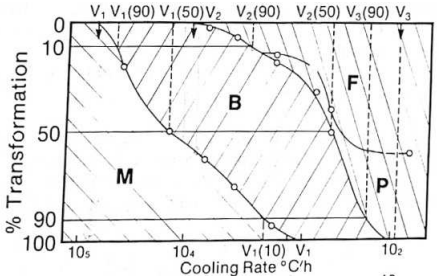

Figure 5.4: Different critical cooling rates related to the percent of transformation [139]

To develop the critical cooling rates formulas, the authors studied data from hundred of CCT diagrams from 8 different sources. The expression of critical cooling rates were obtained by correlating the experimental data of the first group of CCT diagrams and the chemical composition using the least squares method. Then calculations were compared with interpolated data of the second group of CCT diagrams. Importantly, the authors did not include the influence of impurities, such as S, P, Sn, and As, in their calculations since, according to authors, they are present in sufficiently small quantities and have a minor effect on hardenability.

Austenitization conditions were accounted for by the calculation of a parameter, P_a, which establish an equivalence between the time and the temperature of austenitization with the austenite grain growth. The authors presented an expression for each critical cooling rate with the following structure:

$$log(Vr) = constant + \sum K_i P_i + K P_a \tag{5.63}$$

Table 5.1: Alloying element factors for the calculation of critical cooling rates [139]

	cte	C	Mn	Ni	Cr	Mo	Pa
$logV_1$	9.81	4.62	1.10	0.54	0.50	0.66	0.0018
$logV_1^{90}$	8.76	4.04	0.96	0.49	0.58	0.97	0.0010
$logV_1^{50}$	8.50	4.13	0.86	0.57	0.41	0.94	0.0012
$logV_2$	10.17	3.80	1.07	0.70	0.57	1.58	0.0032
$logV_2^{90}$	10.55	3.65	1.08	0.77	0.61	1.49	0.0040
$logV_2^{50}$	8.74	2.23	0.86	0.56	0.59	1.60	0.0032
$logV_3^{90}$	7.51	1.38	0.35	0.93	0.11	2.31	0.0033
$logV_3$	6.36	0.43	0.49	0.78	0.26	0.38Mo + 2 Mo	0.0019

where K_i and P_i are the influence factor and weight percent of each alloying element, respectively. The values of each constant and factor to calculate the critical cooling rates reported by Maynier are shown in table 5.1Alloying element factors for the calculation of critical cooling rates [139]table.caption.55. The austenitization parameter, P_a, is given by:

$$P_a = \left(\frac{1}{T} - \frac{nR}{H} log(\frac{t}{t_o})\right)^{-1} \tag{5.64}$$

where T is temperature in Kelvin, n is the neperian logarithm of 10, R is the universal gas constant, H is activation energy (which in case of grain growth is of the order of 10 kcal/mole), t is time, and t_0 is unit of time (in hours).

The authors combined the critical cooling rate expression and empirical formulas to calculate the hardness of each phase as a function of the chemical composition and the cooling rate in order to obtain a hardness vs cooling rate diagram using the rule of mixture.

$$HV = V_m HV_m + V_b HV_b + V_{fp} HV_{fp} \tag{5.65}$$

Where V_i and HV_i are the volume fraction and hardness value of each constituent respectively.

Hardness formulas for martensite, bainite, and ferrite-pearlite structures shown in equations 5.66Maynier, 1977equation.5.6.66, 5.67Maynier, 1977equation.5.6.67, and 5.68Maynier, 1977equation.5.6.68 were obtained by a Blondeau et al [141] at the same laboratory, LeCreusot. The work done by Blondeau, in the same laboratory, is a first approach to Maynier's work.

$$HV_m = 127 + 949C + 27\text{Si} + 11\text{Mn} + 8\text{Ni} + 16\text{Cr} + 21 \log Vr \tag{5.66}$$

$$\begin{aligned} HV_b = &- 323 + 185C + 330\text{Si} + 153\text{Mn} + 65\text{Ni} + 144\text{Cr} + 191Mo \\ &+ (89 + 53C - 55\text{Si} - 22\text{Mn} - 10Ni - 20\text{Cr} - 33Mo) \log Vr \end{aligned} \tag{5.67}$$

$$\begin{aligned} HV_{f-p} = 42 + 223C + 53\text{Si} + 30\text{Mn} + 12.6Ni + 7\text{Cr} + 19Mo + \\ \log V_r(10 - 19\text{Si} + 4\text{Ni} + 8\text{Cr} + 130V) \end{aligned} \tag{5.68}$$

According to the authors, the cooling rate at 700 °C is equivalent to the cooling rate between 800 and 500 °C and can be easily changed to $t_{8/5}$ values to obtain similar diagrams than the ones designed for predict the HAZ hardness after welding. One of the distinctive characteristic of this model is that it was developed for a wider range of austenitization cycles, being able to predict hardness not only after a conventional heat treatment but also in the HAZ.

5.6.2 Ion, 1984

In 1984, Ion et al. [142] improved and extended a previous model developed by Ashby et al. [143] to predict the microstructure and hardness of the HAZ as a function of the carbon-equivalent. In these two works, the authors predicted the temperature profiles of a welding plate based on Rosenthal equations [144] and proposed empirical equations for the austenite grain growth, precipitate dissolution, coarsening and phase fraction transformed during cooling as function of the peak temperature, time, and cooling rate during welding processes. Later, using the additive rule and the equations for microstructure hardness developed by Blondeau et al. [141] (the same formulas as the Le Cresout model) Ion predicts the hardness HAZ as function of the $t_{8/5}$. The work and equations related to the austenite grain growth and precipitation coarsening and dissolution can be found in the cited reference. In the present work, the methodology to predict the HAZ hardness proposed by Ion is described. Similar as Maynier's work [139], the method to predict the HAZ is

based on two steps. First, calculate the phase fraction of each constituent of resulting microstructure after a given cooling rate. Second, knowing the hardness of each constituent, use the rule of mixture to give a hardness value. To predict the microstructure, the authors used Iganaki et al. [145] expression for a cooling time, Δt, associated to a microstructure containing 50/50 martensite and bainite, $\Delta t^m_{1/2}$, and 50/50 bainite and ferrile-pearlite, $\Delta t^b_{1/2}$, as a function of the carbon-equivalent equation recommended by the International Institute of Welding, equations 5.69Ion, 1984equation.5.6.69 and 5.70Ion, 1984equation.5.6.70. Correction factors for these time constants were proposed, equations 5.72Ion, 1984equation.5.6.72 and 5.73Ion, 1984equation.5.6.73, by the authors to consider the effect of grain growth during austenization on the hardenability.

$$\log \Delta t^m_{1/2} = 8.79 C^{IIW}_{eq} - 1.52 \tag{5.69}$$

$$\log \Delta t^b_{1/2} = 8.84 C^{IIW}_{eq} - 0.74 \tag{5.70}$$

where carbon equivalent is given by 5.71Ion, 1984equation.5.6.71

$$C^{IIW}_{eq} = \mathrm{C} + \frac{\mathrm{Mn}}{6} + \frac{\mathrm{Cr} + \mathrm{Mo} + \mathrm{V}}{5} + \frac{\mathrm{Cu} + \mathrm{Ni}}{15} \tag{5.71}$$

$$\Delta t^m_{1/2} = \frac{g}{g^o} (\Delta t^m_{1/2})^o \tag{5.72}$$

$$\Delta t^b_{1/2} = \frac{g}{g^o} (\Delta t^b_{1/2})^o \tag{5.73}$$

Where $(\Delta t_{1/2})^o$ is the transformation time for a given grain size g^o and $\Delta t_{1/2}$ is the corrected transformation.

The sigmoidal equations 5.74Ion, 1984equation.5.6.74 and 5.75Ion, 1984equation.5.6.75 were proposed to estimate the martensite and bainite fraction after a given cooling time. The ferrite-pearlite fraction are given by the volume fraction that did not transformed either in to martensite or bainite, equation 5.76Ion, 1984equation.5.6.76.

$$V_m = V_{max} \exp[-0.69(\frac{\Delta t}{\Delta t^m_{1/2}})^2] \tag{5.74}$$

$$V_b = V_{max} \exp[-0.69(\frac{\Delta t}{\Delta t^b_{1/2}})^2] - V_m \tag{5.75}$$

$$V_{fp} = 1 - (V_m + V_b) \tag{5.76}$$

Where V_m, V_b, and V_{fp} are the volume fraction of Martensite, Bainite, and Ferrite-Perlite structures respectively, Δt is the cooling time and $\Delta t_{1/2}$ and are the corrected constant times given by equation 5.72Ion, 1984equation.5.6.72 and 5.73Ion, 1984equation.5.6.73.,V_{max} is a factor that goes from 0 to 1 and accounts for the volume fraction of transformable austenite depending on the peak temperature. Finally, following the same procedure as Maynier's work, the authors calculated the maximum hardness of the heat affected zone using the rule of mixtures, equations 5.65Maynier, 1977equation.5.6.65, 5.66Maynier, 1977equation.5.6.66, 5.67Maynier, 1977equation.5.6.67, and 5.68Maynier,

1977equation.5.6.68. The inclusion of the V_{max} factor on equations 5.74Ion, 1984equation.5.6.74 and 5.75Ion, 1984equation.5.6.75 allows not only to predict the maximum hardness (when V_{max} is 1), but also the hardness profile of the HAZ (when $V_{max} < 1$).

5.7 Discussion

The models presented above were develop empirically during the 1970's and the 1980's around the world from different experimental data. However, the nature of the calculations is similar. Due to difficulties predicting the kinetics of austenite decomposition and hardnees of the different phases from fundamental physical metallurgical concepts, the statistical treatment and regression analysis of experimental data were the main tools to solve these models. Most models found the limit values of the problem (hardness of a pure martensitic and free martensitic structure) and later described the continuous change of hardness of the HAZ with cooling time with different types of functions.

Some of the models highlighted in the report explicitly state the applicable compositions in which the model can be used and other models have inferred applicable composition limits from the experimental data that was used. However, the applicable ranges were not able to be inferred for some of the models highlighted within this report, in those cases the alloyings elements

involved in the calculation have been pointed with a checkmark (✓) in Table 5.2Chemical composition ranges for models presented.table.caption.56. The models where the limits were clearly stated or inferred are also summarized in Table 5.2Chemical composition ranges for models presented.table.caption.56.

Beckert's work does not specify a range of chemical compositions, but it is mentioned that the model addresses low alloy steels with a carbon content below 0.3 pct wt.

On the other hand, Le Cresout, Cotrell, Yurioka, and Arata's model, present not only a defined range of chemical compositions, but also a detailed description of the model accuracy respect to experimental data.

Lorenz and Duren's model was specifically addressed to microalloyed steels. Although, the authors did not specified a range of composition, from the different steels used for the laboratory tests the inferred range is presented in Table 5.2Chemical composition ranges for models presented.table.caption.56. The authors run implant tests on steels with carbon contents of up to 0.5 wt pct. However, the majority of the tests involved low carbon steels with less than 0.3 pct wt. Evaluations of these tests were made in a wide range of $t_{8/5}$ from 2 - 40 seconds.

Suzuki's model was designed specifically for BL70 steels, which they represent a family of microalloyed steels with Boron. The composition range of the BL70 steels used by Suzuki is presented in Tabe 5.2Chemical composition ranges for models presented.table.caption.56.

Ion's model, uses Le Cresout model of hardness to estimate the HAZ hardness values. However, the authors compare their models with experimental data obtained from tests on Ti and Nb microalloyed steels.

Boothby, does not specify a chemical composition region. However, experimental data for the regression analysis was obtained from previous works on low alloy steels and C-Mn.

The composition range of the experimental data used by Abson's to develop the hybrid mode is presented in Table 5.2Chemical composition ranges for models presented.table.caption.56. The model addresses to a wide range of low alloy steels with a carbon content below 0.25 pct wt. Although the accuracy and the standard deviation informed by the authors is impressive compared to other models, the range of thickness and heat input of experimental data used covered values of $t_{8/5}$ of up to 6 seconds. This $t_{8/5}$ value can be very small for certain welding procedures with high heat inputs such as sumerged arc welding.

Martensite hardness, or maximum hardness, depends exclusively on the carbon for almost all models. Only Cotrell, which includes the Nitrogen effect, and Blondeu formulas (used by The Le Cresout and Ion's model) which accounts of several alloying elements and the cooling rate give an expression of martensite hardness as a function of multiple variables. However, influence of carbon in these formulas is significantly higher than the other elements or cooling rate. In regard to the effect of boron on hardenability, only Arata, Terasaki, Yurioka, and Suzuki's model account for it.

5.8 Summary

A brief description of the empirical models founded in literature to predict the HAZ hardness has been presented. Due to the nature of the models and how they were developed, differences between them and discrepancy compared to experimental data are expected. However, as a first approximation to estimate the HAZ hardness as function of the welding parameters (cooling time) the empirical models are useful. Unlike other mathematical approaches, these models use simple equations which do not need computational calculations. The user is responsible for selecting the appropriate models for each calculation (in terms of chemical composition and welding parameters) and although results have a good correlation with the experimental data, it is necessary critical interpretation of the results.

5.8.1 Acknowledgements

The authors acknowledge all the financial and support from the CWB Welding Foundation.

Table 5.2: Chemical composition ranges for models presented.

Model	C	Mn	Si	S	P	Cu	Ni	Cr	Mo	Nb	V	Ti	Al	N
Beckert	✓	✓	✓	-	-	✓	✓	✓	✓	-	-	-	-	-
Le Creusot	0.10 - 0.50	<2.00	<1.00	-	-	-	<4.00	<3.00	<1.00	-	<0.20	-	-	-
Arata	0.07 - 0.53	<1.50	<0.60	-	-	-	<3.50	<1.50	<0.60	-	<0.15	-	- -	-
Lorenz	0.03 - 0.55*	0.45 - 2.11	0.03 - 0.75	-	-	<0.60	<3.50	<0.33	<0.50	<0.04	<0.12	-	Al killed	-
Terasaki	✓	✓	✓	-	-	✓	✓	✓	✓	✓	✓	-	-	-
Cotrell	0.06 - 0.23	1.01 - 2.00	<0.55	<0.04	-	<0.30	<0.89	<0.20	<0.54	<0.05	<0.15	-	-	<0.05
Suzuki	0.017 - 0.33	0.4 - 2.00	<0.65	-	-	<0.47	<2.09	<1.06	<0.66	<0.06	<0.06	<0.02	-	-
Ion	✓	✓	✓	-	-	✓	✓	✓	✓	✓	✓	-	-	-
Yurioka	<0.8	<2	<1.2	<0.016	-	<0.9	<10	<10	<2	-	-	-	Al killed	✓
Abson	0.04 - 0.25	0.9 - 2.00	<0.50	<0.03	<0.04	<0.4	<0.90	<0.05	<0.6	<0.07	<0.15	<0.02	0.01 - 0.06	<0.015

Chapter 6

Conclusions

6.1 Conclusions and Summary of Findings

Two different commercial X80 pipeline steels were subject of study. Despite being the same material grade with similar chemical compositions, differences during the thermo mechanical processing of the materials lead to slightly different initial microstructures.

Despite the differences on the room temperautre microstructure, the results obtained in both chapters indicate that the early stages of transformation are sensitive to the heating rate and the initial microstructure. The metallographic observations of partially transformed samples suggests that at high heating rates, the M/A microconstituents or ferrite and carbide aggregates are favorable zones for austenite nucleation (if needed) and growth. And when the heating rate is decreased, ferrite grain boundaries and triple

points have been observed as nucleation sites of austenite. When the initial bainitic microsctructure contains features of an incomplete transformation phenomena, the transformation start temperature estimated was in good agreement with the determined ones by dilatometry.

One of the most remarkable results of this study is reflected in the continuous heating transformation diagram of Chapter 2Effect of the heating rate on austenite formation in low carbon microalloyed steelschapter.2 and the transformation times & temperatures of chapter 3Kinetics of austenization during heating accounting for solute drag and Mn redistributionchapter.3. The measured A_{c1} and A_{c3} for the re-austenization of pipeline steels during continuous heating presented higher values than the ones computed under orthoequilibrium conditions. A slightly dependence of these critical transformation temperatures with the heating rate was observed. A change of heating rates from 1 °C/s to 200 °C/s increased the start and finish transformation temperatures by approximately 20 °C and 50 °C respectively. Nevertheless, this results also indicate that time required for transformation to complete is reduced by 2 orders of magnitude when the heating rates is increased.

To understand this abrupt change in transformation kinetics, in Chapter 3Kinetics of austenization during heating accounting for solute drag and Mn redistributionchapter.3, a Gibbs free energy balance (GEB) was performed to model the boundary migration rate of austenite formation during con-

tinuous heating as a function of the chemical driving force. For the GEB approach, the energy dissipated by (a) the friction of the interface and (b) the solute drag effect of Mn was balanced with the available driving force for the transformation.

A original methodology, to calculate the chemical Gibbs free energy available for transformation under para-equilibrium conditions was proposed. With the guidelines of Chapter 4Driving force for phase transformation of microalloyed steels under paraequilibrium conditionschapter.4 and the additional information in Appendices AMatlab Code for the calculation of the chemical driving forceappendix.A, BDefinition of phase parameter for the Gibbs free energy calculationsappendix.B, and CMatlab code for the calculation of the Gibbs free energy of ferrite and austenite in a Z-C systemappendix.C, this procedure can be easily extended to analyze thermodynamic functions under paraequilbirum for different multicomponent systems.

Additionally, in Chapter 3Kinetics of austenization during heating accounting for solute drag and Mn redistributionchapter.3, a modification of the solute drag model was proposed to extend the model to account for the partially redistribution of the solute element between austenite and ferrite.

For the high heating rate experiments (200 °C/s) the model predicts a negligible interaction between the solute atoms and the moving interface, then the boundary migration is mainly controlled by the interface mobility and the driving force available for transformation.

For the slow heating rate experiments (1 °C/s), the Gibbs free energy balance, successfully predicts stagnant boundary migration rates when the volume fraction is close to the required by equilibrium and as the chemical driving force increases the interface velocity is given by the balance with the energy consumed by the diffusion of solute atoms within the interface.

Then, the difference in kinetics between the two different heating rates was elucidated by the fact that the available energy for transformation is consumed by different processes at the interface.

6.2 Future Work

- Due to the characteristics of the studied systems, the Gibbs free energy balance was performed accounting for the solute drag of only one substitutional alloying element, Mn. Future work, could focus on extending the solute drag model to account for other substitutional species.

- Combine the interface velocities calculated from the GEB approach with a suitable transformation model to obtain the transformed fraction as function of the time or temperature for any heating rate.

- The present work, was focused on reversion of austenite from a typical base metal microstructures of high strength pipeline steels. However, various current welding challenges are associated to the re-austenization of different initial microstructures. Thus, future investigation in this field should include the following topics:

  Explore the austenite formation from different HAZ initial microstructures. To mitigate the low toughness behavior of multipass welds, it is important to reduce the volume fraction and unfavorable distribution of M/A constituents at the ICHAZ. Thus, an understanding of austneite formation from a bainitic initial microstructure is imperative to understand the characteristics of the subsequent decomposition of the reverted austenite.

  Investigate the effect of the heating rate, chemical composition, and initial microstructure on the decomposition of the partially or scarcely complete transformed austenite. A thorough study will help to alleviate and prevent HAZ softening problematic in field girth weld.

  Study the influence of crystallographic texture during the austenite formation process. An investigation of the austenite nucleation and growth in relationship with the "austenite memory effect" could represent a crucial step to adjust Post Welding Heat Treatment conditions to improve the ERW bondline low temperature toughness in pipeline steels.

Bibliography

[1] Siebert, C. A., Breen, D. H., and Doane, D. V., 1977. *The hardenability of steels*. American Society for Metals.

[2] Puskar, J., Dykhuizen, R., Robino, C., Kelley, J., and Burnett, M., 2000. "Austenite formation kinetics during rapid heating in a microalloyed steel". *Iron & steelmaker,* ***27***(12), pp. 27–34.

[3] Gunabalapandian, K., Samanta, S., Ranjan, R., and Singh, S. B., 2017. "Investigation of Austenitization in Low Carbon Microalloyed Steel During Continuous Heating". *Metallurgical and Materials Transactions A: Physical Metallurgy and Materials Science,* ***48***(5), pp. 2099–2104.

[4] Caballero, F. G., Capdevila, C., and Andrés, C. G. D., 2001. "Mathematical Modeling of Iron and Steel Making Processes. Modelling of Kinetics of Austenite Formation in Steels with Different Initial Microstructures.". *ISIJ International,* ***41***(10), pp. 1093–1102.

[5] Caballero, F. G., Capdevila, C., and De Andrés, C. G., 2003. "An attempt to establish the variables that most directly influence the austenite formation process in steels". *ISIJ International,* ***43***(5), pp. 726–735.

[6] Macedo, M. Q., Cota, A. B., and Araujo, F. G. d. S., 2011. "The kinetics of austenite formation at high heating rates". *Rem: Revista Escola de Minas,* ***64***, 06, pp. 163 – 167.

[7] Dykhuizen, R. C., Robino, C. V., and Knorovsky, G. A., 1999. "A method for extracting phase change kinetics from dilatation for multistep transformations: Austenitization of a low carbon steel". *Metallurgical and Materials Transactions B,* ***30***(1), pp. 107–117.

[8] Kong, L., Liu, Y., Liu, J., Song, Y., Li, S., Liang, Y., Zheng, Y., and Cui, W., 2016. "Kinetics of the austenitization in the Fe-Mo-C ternary alloys during continuous heating". *Open Physics,* ***14***(1), pp. 695–702.

[9] Clarke, K. D., Van Tyne, C. J., Vigil, C. J., and Hackenberg, R. E., 2011. "Induction hardening 5150 steel: Effects of initial microstructure and heating rate". *Journal of Materials Engineering and Performance,* ***20***(2), pp. 161–168.

[10] Garcia, C. I., and Deardo, A. J., 1981. "Formation of austenite in 1.5 pct Mn Steels.". *Metallurgical transactions. A, Physical metallurgy and materials science,* ***12 A***(3), pp. 521–530.

[11] Martín, S. D., de T. Cock, García-Junceda, A., Caballero, F. G., Capdevila, C., and de Andrés, C. G., 2008. "Effect of heating rate on reaustenitisation of low carbon niobium microalloyed steel". *Materials Science and Technology,* ***24***(3), pp. 266–272.

[12] Reed, R., Akbay, T., Shen, Z., Robinson, J., and Root, J., 1998. "Determination of reaustenitisation kinetics in a Fe–0.4C steel using using dilatometry and neutron diffraction". *Materials Science and Engineering: A,* ***256***(1-2), pp. 152–165.

[13] Akbay, T., and Atkinson, C., 1996. "The influence of diffusion of carbon in ferrite as well as in austenite on a model of reaustenitization from ferrite/cementite mixtures in Fe-C steels". *Journal of Materials Science,* ***31***(9), pp. 2221–2226.

[14] Maicon, M., and Lopes, B., 2014. "Metallurgy and materials austenitization kinetics in a low". *Revista da Engenharia de Materiais - Metalurgia and Materiais,* ***67***(1), pp. 61–66.

[15] Moszner, F., Povoden-Karadeniz, E., Pogatscher, S., Uggowitzer, P. J., Estrin, Y., Gerstl, S. S., Kozeschnik, E., and Löffler, J. F., 2014. "Reverse alpha' to gamma transformation mechanisms of martensitic Fe-Mn and age-hardenable Fe-Mn-Pd alloys upon fast and slow continuous heating". *Acta Materialia,* ***72***, pp. 99–109.

[16] López-Martínez, E., Vázquez-Gómez, O., Vergara-Hernández, H. J., and Campillo, B., 2015. "Effect of initial microstructure on austenite formation kinetics in high-strength experimental microalloyed steels". *International Journal of Minerals, Metallurgy and Materials,* ***22***(12), pp. 1304–1312.

[17] Vasilyev, A. A., Kolbasnikov, N. G., Rudskoy, A. I., Sokolov, D. F., and Sokolov, S. F., 2017. "Kinetics of Structure Formation in the Heating of Cold-Rolled Automotive Steel Sheet". *Steel in Translation,* ***47***(12), pp. 830–838.

[18] Banerjee, K., Militzer, M., Perez, M., and Wang, X., 2010. "Non-isothermal austenite grain growth kinetics in a microalloyed x80 linepipe steel". *Metallurgical and Materials Transactions A: Physical Metallurgy and Materials Science,* ***41***(12), pp. 3161–3172.

[19] Speich, G. R., Demarest, V. A., and Miller, R. L., 1981. "Formation of Austenite During Intercritical Annealing of Dual-Phase Steels". *Metallurgical and Materials Transactions A,* ***12***(8), pp. 1419–1428.

[20] Souza, M. M., Guimarães, J. R., and Chawla, K. K., 1982. "Intercritical Austenitization of Two Fe-Mn-C Steels". *Metallurgical Transactions A,* ***13***(4), pp. 575–579.

[21] Huang, J., Poole, W. J., and Militzer, M., 2004. "Austenite formation during intercritical annealing". *Metallurgical and Materials Transactions A: Physical Metallurgy and Materials Science,* ***35A***(11), pp. 3363–3375.

[22] Kulakov, M., Poole, W. J., and Militzer, M., 2013. "The effect of the initial microstructure on recrystallization and austenite formation in a DP600 steel". *Metallurgical and Materials Transactions A: Physical Metallurgy and Materials Science,* ***44***(8), pp. 3564–3576.

[23] Mecozzi, M. G., Bos, C., and Sietsma, J., 2015. "A mixed-mode model for the ferrite-to-austenite transformation in a ferrite/pearlite microstructure". *Acta Materialia,* ***88***, pp. 302–313.

[24] Nehrenberg, A., 1950. "The growth of austenite as related to prior structure". *JOM,* ***2***(1), pp. 162–174.

[25] Azizi-Alizamini, H., Militzer, M., and Poole, W. J., 2011. "Austenite formation in plain low-carbon steels". *Metallurgical and Materials Transactions A: Physical Metallurgy and Materials Science,* ***42***(6), pp. 1544–1557.

[26] Law, N., and Edmonds, D., 1980. "The formation of austenite in a low-alloy steel". *Metallurgical and Materials Transactions A,* ***11***(1), pp. 33–46.

[27] Kimmins, S., and Gooch, D., 1983. "Austenite memory effect in 1 cr–1 mo–0· 75v (ti, b) steel". *Metal science,* ***17***(11), pp. 519–532.

[28] Matsuda, S., and Okamura, Y., 1974. "Microstructural and kinetic studies of reverse transformation in a low-carbon low alloy steel". *Transactions of the Iron and Steel Institute of Japan,* ***14***(5), pp. 363–368.

[29] Zhang, X., Miyamoto, G., Kaneshita, T., Yoshida, Y., Toji, Y., and Furuhara, T., 2018. "Growth mode of austenite during reversion from martensite in fe-2mn-1.5 si-0.3 c alloy: A transition in kinetics and morphology". *Acta Materialia,* ***154***, pp. 1–13.

[30] De Andres, C. G., Caballero, F. G., Capdevila, C., and Bhadeshia, H., 1998. "Modelling of kinetics and dilatometric behavior of non-isothermal pearlite-to-austenite transformation in an eutectoid steel". *Scripta Materialia,* ***39***(6), pp. 791–796.

[31] Shtansky, D., Nakai, K., and Ohmori, Y., 1999. "Pearlite to austenite transformation in an fe–2.6 cr–1c alloy". *Acta materialia,* ***47***(9), pp. 2619–2632.

[32] Datta, D. P., and Gokhale, A. M., 1981. "Austenization Kinetics of Pearlite and Ferrite Aggregates in Low Carbon Steel Containing 0. 15 wt pct C.". *Metallurgical transactions. A, Physical metallurgy and materials science,* ***12 A***(3), pp. 443–450.

[33] Li, Z.-D., Miyamoto, G., Yang, Z.-G., and Furuhara, T., 2009. "Nucleation of austenite from pearlitic structure in an fe–0.6 c–1cr alloy". *Scripta Materialia,* ***60***(7), pp. 485–488.

[34] Roosz, A., Gacsi, Z., and Fuchs, E., 1983. "Isothermal formation of austenite in eutectoid plain carbon steel". *Acta Metallurgica,* ***31***(4), pp. 509–517.

[35] Akbay, T., Reed, R. C., and Atkinson, C., 1994. "Modelling reaustenitisation from ferrite/cementite mixtures in FeC steels". *Acta Metallurgica Et Materialia,* ***42***(4), pp. 1469–1480.

[36] Jacot, A., Rappaz, M., and Reed, R. C., 1998. "Modelling of reaustenitization from the pearlite structure in steel". *Acta Materialia,* ***46***(11), pp. 3949–3962.

[37] Schmidt, E., Soltesz, D., Roberts, S., Bednar, A., and Sridhar, S., 2006. "The austenite/ferrite front migration rate during heating of IF steel". *ISIJ International,* ***46***(10), pp. 1500–1509.

[38] Yang, J., and Bhadeshia, H. "Reaustenitisation in steel weld deposits". *Proc. Int. Conf. on Recent Trends in Welding Science and Technology*, Vol. 9, pp. 549–63.

[39] Matsuda, S., and Okamura, Y., 1974. "The later stage of reverse transformation in low-carbon low alloy steel". *Transactions of the Iron and Steel Institute of Japan,* ***14***(6), pp. 444–449.

[40] Plichta, M., and Aaronson, H., 1974. "Influence of alloying elements upon the morphology of austenite formed from martensite in fe-cx alloys". *Metallurgical and Materials Transactions B,* ***5***(12), pp. 2611–2613.

[41] Cho, Y.-B., 2000. "The Kinetics of Austenite Formation during Continuous Heating of a Multi-Phase Steel". PhD thesis, University of British Columbia.

[42] Schmidt, E., Wang, Y., and Sridhar, S., 2006. "A study of nonisothermal austenite formation and decomposition in Fe-C-Mn alloys". *Metallurgical and Materials Transactions A: Physical Metallurgy and Materials Science,* ***37***(6), pp. 1799–1810.

[43] Atkinson, C., Akbay, T., and Reed, R. C., 1995. "Theory for reaustenitisation from ferrite/cementite mixtures in Fe-C-X steels". *Acta Metallurgica Et Materialia,* ***43***(5), pp. 2013–2031.

[44] Alvarenga, H. D., Van Steenberge, N., Sietsma, J., and Terryn, H., 2017. "The Kinetics of Formation and Decomposition of Austenite in Relation to Carbide Morphology". *Metallurgical and Materials Transactions A: Physical Metallurgy and Materials Science,* ***48***(2), pp. 828–840.

[45] Castro Cerda, F. M., Sabirov, I., Goulas, C., Sietsma, J., Monsalve, A., and Petrov, R. H., 2017. "Austenite formation in 0.2% C and 0.45% C steels under conventional and ultrafast heating". *Materials and Design,* ***116***, pp. 448–460.

[46] Schmidt, E. D., Damm, E., and Sridhar, S., 2007. "A study of diffusion- and interface-controlled migration of the austenite/ferrite front during austenitization of a case-hardenable alloy steel". *Metallurgical and Materials Transactions A,* ***38***(2), pp. 244–260.

[47] Rödel, J., and Spies, H.-J., 1996. "Modelling of austenite formation during rapid heating". *Surface Engineering,* ***12***(4), pp. 313–318.

[48] Enomoto, M., and Hayashi, K., 2015. "Simulation of the growth of austenite during continuous heating in low carbon iron alloys". *Journal of Materials Science,* ***50***(20), pp. 6786–6793.

[49] Li, B., Liu, Q., Jia, S., Ren, Y., and Yang, P., 2022. "Effect of v content and heat input on haz softening of deep-sea pipeline steel". *Materials,* ***15***(3), pp. 1996–1944.

[50] Mohammadijoo, M., Collins, L., Rashid, M., and Arafin, M., 2020. "Influence of steel chemistry and field girth welding procedure on performance of api x70 line pipe steels". *International Pipeline Conference*, Vol. 84461, American Society of Mechanical Engineers.

[51] Tronskar, J., and Vadholm, T. "Advances in linepipe material and welding". *Offshore Pipeline Technology Conference Asia 2015.*

[52] Khalaj, G., Pouraliakbar, H., Jandaghi, M. R., and Gholami, A., 2017. "Microalloyed steel welds by hf-erw technique: Novel pwht cycles, microstructure evolution and mechanical properties enhancement". *International Journal of Pressure Vessels and Piping,* ***152***, pp. 15–26.

[53] Yan, P., Güngör, Ö., Thibaux, P., Liebeherr, M., and Bhadeshia, H., 2011. "Tackling the toughness of steel pipes produced by high frequency induction welding and heat-treatment". *Materials Science and Engineering: A,* ***528***(29-30), pp. 8492–8499.

[54] Li, X., Shang, C., Ma, X., and Subramanian, S., 2014. "Study on the toughness of x100 pipeline steel heat affected zone". *Energy Materials 2014*. Springer, pp. 597–604.

[55] Esin, V., Denand, B., Le Bihan, Q., Dehmas, M., Teixeira, J., Geandier, G., Denis, S., Sourmail, T., and Aeby-Gautier, E., 2014. "In situ synchrotron X-ray diffraction and dilatometric study of austenite formation in a multi-component steel: Influence of initial microstructure and heating rate". *Acta Materialia,* ***80***, pp. 118 – 131.

[56] Caballero, F. G., Garcia-Mateo, C., and de Andres, C. G., 2005. "Dilatometric Study of Reaustenitisation of High Silicon Bainitic Steels: Decomposition of Retained Austenite". *Materials Transactions,* ***46***(3), pp. 581–586.

[57] Lopes, M. M. B., and Cota, A. B., 2014. "A study of isochronal austenitization kinetics in a low carbon steel". *Rem: Revista Escola de Minas,* ***67***, 03, pp. 61 – 66.

[58] Savran, V., Van Leeuwen, Y., Hanlon, D., Kwakernaak, C., Sloof, W., and Sietsma, J., 2007. "Microstructural features of austenite formation in C35 and C45 alloys". *Metallurgical and Materials Transactions A,* ***38***(5), pp. 946–955.

[59] Hernández-Morale, B., Vázquez-Gómez, O., López-Martínez, E., Vergara-Hernández, H., and Olmos, L., 2014. "Effect of heating rate and silicon content on kinetics of austenite formation during continuous heating". *Materials Science Forum*, Vol. 783, Trans Tech Publ, pp. 771–776.

[60] Papaefthymiou, S., Karamitros, V., and Bouzouni, M., 2019. "Ultrafast heating and initial microstructure effect on phase transformation evolution of a CrMo steel". *Metals,* ***9***(1), p. 72.

[61] Elmer, J., Palmer, T., Zhang, W., Wood, B., and DebRoy, T., 2003. "Kinetic modeling of phase transformations occurring in the HAZ of c-mn steel welds based on direct observations". *Acta Materialia,* ***51***(12), jul, pp. 3333–3349.

[62] Zhang, W., Elmer, J. W., and DebRoy, T., 2005. "Integrated modelling of thermal cycles, austenite formation, grain growth and decomposition in the heat affected zone of carbon steel". *Science and Technology of Welding and Joining,* ***10***(5), sep, pp. 574–582.

[63] Han, J., and Lee, Y. K., 2014. "The effects of the heating rate on the reverse transformation mechanism and the phase stability of reverted austenite in medium Mn steels". *Acta Materialia,* ***67***, pp. 354–361.

[64] Takahashi, M., 1992. "Reaustenitisation of Bainite". PhD thesis, University of Cambdridge.

[65] Yang, J. R., and Bhadeshia, H. K. D. H., 1991. "Continuous heating transformation of bainite to austenite". *Materials Science and Engineering A,* ***131***(1), pp. 99–113.

[66] Yang, J. R., and Bhadeshia, H. K. D. H., 1988. "The bainite to austenite transformation". *Phase Transformations,* ***87***, pp. 365–373.

[67] Cryderman, R., Garrett, D., Schlittenhart, Z., and Seo, E. J., 2020. "Effects of rapid induction heating on transformations in 0.6% c steels". *Journal of Materials Engineering and Performance,* ***29***(6), pp. 3502–3515.

[68] Chang, M., and Yu, H., 2013. "Kinetics of bainite-to-austenite transformation during continuous reheating in low carbon microalloyed steel". *International Journal of Minerals, Metallurgy and Materials,* ***20***(5), pp. 427–432.

[69] Wiskel, J. B., Li, X., Ivey, D. G., and Henein, H., 2018. "Characterization of X80 and X100 Microalloyed Pipeline Steel Using Quantitative X-ray Diffraction". *Metallurgical and Materials Transactions B: Process Metallurgy and Materials Processing Science,* ***49***(4), pp. 1597–1611.

[70] Collins, L. E., Wei, P., Nafisi, S., Wang, P., and Wiskel, J. B., 2016. "Effects of Segregation on the Mechanical Performance of X70 Line Pipe". Vol. Volume 3: Operations, Monitoring and Maintenance; Materials and Joining of *International Pipeline Conference*. V003T05A028.

[71] Faria, G., Cardoso, R., and Lino, J., 2017. "Efeito da composicao quimica sobre a cinetica de transformacao de fases de acos baixo carbono microligados laminados pelo processo steckel". pp. 222–235.

[72] Lima, A. P. d. S., Faria, G. L. d., Trindade Filho, V. B. d., and Candido, L. C., 2019. "Effect of the Chemical Homogeneity of a Quenched and Tempered C-Mn Steel Pipe on the Mechanical Properties and Phase Transformations". *Materials Research,* ***22***, 00.

[73] Kop, T. A., Sietsma, J., and Van Der Zwaag, S., 2001. "Dilatometric analysis of phase transformations in hypo-eutectoid steels". *Journal of Materials Science,* ***36***(2), pp. 519–526.

[74] Verma, A., Sundararaman, M., Singh, J., and Nalawade, S., 2010. "A new method for determining the curie temperature using a dilatometer". *Measurement Science and Technology,* ***21***(10), p. 105106.

[75] Lu, J., 2009. "Quantitative microstructural characterization of microalloyed steels". PhD thesis, University of Alberta.

[76] You Liu, Q., jun Sun, X., jun Jia, S., lin Zhang, L., jian Huang, G., and Ren, Y., 2009. "Austenitization Behaviors of X80 Pipeline Steel With High Nb and Trace Ti Treatment". *Journal of Iron and Steel Research International,* ***16***(6), pp. 58–62.

[77] Bhadeshia, H. K. D. H., and Christian, J., 1990. "Bainite in steels". *Metallurgical transactions A,* ***21***(3), pp. 767–797.

[78] Lobo, J. A., and Geiger, G. H., 1976. "Thermodynamics and solubility of carbon in ferrite and ferritic Fe-Mo alloys". *Metallurgical Transactions A,* ***7***(8), pp. 1347–1357.

[79] De Cooman, B. C., and Speer, J. G., 2011. *Fundamentals of steel product physical metallurgy.* AIST, Association for Iron & Steel Technology.

[80] Morales, E. V., Bott, I. S., Silva, R. A., Morales, A. M., and de Souza, L. F., 2016. "Characterization of Carbon-Rich Phases in a Complex Microstructure of a Commercial X80 Pipeline Steel". *Journal of Materials Engineering and Performance,* ***25***(7), pp. 2736–2745.

[81] Pawłowski, B., 2012. "Dilatometric examination of continuously heated austenite formation in hypoeutectoid steels". *Journal of Achievements in Materials and Manufacturing Engineering,* ***54***, 10, pp. 185–193.

[82] Takayama, N., Miyamoto, G., and Furuhara, T., 2018. "Chemistry and three-dimensional morphology of martensite-austenite constituent in the bainite structure of low-carbon low-alloy steels". *Acta Materialia,* ***145***, pp. 154 – 164.

[83] Lan, L., Qiu, C., Zhao, D., Gao, X., and Du, L., 2012. "Analysis of martensite-austenite constituent and its effect on toughness in submerged arc welded joint of low carbon bainitic steel". *Journal of Materials Science,* ***47***(11), pp. 4732–4742.

[84] Zong, Y., and Liu, C.-M., 2019. "Continuous Cooling Transformation Diagram, Microstructures, and Properties of the Simulated Coarse-Grain Heat-Affected Zone in a Low-Carbon Bainite E550 Steel". *Metals,* ***9***(9), p. 939.

[85] Savran, V. I., Offerman, S. E., and Sietsma, J., 2010. "Austenite nucleation and growth observed on the level of individual grains by three-dimensional X-ray diffraction microscopy". *Metallurgical and Materials Transactions A,* ***41***(3), pp. 583–591.

[86] Zener, C., 1949. "Theory of Growth of Spherical Precipitates from Solid Solution". *Journal of Applied Physics,* ***20***(10), pp. 950–953.

[87] Christian, J. W., 2002. *The Theory of Transformations in Metals and Alloys*. Pergamon, Oxford, Chap. Chapter 11 - Theory of Thermally Activated Growth, pp. 480 – 528.

[88] Bos, C., and Sietsma, J., 2007. "A mixed-mode model for partitioning phase transformations". *Scripta Materialia,* ***57***(12), dec, pp. 1085–1088.

[89] Sietsma, J., Mecozzi, M. G., van Bohemen, S. M. C., and van der Zwaag, S., 2006. "Evolution of the mixed-mode character of solid-state phase transformations in metals involving solute partitioning". *Zeitschrift für Metallkunde,* ***97***(4), apr, pp. 356–361.

[90] Sietsma, J., and van der Zwaag, S., 2004. "A concise model for mixed-mode phase transformations in the solid state". *Acta Materialia,* ***52***(14), aug, pp. 4143–4152.

[91] Chen, H., Zhu, K., Zhao, L., and van der Zwaag, S., 2013. "Analysis of transformation stasis during the isothermal bainitic ferrite formation in fe–c–mn and fe–c–mn–si alloys". *Acta materialia,* ***61***(14), pp. 5458–5468.

[92] Chen, H., Borgenstam, A., Odqvist, J., Zuazo, I., Goune, M., Ågren, J., and van der Zwaag, S., 2013. "Application of interrupted cooling experiments to study the mechanism of bainitic ferrite formation in steels". *Acta materialia,* ***61***(12), pp. 4512–4523.

[93] Clark, S. J., Lan, Y., Rahnama, A., Janik, V., and Sridhar, S., 2018. "A gibbs energy balance model for growth via diffusional growth-ledges". *ISIJ International*, pp. ISIJINT–2018.

[94] Fazeli, F., and Militzer, M., 2005. "Application of solute drag theory to model ferrite formation in multiphase steels". *Metallurgical and Materials Transactions A,* ***36***(6), pp. 1395–1405.

[95] Zhu, J., Luo, H., Yang, Z., Zhang, C., van der Zwaag, S., and Chen, H., 2017. "Determination of the intrinsic α/γ interface mobility during massive transformations in interstitial free Fe-X alloys". pp. 258–268.

[96] Enomoto, M., 1999. "Influence of solute drag on the growth of proeutectoid ferrite in fe–c–mn alloy". *Acta materialia,* ***47***(13), pp. 3533–3540.

[97] Fang, H., van der Zwaag, S., and van Dijk, N., 2021. "A novel 3d mixed-mode multigrain model with efficient implementation of solute drag applied to austenite-ferrite phase transformations in fe-c-mn alloys". *Acta Materialia,* ***212***, p. 116897.

[98] An, D., Pan, S., Ren, Q., Li, Q., Krakauer, B. W., and Zhu, M., 2020. "A gibbs energy balance model for the isothermal ferrite-to-austenite transformation". *Scripta Materialia,* ***178***, pp. 207–210.

[99] Cesaro, A. H., and Mendez, P., 2021. "Effect of the heating rate on austenite formation austenite formation during continuous heating on a grade x80 pipeline steel was studied". *WELDING JOURNAL,* ***100***(10), pp. 338S–347S.

[100] Kempen, A., Sommer, F., and Mittemeijer, E., 2002. "The kinetics of the austenite–ferrite phase transformation of fe-mn: differential thermal analysis during cooling". *Acta Materialia,* ***50***(14), aug, pp. 3545–3555.

[101] Austin, J., 1939. "Kinetics of the decomposition of austenite at constant temperature". *Transactions of the American Institute of Mining and Metallurgical Engineers,* ***135***, pp. 396–415.

[102] Cahn, J. W., 1962. "The impurity-drag effect in grain boundary motion". *Acta Metallurgica,* ***10***(9), sep, pp. 789–798.

[103] Lucke, K., and Stuwe, H., 1963. "Recovery and recrystallisation". *New York, Interscience,* ***9***, pp. 118–124.

[104] G.R. Purdy , Y.J.M. Brechet, 1995. "A solute drag treatment of the effects of alloying elements on the rate of the proeutectoid ferrite transformation in steels". *Acta Metallurgica et Materialia,* ***43***(10), oct, pp. 3763–3774.

[105] Hillert, M., Odqvist, J., and Ågren, J., 2001. "Comparison between solute drag and dissipation of gibbs energy by diffusion". *Scripta materialia,* ***45***(2), pp. 221–227.

[106] Hillert, M., 1999. "Solute drag, solute trapping and diffusional dissipation of gibbs energy". *Acta Materialia,* ***47***(18), dec, pp. 4481–4505.

[107] Grujicic, M., and Haidemenopoulos, G. N., 1988. "A treatment of paraequilibrium thermodynamics in AF1410 steel using the thermocalc software and database". *Calphad,* ***12***(3), jul, pp. 219–224.

[108] Krielaart, G. P., Sietsma, J., and Van Der Zwaag, S., 1997. "Ferrite formation in fe-c alloys during austenite decomposition under non-equilibrium interface conditions". *Materials Science and Engineering: A,* ***237***(2), pp. 216–223.

[109] Hillert, M., 1975. "Diffusion and interface control of reactions in alloys". *Metallurgical Transactions A,* ***6***(1), pp. 5–19.

[110] Gamsjäger, E., Wiessner, M., Schider, S., Chen, H., and van der Zwaag, S., 2015. "Analysis of the mobility of migrating austenite–ferrite interfaces". *Philosophical Magazine,* ***95***(26), sep, pp. 2899–2917.

[111] Wits, J., Kop, T., van Leeuwen, Y., Seitsma, J., and van Der Zwaag, S., 2000. "A study on the austenite-to-ferrite phase transformation in binary substitutional iron alloys". pp. 234–241.

[112] Kučera, J., and Stránskỳ, K., 1982. "Diffusion in iron, iron solid solutions and steels". *Materials Science and Engineering,* ***52***(1), pp. 1–38.

[113] Svoboda, J., Fischer, F. D., and Leindl, M., 2011. "Transient solute drag in migrating grain boundaries". *Acta materialia,* ***59***(17), pp. 6556–6562.

[114] Grujicic, M., and Haidemenopoulos, G. N., 1988. "A treatment of paraequilibrium thermodynamics in AF1410 steel using the thermocalc software and database". *Calphad,* ***12***(3), pp. 219–224.

[115] Ghosh, G., and Olson, G., 2001. "Simulation of paraequilibrium growth in multicomponent systems". *Metallurgical and Materials Transactions A,* ***32***(3), pp. 455–467.

[116] Ghosh, G., and Olson, G., 2002. "Precipitation of paraequilibrium cementite: Experiments, and thermodynamic and kinetic modeling". *Acta materialia,* ***50***(8), pp. 2099–2119.

[117] Sundman, B., and Ågren, J., 1981. "A regular solution model for phases with several components and sublattices, suitable for computer applications". *Journal of physics and chemistry of solids,* ***42***(4), pp. 297–301.

[118] Hillert, M., and Jarl, M., 1978. "A model for alloying in ferromagnetic metals". *Calphad,* ***2***(3), pp. 227–238.

[119] Gamsjäger, E., Antretter, T., Schmaranzer, C., Preis, W., Chimani, C. M., Simha, N. K., Svoboda, J., and Fischer, F. D., 2002. "Diffusional phase transformation and deformation in steels". *Computational materials science,* ***25***(1-2), pp. 92–99.

[120] Kasugai, T., 1999. "Atlas of cct diagrams for welding (i)". *NRIM-special report.*

[121] Buchmayr, B., and Kirkaldy, J., 1990. "Modeling of the temperature field, transformation behavior, hardness and mechanical response of low alloy steels during cooling from the austenite region". *Journal of Heat Treating,* ***8***(2), pp. 127–136.

[122] Li, M. V., Niebuhr, D. V., Meekisho, L. L., and Atteridge, D. G., 1998. "A computational model for the prediction of steel hardenability". *Metallurgical and Materials transactions B,* ***29***(3), pp. 661–672.

[123] Vandermeer, R., 1990. ""modeling diffusional growth during austenite decomposition to ferrite in polycrystalline fe c alloys"". *Acta Metallurgica et Materialia,* ***38***(12), pp. 2461 – 2470.

[124] Pouraliakbar, H., Khalaj, M.-J., Nazerfakhari, M., and Khalaj, G., 2015. "Artificial neural networks for hardness prediction of haz with chemical composition and tensile test of x70 pipeline steels". *Journal of Iron and Steel Research, International,* ***22***(5), pp. 446 – 450.

[125] Anelli, E., Cesile, M., and Di Nunzio, P., 2003. "Prediction of austenite decomposition during cooling of low and medium-carbon low-alloy steels". *Materials Science and Technology,* ***19***(5), pp. 453–466.

[126] Yu, L., Saida, K., Hirano, S., Chigusa, N., Mochizuki, M., and Nishimoto, K., 2017. "Application of neural network-based hardness prediction method to haz of a533b steel produced by laser temper bead welding". *Welding in the World,* ***61***(3), May, pp. 483–498.

[127] Beckert, B., and Holz, R., 1973. "Use of carbon equivalent and prediction of the weld heat affected zone hardness". *Schweiss Technik,* ***23***(8), pp. 344–350.

[128] Arata, Y., Nishiguchi, K., Ohji, T., and Kohsai, N., 1979. "Weldability concept on hardness prediction (materials, metallurgy, weldability)". *Transactions of JWRI,* ***8***(1), pp. 43–52.

[129] Terasaki, T., Akiyama, T., and Serino, M., 1984. "Chemical compositions and welding procedure to avoid cold cracking". *Proc. Int. Conf. Joining of Metals.*

[130] Terasaki, T., Karppi, R., and Satoh, K., 1979. "Relationship between critical stress of haz cracking and residual diffusible hydrogen content". *Transactions of the Japan Welding Society,* ***10***(1), pp. 53–57.

[131] Lorenz, K., and Duren, C., 1983. "Evaluation of large diameter pipe steel weldability by means of the carbon equivalent". *The Metals Society,*, pp. 322–332.

[132] Cottrell, C., 1984. "Hardness equivalent may lead to a more critical measure of weldability". *Met. Constr.,* ***16***(12), pp. 740–744.

[133] Boothby, P., 1985. "Predicting hardness in steel hazs". *Met. Constr.*, pp. 363 – 366.

[134] Suzuki, H., 1985. "A new formula for estimating haz maximum hardness in welded steel". *Transactions of the Japan Welding Society,* ***16***(2), pp. 157–164.

[135] Ito, Y., 1968. "Weldability formula for high strength steels related to heat affected zone cracking". *Journal of Japanese Welding Society,* ***12***, p. 938.

[136] Yurioka, N., Okumura, M., Kasuya, T., and Cotton, H., 1987. "Prediction of haz hardness of transformable steels". *Met. Constr.,* ***19***(4), p. 217.

[137] Nicholas, J., and Abson, D., 2008. "The prediction of maximum haz hardness in c-mn and low alloy steel arc welds". *17th International Conference Computer Technology in Welding Engineering. University of Cranfield, UK*, pp. 18–19.

[138] Yurioka, N., Ohshita, S., and Tamehiro, H., 1981. "Study on carbon equivalents to assess cold cracking tendency and hardness in steel welding in connection with the development of low carbon bainitic line-pipe steels". *Symposium on Pipeline welding in the 80s, 19-20 March 1981, Melbourne, Australia. Proc Australian Welding Research Association, lc-1 to lc*, Vol. 18.

[139] Maynier, P., Jungmann, B., and Dollet, J., 1977. "Creusot–loire system for the prediction of the mechanical properties of low alloy steel products". *Hardenability concepts with applications to steel*, pp. 518–545.

[140] Maynier, P., Dollet, J., and Bastien, P., 1978. "Prediction of microstructure via empirical formulas based on cct diagrams". *Metallurgical Society AIME,*, pp. 163–178.

[141] Blondeau, R., Maynier, P., Dollet, J., and Viellard-Baron, B., 1976. "Mathematical model for the calculation of mechanical properties of low alloy steel metallurgical products: A few examples of its applications". *Heat Treatment,* ***76***, pp. 6–7.

[142] Ion, J., Easterling, K. E., and Ashby, M., 1984. "A second report on diagrams of microstructure and hardness for heat-affected zones in welds". *Acta Metallurgica,* ***32***(11), pp. 19491957–19551962.

[143] Ashby, M., and Easterling, K. E., 1982. "A first report on diagrams for grain growth in welds". *Acta metallurgica,* ***30***(11), pp. 1969–1978.

[144] Rosenthal, D., 1946. "The theory of moving sources of heat and its application of metal treatments". *Transactions of ASME,* ***68***, pp. 849–866.

[145] M. Inagaki, H. S.", 1960.". *Trans. Natn. Res. Inst. Metals Japan,* ***2***, p. 102.

[146] Bergman, T. L., Lavine, A. S., Incropera, F. P., and DeWitt, D. P., 2011. *Introduction to heat transfer*. John Wiley & Sons.

Appendix A

Matlab Code for the calculation of the chemical driving force

Included in this Appendix is the Matlab code, according to the procedure detailed in chapter 4Driving force for phase transformation of microalloyed steels under paraequilibrium conditionschapter.4, section 4.3Calculation Procedure to obtain the Chemical Driving Forcesection.4.3, to calculate the chemical driving Force under para-equilbirum conditions.

```
{\small
function [DG,xxa,xxf]=DELTAG(T,VF)

%R constant [J/K mol]
R=8.314;

%Molar volume of austenite fron Ridley and Stuart1970 [m3/mol] also in
%"Control of Upstream Austenite Grain Coarsening during the Thin-Slab Cast
%Direct-Rolling"

VmA=7.3E-6;
```

```
%%%%%%%%%%%%%%%%%%
%%input nominal carbon content - .02 wt% (0.00093 mol fraction)
xn=0.00093;
%cabon content string [mol fraction] - geometric string

x=(9.119E-9)*1.03.^(0:545);


%derivative at xn of the Gibbs curves for each temperautre
[s_bcc_n,oi_bcc_n]=tangentBCC(xn,T);
[s_fcc_n,oi_fcc_n]=tangentFCC(xn,T);
%value of GF @ the xn and T.
gfn=GbccPE(xn,T);
%chemical potential of carbon in each phase @xn,T
UfnC=s_bcc_n*1 + oi_bcc_n;
UanC=s_fcc_n*1 + oi_fcc_n;

for i=1:length(x)
%evaluation of Giibs Energy of Austenite and Ferrite for x
GA(i)=GfccPE(x(i),T);
GF(i)=GbccPE(x(i),T);
%evuluation of the tangent to xn for each phase
tbcc_n(i)=s_bcc_n*x(i) + oi_bcc_n;
tfcc_n(i)=s_fcc_n*x(i) + oi_fcc_n;

end

%step division of chemical potential segmentation
n=100;
```

```
%difference between the chemical potential of carbon in austenite and ferrite

UcDIFF=abs(UfnC-UanC);

%step of chemical potential
int_u=UcDIFF/n;

%chemical potential string, from the lower mu_c to the higer mu_c
if UanC<UfnC

u=(UanC:int_u:UfnC);
else
u=(UfnC:int_u:UanC);
end

%Creating two matrices.
%One for austenite and one for ferrite with g_i values
for k=1:(n+1)

for i=1:length(x)
g_f(k,i)=  (u(k)-GF(i))/(1-x(i));
g_a(k,i)=  (u(k)-GA(i))/(1-x(i));

end

end

%find maxs of g_i, of each row (each mu_c) giving value "vi"(of g_i) and
%the index of x "ii". So ia and ife are the index value of x string that
```

```
%correspond to the maximum value of g_i when mu_c is given by the row
%number.
%
[va,ia]=max(g_a,[],2);
[vf,ife]=max(g_f,[],2);

%%with the x values that correspond to the maxium value of g_i, the
%phase fraction array for all each mu_c value is given by these functions.

f_a= (xn-x(ife))./(x(ia)-x(ife));
f_f=(x(ia)-xn)./(x(ia)-x(ife));

if f_a(1)>1
f_a(1)=1;
end
if f_f(1)<0
f_f(1)=0;
end

[val,ind]=min(abs(f_a-VF));

%sting of maximum values of g_i for the mu_c that correspond to the
%experimental transformed fraction
ga=g_a(ind,ia);
gf=g_f(ind,ife);

%p1 and p2 are the the index for the x string
%that gives you the maximum g_i with the corresponding mu_c
p1=ia(ind);
p2=ife(ind);
```

```
%save the x value for ferrite and austenite for o steps in temp.
xxa= x(p1);
xxf=x(p2);


%calculate tangents to xxa and xxf

[s_bcc2,oi_bcc2]=tangentBCC(x(p2),T);
[s_fcc2,oi_fcc2]=tangentFCC(x(p1),T);

for i=1:length(x)
tbcc_2(i)=s_bcc2*x(i) + oi_bcc2;
tfcc_2(i)=s_fcc2*x(i) + oi_fcc2;
end

UfnC2=s_bcc2*1 + oi_bcc2;
UanC2=s_fcc2*1 + oi_fcc2;

%%%%gibbs free energy according to the geometric construction.

A=1
%%%%Gibbs free energy for austenite
GAP1=GfccPE(x(p1),T);
G_ast=((1-x(p2))/(1-x(p1)))*GAP1 - A*u(ind)*((x(p1)-x(p2))/(1-x(p1)));
DG =  G_ast - GF(p2);
}
```

Appendix B

Definition of phase parameter for the Gibbs free energy calculations

The general form of each phase thermodynamic parameter utilized in the calculation of the molar Gibbs free energy of the system Z-C are presented below.

Each term, is defined by the combination of the site fraction, y, of substituional elements (p, o, l) and their respective reference value obtained from the thermodynamic data base.

$$G^{0,j}_{\mathrm{Z:C}} = \sum y_{\mathrm{p}} G^{0,j}_{\mathrm{p:C}} + RT \sum y_{\mathrm{p}} \ln y_{\mathrm{p}} + \sum \sum_{p \neq o} y_{\mathrm{p}} y_{\mathrm{o}} (L^{0,j}_{\mathrm{p:o:C}} + (y_{\mathrm{p}} - y_{\mathrm{o}}) L^{1,j}_{\mathrm{p:o:C}}) + \sum \sum \sum_{p \neq o \neq l} y_{\mathrm{p}} y_{\mathrm{o}} y_{\mathrm{l}} L^{0,j}_{\mathrm{p:o:l:C}} \quad \text{(B.1)}$$

$$G^{0,j}_{\mathrm{Z:VA}} = \sum y_{\mathrm{p}} G^{0,j}_{\mathrm{p:VA}} + RT \sum y_{\mathrm{p}} \ln y_{\mathrm{p}} + \sum \sum_{p \neq o} y_{\mathrm{p}} y_{\mathrm{o}} (L^{0,j}_{\mathrm{p:o:VA}} + (y_{\mathrm{p}} - y_{\mathrm{o}}) L^{1,j}_{\mathrm{p:o:VA}}) + \sum \sum \sum_{p \neq o \neq l} y_{\mathrm{p}} y_{\mathrm{o}} y_{\mathrm{l}} L^{0,j}_{\mathrm{p:o:l:VA}} \quad \text{(B.2)}$$

$$L^{0,j}_{\mathrm{Z:C:VA}} = \sum y_{\mathrm{p}} L^{0,j}_{\mathrm{p:C:VA}} + \sum \sum_{p \neq o} y_{\mathrm{p}} y_{\mathrm{o}} L^{0,j}_{\mathrm{p:o:C:VA}} \quad \text{(B.3)}$$

$$L^{1,j}_{\mathrm{Z:C:VA}} = \sum y_{\mathrm{p}} L^{1,j}_{\mathrm{p:C:VA}} + \sum \sum_{p \neq o} y_{\mathrm{p}} y_{\mathrm{o}} (y_{\mathrm{p}} - y_{\mathrm{o}}) L^{0,j}_{\mathrm{p:o:C:VA}} \quad \text{(B.4)}$$

$$\beta^{0,j}_{\mathrm{Z:C}} = \sum y_{\mathrm{p}} \beta^{0,j}_{\mathrm{p:C}} + \sum \sum_{p \neq o} y_{\mathrm{p}} y_{\mathrm{o}} (\beta^{0,j}_{\mathrm{p:o:C}} + (y_{\mathrm{p}} - y_{\mathrm{o}}) \beta^{1,j}_{\mathrm{p:o:C}}) + \sum \sum \sum_{p \neq o \neq l} y_{\mathrm{p}} y_{\mathrm{o}} y_{\mathrm{l}} \beta^{0,j}_{\mathrm{p:o:l:C}} \quad \text{(B.5)}$$

$$\beta^{0,j}_{\mathrm{Z:VA}} = \sum y_{\mathrm{p}} \beta^{0,j}_{\mathrm{p:VA}} + \sum \sum_{p \neq o} y_{\mathrm{p}} y_{\mathrm{o}} (\beta^{0,j}_{\mathrm{p:o:VA}} + (y_{\mathrm{p}} - y_{\mathrm{o}}) \beta^{1,j}_{\mathrm{p:o:VA}}) + \sum \sum \sum_{p \neq o \neq l} y_{\mathrm{p}} y_{\mathrm{o}} y_{\mathrm{l}} \beta^{0,j}_{\mathrm{p:o:l:VA}} \quad \text{(B.6)}$$

$$\beta^{0,j}_{\text{Z:C:VA}} = \sum y_{\text{p}} \beta^{0,j}_{\text{p:C:VA}} + \sum \sum_{p \neq o} y_{\text{p}} y_{\text{o}} \beta^{0,j}_{\text{p:o:C:VA}} \quad \text{(B.7)}$$

$$\beta^{1,j}_{\text{Z:C:VA}} = \sum y_{\text{p}} \beta^{1,j}_{\text{p:C:VA}} + \sum \sum_{p \neq o} y_{\text{p}} y_{\text{o}} (y_{\text{p}} - y_{\text{o}}) \beta^{1,j}_{\text{p:o:C:VA}} \quad \text{(B.8)}$$

$$\begin{aligned} Tc^{0,j}_{\text{Z:C}} = & \sum y_{\text{p}} Tc^{0,j}_{\text{p:C}} \\ & + \sum \sum_{p \neq o} y_{\text{p}} y_{\text{o}} (Tc^{0,j}_{\text{p:o:C}} + (y_{\text{p}} - y_{\text{o}}) Tc^{1,j}_{\text{p:o:C}}) \\ & + \sum \sum \sum_{p \neq o \neq l} y_{\text{p}} y_{\text{o}} y_{\text{l}} Tc^{0,j}_{\text{p:o:l:C}} \end{aligned} \quad \text{(B.9)}$$

$$\begin{aligned} Tc^{0,j}_{\text{Z:VA}} = & \sum y_{\text{p}} Tc^{0,j}_{\text{p:VA}} \\ & + \sum \sum_{p \neq o} y_{\text{p}} y_{\text{o}} (Tc^{0,j}_{\text{p:o:VA}} + (y_{\text{p}} - y_{\text{o}}) Tc^{1,j}_{\text{p:o:VA}}) \\ & + \sum \sum \sum_{p \neq o \neq l} y_{\text{p}} y_{\text{o}} y_{\text{l}} Tc^{0,j}_{\text{p:o:l:VA}} \end{aligned} \quad \text{(B.10)}$$

$$Tc^{0,j}_{\text{Z:C:VA}} = \sum y_{\text{p}} Tc^{0,j}_{\text{p:C:VA}} + \sum \sum_{p \neq o} y_{\text{p}} y_{\text{o}} Tc^{0,j}_{\text{p:o:C:VA}} \quad \text{(B.11)}$$

$$Tc^{1,j}_{\text{Z:C:VA}} = \sum y_{\text{p}} Tc^{1,j}_{\text{p:C:VA}} + \sum \sum_{p \neq o} y_{\text{p}} y_{\text{o}} (y_{\text{p}} - y_{\text{o}}) Tc^{1,j}_{\text{p:o:C:VA}} \quad \text{(B.12)}$$

Appendix C

Matlab code for the calculation of the Gibbs free energy of ferrite and austenite in a Z-C system

Included in this Appendix is the Matlab code to calculate the Gibbs Free energy functions of ferrite and austenite under paraequilbrium as a function of the temperature and the carbon content for a multicomponent system studied in chapters 3Kinetics of austenization during heating accounting for solute drag and Mn redistributionchapter.3 and 4Driving force for phase transformation of microalloyed steels under paraequilibrium conditionschapter.4.

The thermodynamic parameters of the multicomponent alloy were extracted from the Gibbs Energy System (GES) files of each participating phase, using SSOL4 Database, and merged together to build the thermodynamic parameters of the fictitious Z-C system using the equations presented in Appendix BDefinition of phase parameter for the Gibbs free energy calculationsappendix.B.

The Matlab functions for $G^{\alpha}(x_c, T)$ and $G^{\gamma}(x_c, T)$ are presented below.

Gibbs Free Energy of Ferrite

```
function [GmBCC,TCBCC] = GbccPE(XC,T)
%%%%%%%%SITE FRACTIONS MODULE%%%%%%%%%%%%%%
%XFE=VARIABLE
XMN=0.01724;
XSI=0.00535;
XMO=0.00157;
%XC=variable;
XFE=1-XMN-XSI-XMO-XC;
XVA=1-XC;
XN=0;
% YJs are site fractions defined as
%for ferrite q=3 and p=1
p=1;
q=3;
Y1 = XFE / (1 - XC - XN);
Y2 = XMN / (1 - XC - XN);
Y3 = XSI / (1 - XC - XN);
Y4 = XMO / (1 - XC - XN);
YC = (p/q)*(XC/(1 -XC - XN));
YVA = 1 - YC;
Y12 = Y1 - Y2;
Y13 = Y1 - Y3;
Y14 = Y1 - Y4;
Y23 = Y2 - Y3;
Y24 = Y2 - Y4;
Y34 = Y3 - Y4;
P=1E5; %Pa
%%%%%%%%%%% THERMODYNAMIC PARAMTERES OF MULTICOPONENT SYSTEM  %%%%%%%%%%
```

```
%%%%%%%%%%AND DEFINITION OF THERMODYNAMIC PARAMTER OF Z-C %%%%%%%%%%
%the order (in definition) is imporatant. We onlu need GPFEXXX, but to get
%that we need all the other ones defined.
%T and P must be defined
R=8.314; %J/Kmol
RT= R*T;
% BFEFCC   298.15
BFEFCC = +1 + 3.25236341E-11*P+3.36607808E-16*T*P; % 6000 N
% BFEBCC   298.15
BFEBCC = +1 + 2.80599565E-11*P+3.06481523E-16*T*P; % 6000 N
% DFEBCC   298.15
DFEBCC = +1*log(BFEBCC );  %6000 N
%CFEFCC   298.15
CFEFCC = +2.62285341E-11+2.71455808E-16*T; %6000 N
% AFEFCC   298.15
AFEFCC = +7.3097E-05*T;% 6000 N
% DFEFCC   298.15
DFEFCC = +1*log(BFEFCC ); % 6000 N
% CFEBCC   298.15
CFEBCC = +2.20949565E-11+2.41329523E-16*T;% 6000 N
%AFEBCC   298.15
AFEBCC = +2.3987E-05*T+1.2845E-08*T^2; %6000 N
VFEBCC = +7.042095E-06*exp(AFEBCC ); % 6000 N
% EFEBCC   298.15
EFEBCC = +1*log(CFEBCC ); % 6000 N
% XFEBCC   298.15
XFEBCC = +1*exp(.7874195*DFEBCC )-1; % 6000 N
%VFEFCC   298.15
VFEFCC = +6.688726E-06*exp(AFEFCC ); %6000 N
% EFEFCC   298.15
```

```
EFEFCC = +1*log(CFEFCC ); % 6000 N
% XFEFCC   298.15
XFEFCC = +1*exp(.8064454*DFEFCC )-1; %6000 N
% YFEBCC   298.15
YFEBCC = +VFEBCC *exp(-EFEBCC ); % 6000 N
% ZFEBCC   298.15
ZFEBCC = +1*log(XFEBCC ); % 6000 N
% YFEFCC   298.15
YFEFCC = +VFEFCC *exp(-EFEFCC ); % 6000 N
% ZFEFCC   298.15
ZFEFCC = +1*log(XFEFCC );% 6000 N
%GPFEBCC  298.15
GPFEBCC = +YFEBCC *exp(ZFEBCC ); %6000 N
%GPFEFCC  298.15
GPFEFCC= +YFEFCC *exp(ZFEFCC ); %6000 N
YLNY= Y1*log(Y1) + Y2*log(Y2)+ Y3*log(Y3) + Y4*log(Y4);
YLNYCVA = YC*log(YC) + YVA*log(YVA);
%%%%%%%%%G(BCC,X,C)%%%%%%%%%%
%  G(BCC_A2,FE:C;0)- 3 H298(GRAPHITE,C;0)-H298(BCC_A2,FE;0)
%298.15<T< 1811.00:
GF1= +271170.377 + 711.991*T - 96.4143*T*log(T) - 0.00581442*T^2
- 5.8927E-08 *T^3 + 7765159*T^(-1)-7.929E+08*T^(-2) + 3.6E+10*T^(-3);
%G(BCC_A2,MN:C;0)- 3 H298(GRAPHITE,C;0)-H298(CBCC_A12,MN;0) =
%298.15<T< 1519.00:
GF2=-50220.603 + 672.249*T - 96.3582*T*log(T) - 0.00876458*T^2
 + 7757627*T^(-1) -7.929E+08*T^(-2)+ 3.6E+10*T^(-3);
%G(BCC_A2,SI:C;0)- 3 H298(GRAPHITE,C;0)-H298(DIAMOND_A4,SI;0) =
%298.15<T< 1687.00:
GF3= +308782.068 + 551.250259*T-95.7317533*T*log(T) - 0.003329804*T^2
 - 3.552E-09*T^3 + 7864467*T^(-1) - 7.929E+08*T^(-2)+ 3.6E+10*T^(-3);
```

```
%G(BCC_A2,MO:C;0)- 3 H298(GRAPHITE,C;0)-H298(BCC_A2,MO;0) =
%298.15<T< 2896.00:
GF4=+271148.375+569.1097*T-96.46414*T*log(T) - 0.004860296*T^2
+ 5.66283E-07*T^3 + 7753612*T^(-1) -1.30927E-10*T^4 - 7.929E+08*T^(-2) + 3.6E+10*T
%L(BCC_A2,FE,MN:C;0)
LF12= +34052-23.467*T;
%L(BCC_A2,FE,SI:C;0)
LF13= +1000000-100*T;
%L(BCC_A2,FE,SI:C;1)
LF13o1= -900000;
%L(BCC_A2,FE,MO:C;0)
LF14= -1250000+667.7*T;
%L(BCC_A2,MN,SI:C;0)
LF23=  0.0;
GBCC_XC= Y1*GF1 + Y2*GF2 + Y3*GF3 + Y4*GF4 + RT*YLNY + (Y1*Y2)*LF12
+  (Y1*Y3)*(LF13 + Y13*LF13o1) + (Y1*Y4)*LF14;
%GPEBCC
%%%%%%%%%G(BCC,X,VA)%%%%%%%%%%
%G(BCC_A2,FE:VA;0)-H298(BCC_A2,FE;0) =
% 298.15<T< 1811.00:
GF1VA = +1225.7+124.134*T-23.5143*T*log(T)
- 0.00439752*T^2-5.8927E-08*T^3+77359*T^(-1) + GPFEBCC;
%GPFEBB function must be defined before!
%G(BCC_A2,MN:VA;0)-H298(CBCC_A12,MN;0) =
%298.15<T< 1519.00:
GF2VA= -3235.3+127.85*T-23.7*T*log(T)
- 0.00744271*T^2 + 60000*T^(-1);
%G(BCC_A2,SI:VA;0)-H298(DIAMOND_A4,SI;0) =
%298.15<T< 1687.00:
GF3VA = +38837.391+114.736859*T-22.8317533*T*log(T)
```

```
- 0.001912904*T^2-3.552E-09*T^3+176667*T^(-1);
%G(BCC_A2,MO:VA;0)-H298(BCC_A2,MO;0) =
%298.15<T< 2896.00:
GF4VA = -7746.302+131.9197*T-23.56414*T*log(T)
- 0.003443396*T^2+5.66283E-07*T^3+65812*T^(-1)-1.30927E-10*T^4;
%L(BCC_A2,FE,MN:VA;0) =
LF12VA = -2759+1.237*T;
% L(BCC_A2,FE,SI:VA;0) =
LF13VA = -153141.13+46.48*T;
% L(BCC_A2,FE,SI:VA;1) =
LF13o1VA =-92352;
% L(BCC_A2,FE,SI:VA;2) =
LF13o2VA = +62240;
%L(BCC_A2,FE,MO:VA;0) =
LF14VA = +36818-9.141*T;
%L(BCC_A2,FE,MO:VA;1) =
LF14o1VA = -362-5.724*T;
% LF4 MN MO
%L(BCC_A2,MN,SI:VA;0) =
LF23VA = -89620.7+2.94097*T;
%L(BCC_A2,MN,SI:VA;1) =
LF23o1VA = -7500;
%L(BCC_A2,MO,SI:VA;0) =
LF34VA = -11900.9+.66729*T;
%L(BCC_A2,MO,SI:VA;1) =
LF34o1VA = -78175.9;
%L(BCC_A2,FE,MN,SI:VA;0) =
LF123 = -97474;
GBCC_XVA = Y1*GF1VA + Y2*GF2VA + Y3*GF3VA + Y4*GF4VA
+ RT*YLNY + Y1*Y2*LF12VA + Y1*Y3*(LF13VA + Y13*LF13o1VA
```

```
+ (Y13^2)*LF13o2VA) + Y1*Y4*(LF14VA + Y14*LF14o1VA)
+ Y2*Y3*(LF23VA + Y23*LF23o1VA) + Y3*Y4*(LF34VA + Y34*LF34o1VA)
+ Y1*Y2*Y3*LF123;
%%%%%%%%%% L(BCC, X, C:VA, 0 ) %%%%%%%%%%
%L(BCC_A2,FE:C,VA;0) =
LF1CVA = -190*T;
LBCC_XCVA = Y1*LF1CVA;
%%%%%%%%%% L(BCC, X, C:VA, 1 ) %%%%%%%%%%
LBCC_XVA1 = 0;
%%%%%%%%%% BM(BCC, X, C, 0) %%%%%%%%
%BMAGN(BCC_A2,FE:C;0)
BMF1 = +2.22;
BMBCC_ZC = Y1*BMF1;
%%%%%%%%%% BM(BCC, X, VA, 0) %%%%%%%%
% BMAGN(BCC_A2,FE:VA;0) =
BMF1VA = +2.22;
%BMAGN(BCC_A2,MN:VA;0) =    298.15<T< 2000.00:
BMF2VA = -0.27;
BMBCC_ZVA = Y1*BMF1VA + Y2*BMF2VA;
%%%%%%%%%% BM(BCC, X, CVA, 0) %%%%%%%%
%%%%%%%%%% BM(BCC, X, CVA, 1) %%%%%%%%
%%%%%%%%%% TC(BCC, X, C, 0) %%%%%%%%
%TC(BCC_A2,FE:C;0)
TCF1 = +1043;
%TC(BCC_A2,FE,MO:C;0)
TCF14= +335;
%TC(BCC_A2,FE,MO:C;1)
TCF14o1= +526;
TCBCC_ZC = Y1*TCF1 + Y1*Y4* (TCF14 + Y14*TCF14o1);
%%%%%%%%%% TC(BCC, X, VA, 0) %%%%%%%%
```

```
%TC(BCC_A2,FE:VA;0)
TCF1VA = +1043;
%TC(BCC_A2,FE,MN:VA;0)
TCF12VA= +123;
%TC(BCC_A2,MN:VA;0) =    298.15<T< 2000.00:
TCF2VA = -580;
%TC(BCC_A2,FE,MO:VA;0)
TCF14VA= +335;
%TC(BCC_A2,FE,MO:VA;1)
TCF14o1VA= +526;
%TC(BCC_A2,FE,SI:VA;0)
TCF13VA =  0.0;
%TC(BCC_A2,FE,SI:VA;1)
TCF13o1VA= +504;
TCBCC_ZVA = Y1*TCF1VA + Y2*TCF2VA + Y1*Y4* (TCF14VA + Y14*TCF14o1VA)
+ Y1*Y3* (TCF13VA + Y13*TCF13o1VA);
%%%%%%%%%% TC(BCC, X, CVA, 0) %%%%%%%%
%%%%%%%%%% TC(BCC, X, CVA, 1) %%%%%%%%
%%%%%%%CALCULATIONS%%%%%%
%%%Curie Temperature%%%%%%
TCBCC = YC*TCBCC_ZC + YVA*TCBCC_ZVA ;
BMAGBCC = YC*BMBCC_ZC + YVA*BMBCC_ZVA ;
TAO=T/TCBCC;
if T<TCBCC
fta= +1-.905299383*TAO^(-1)-.153008346*TAO^3
-.00680037095*TAO^9 -.00153008346*TAO^15;
end
if T>TCBCC
fta=-.0641731208*TAO^(-5)-.00203724193*TAO^(-15)
-4.27820805E-04*TAO^(-25);
```

```
end
BMAGBCCcor=BMAGBCC/(-1);
MAGBCC= RT*log(BMAGBCC + 1 )* fta;
%%%%%%%EXPANADED FORM FOR GIBBS FREE ENERGY OF FERRITE Z-C %%%%%%%%%%
GmBCC = YC*GBCC_XC + YVA*GBCC_XVA + YC*YVA*LBCC_XCVA + 3*RT*YLNYCVA + MAGBCC;
```

Gibbs Free Energy of Austenite

```
function [GmFCC,TCFCC] = GfccPE(XC,T)
%%%%%%%%SITE FRACTIONS MODULE%%%%%%%%%%%%%%%
%%X in mole fractions
%XFE=variable;
XMN=0.01724;
XSI=0.00535;
XMO=0.00157;
%XC=variable;
XFE=1-XMN-XSI-XMO-XC;
XVA=1-XC;
XN=0;
% YJs are site fractions defined as
%for ferrite q=3 and p=1
p=1;
q=1;
Y1 = XFE / (1 - XC - XN);
Y2 = XMN / (1 - XC - XN);
Y3 = XSI / (1 - XC - XN);
Y4 = XMO / (1 - XC - XN);
YC = (p/q)*(XC/(1 -XC - XN));
YVA = 1 - YC;
Y12 = Y1 - Y2;
Y13 = Y1 - Y3;
Y14 = Y1 - Y4;
Y23 = Y2 - Y3;
Y24 = Y2 - Y4;
Y34 = Y3 - Y4;
%T=variable; %K
P=1E5; %Pa
```

```
%%%%%%%%%%% THERMODYNAMIC PARAMTERES OF MULTICOPONENT SYSTEM  %%%%%%%%%%
%%%%%%%%%%AND DEFINITION OF THERMODYNAMIC PARAMTER OF Z-C %%%%%%%%%
%the order (in definition) is imporatant. We only need GPFEXXX, but to get
%that we need all the other ones defined.
%T and P must be defined
R=8.314; %J/Kmol
RT= R*T;
% BFEFCC   298.15
BFEFCC = +1 + 3.25236341E-11*P+3.36607808E-16*T*P; % 6000 N
% BFEBCC   298.15
BFEBCC = +1 + 2.80599565E-11*P+3.06481523E-16*T*P; % 6000 N
% DFEBCC   298.15
DFEBCC = +1*log(BFEBCC );  %6000 N
%CFEFCC   298.15
CFEFCC = +2.62285341E-11+2.71455808E-16*T; %6000 N
% AFEFCC   298.15
AFEFCC = +7.3097E-05*T;% 6000 N
% DFEFCC   298.15
DFEFCC = +1*log(BFEFCC ); % 6000 N
% CFEBCC   298.15
CFEBCC = +2.20949565E-11+2.41329523E-16*T;% 6000 N
%AFEBCC   298.15
AFEBCC = +2.3987E-05*T+1.2845E-08*T^2; %6000 N
VFEBCC = +7.042095E-06*exp(AFEBCC ); % 6000 N
% EFEBCC   298.15
EFEBCC = +1*log(CFEBCC ); % 6000 N
% XFEBCC   298.15
XFEBCC = +1*exp(.7874195*DFEBCC )-1; % 6000 N
%VFEFCC   298.15
VFEFCC = +6.688726E-06*exp(AFEFCC ); %6000 N
```

```
% EFEFCC   298.15
EFEFCC = +1*log(CFEFCC ); % 6000 N
% XFEFCC   298.15
XFEFCC = +1*exp(.8064454*DFEFCC )-1; %6000 N
% YFEBCC   298.15
YFEBCC = +VFEBCC *exp(-EFEBCC ); % 6000 N
% ZFEBCC   298.15
ZFEBCC = +1*log(XFEBCC ); % 6000 N
% YFEFCC   298.15
YFEFCC = +VFEFCC *exp(-EFEFCC ); % 6000 N
% ZFEFCC   298.15
ZFEFCC = +1*log(XFEFCC );% 6000 N
%GPFEBCC  298.15
GPFEBCC = +YFEBCC *exp(ZFEBCC ); %6000 N
%GPFEFCC  298.15
GPFEFCC= +YFEFCC *exp(ZFEFCC ); %6000 N
%%%%%%%%%%
YLNY= Y1*log(Y1) + Y2*log(Y2)+ Y3*log(Y3) + Y4*log(Y4);
YLNYCVA = YC*log(YC) + YVA*log(YVA);
%%%%%%%%%%%%
%%%%%%%%%G(fcc,X,C)%%%%%%%%%
%G(FCC_A1,FE:C;0)-H298(GRAPHITE,C;0)-H298(BCC_A2,FE;0) =
%298.15<T< 1811.00:
GA1 = +59601.859 + 287.269*T - 48.9643*T*log(T) - 0.00422982*T^2
- 5.8927E-08*T^3 + 2639959*T^(-1)- 2.643E+08*T^(-2) + 1.2E+10*T^(-3);
%G(FCC_A1,MN:C;0)-H298(GRAPHITE,C;0)-H298(CBCC_A12,MN;0) =
%298.15<T< 1519.00:
GA2 = -24981.721+316.05*T-47.7582*T*log(T) - 0.00781998*T^2
+ 2632427*T^(-1)- 2.643E+08*T^(-2)+ 1.2E+10*T^(-3);
%G(FCC_A1,SI:C;0)-H298(GRAPHITE,C;0)-H298(DIAMOND_A4,SI;0) =
```

```
%298.15<T< 1687.00:
GA3 = -46041.05 + 346.657259*T - 47.1317533*T*log(T)- 0.002385204*T^2
-3.552E-09*T^3+2739267*T^(-1)-2.643E+08*T^(-2) +1.2E+10*T^(-3);
%G(FCC_A1,MO:C;0)-H298(GRAPHITE,C;0)-H298(BCC_A2,MO;0) =
%298.15<T< 2896.00:
GA4 = -32614.743+294.3497*T-47.86414*T*log(T) - 0.003915696*T^2
+ 5.66283E-07*T^3 + 1878412*T^(-1) -1.30927E-10*T^4-2.643E+08*T^(-2)+1.2E+10*T^(-3
%L(FCC_A1,FE,MN:C;0)
LA12 = +34052-23.467*T;
% L(FCC_A1,FE,MO:C;0)
LA14 = +6000;
%L(FCC_A1,FE,SI:C;0)
LA13 = +226100-34.25*T;
% L(FCC_A1,FE,SI:C;1)
LA13o1= -202400;
%L(FCC_A1,MN,SI:C;0)
LA23 =  0.0;
GFCC_XC= Y1*GA1 + Y2*GA2 + Y3*GA3 + Y4*GA4 + RT*YLNY + (Y1*Y2)*LA12
+  (Y1*Y3)*(LA13 + Y13*LA13o1) + (Y1*Y4)*LA14;
%%%%%%%%%G(FCC,X,VA)%%%%%%%%%
%G(FCC_A1,FE:VA;0)-H298(BCC_A2,FE;0) =
%298.15<T< 1811.00:
GA1VA = -236.7+132.416*T - 24.6643*T*log(T) - 0.00375752*T^2
- 5.8927E-08*T^3+77359*T^(-1)+GPFEFCC;
%G(FCC_A1,MN:VA;0)-H298(CBCC_A12,MN;0) =
%298.15<T< 1519.00:
GA2VA = -3439.3+131.884*T - 24.5177*T*log(T)- 0.006*T^2 + 69600*T^(-1);
%G(FCC_A1,SI:VA;0)-H298(DIAMOND_A4,SI;0) =
%298.15<T< 1687.00:
GA3VA = +42837.391+115.436859*T-22.8317533*T*log(T)
```

```
- 0.001912904*T^2-3.552E-09*T^3+176667*T^(-1);
%G(FCC_A1,MO:VA;0)-H298(BCC_A2,MO;0) =
%298.15<T< 2896.00:
GA4VA = +7453.698+132.5497*T-23.56414*T*log(T)- 0.003443396*T^2
+ 5.66283E-07*T^3 + 65812*T^(-1)- 1.30927E-10*T^4;
%L(FCC_A1,FE,MN:VA;0)
LA12VA = -7762+3.865*T;
%L(FCC_A1,FE,MN:VA;1)
LA12o1VA = -259;
%L(FCC_A1,FE,MN,SI:VA;0)
LA123VA= -56655-55.613*T;
%L(FCC_A1,FE,MO:VA;0)
LA14VA= +28347-17.691*T;
%L(FCC_A1,FE,SI:VA;0)
LA13VA= -125247.7+41.166*T;
%L(FCC_A1,FE,SI:VA;1)
LA13o1VA= -142707.6;
%L(FCC_A1,FE,SI:VA;2)
LA13o2VA= +89907.3;
%L(FCC_A1,MN,SI:VA;0)
LA23VA= -95600+2.94097*T;
%L(FCC_A1,MN,SI:VA;1)
LA23o1VA= -7500;
GFCC_XVA = Y1*GA1VA + Y2*GA2VA + Y3*GA3VA + Y4*GA4VA + RT*YLNY
+ Y1*Y2*(LA12VA + (Y1-Y2)*LA12o1VA) + Y1*Y3*(LA13VA + Y13*LA13o1VA
 + (Y13^2)*LA13o2VA) + Y1*Y4*LA14VA  + Y2*Y3*(LA23VA + Y23*LA23o1VA)
  + Y1*Y2*Y3*LA123VA;
%%%%%%%%%% L(FCC, X, C:VA, 0 ) %%%%%%%%%%
%L(FCC_A1,MN:C,VA;0)
LA2CVA = -43433;
```

```
%L(FCC_A1,FE:C,VA;0)
LA1CVA = -34671;
%L(FCC_A1,MO:C,VA;0)
LA4CVA = -41300;
%L(FCC_A1,SI:C,VA;0)
LA3CVA =  0.0;
LFCC_XCVA = Y1*LA1CVA + Y2*LA2CVA + Y4*LA4CVA ;
%%%%%%%%% L(BCC, X, C:VA, 1 ) %%%%%%%%%%
%nothing was defined here.
LFCC_XVA1 = 0;
%%%%%%%%%% BM(FCC, X, C, 0) %%%%%%%%
%BMAGN(FCC_A1,FE:C;0)
BMA1 = -2.1;
BMFCC_ZC = Y1*BMA1;
%%%%%%%%%% BMFCCBCC, X, VA, 0) %%%%%%%%
%BMAGN(FCC_A1,FE:VA;0)
BMA1VA = -2.1;
%BMAGN(FCC_A1,MN:VA;0) =    298.15<T< 2000.00:
BMA2VA = -1.86;
BMFCC_ZVA = Y1*BMA1VA + Y2*BMA2VA;
%%%%%%%%%% BM(FCC, X, CVA, 0) %%%%%%%%
%%%%%%%%%% BM(FCC, X, CVA, 1) %%%%%%%%
%%%%%%%%%% TC(FCC, X, C, 0) %%%%%%%%
%TC(FCC_A1,FE:C;0)
TCA1 = -201;
TCFCC_ZC = Y1*TCA1;
%%%%%%%%%% TC(FCC, X, VA, 0) %%%%%%%%
%TC(FCC_A1,FE:VA;0)
TCA1VA= -201;
%TC(FCC_A1,MN:VA;0) =    298.15<T< 2000.00:
```

```
TCA2VA=-1620;
%TC(FCC_A1,FE,MN:VA;0)
TCA12VA = -2282;
%TC(FCC_A1,FE,MN:VA;1)
TCA12o1VA= -2068;
%TC(FCC_A1,FE,MN,SI:VA;0)
TCA123VA = +13854;
TCFCC_ZVA = Y1*TCA1VA + Y2*TCA2VA
+ Y1*Y2* (TCA12VA + Y12*TCA12o1VA)+ Y1*Y3*Y2*TCA123VA;
%%%%%%%CALCULATIONS%%%%%%
%%%Curie Temperature%%%%%%
TCFCC = YC*TCFCC_ZC + YVA*TCFCC_ZVA ;
BMAGFCC = YC*BMFCC_ZC + YVA*BMFCC_ZVA ;
TAO=T/TCFCC;
if T<TCFCC
fta= +1-.860338755*TAO^(-1)- 0.17449124*TAO^3
-.00775516624*TAO^9 -.0017449124*TAO^15;
end
if T>TCFCC
fta= -.0426902268*TAO^(-5)-.0013552453*TAO^(-15) -2.84601512E-04*TAO^(-25);
end
BMAGFCCcor=BMAGFCC/(-3);
MAGFCC= RT*log(BMAGFCCcor + 1 )* fta;
%%%%%%%EXPANADED FORM FOR GIBBS FREE ENERGY OF AUSTENITE Z-C %%%%%%%%%%
GmFCC = YC*GFCC_XC + YVA*GFCC_XVA + YC*YVA*LFCC_XCVA + RT*YLNYCVA + MAGFCC;
```

The general form of each phase thermodynamic parameter utilized in the calculation of the molar Gibbs free energy of the system Z-C are presented below.

Each term, is defined by the combination of the site fraction, y, of substituional elements (p, o, l) and their respective reference value obtained from the thermodynamic data base.

$$G^{0,j}_{\mathrm{Z:C}} = \sum y_{\mathrm{p}} G^{0,j}_{\mathrm{p:C}} + RT \sum y_{\mathrm{p}} \ln y_{\mathrm{p}} + \sum \sum_{p \neq o} y_{\mathrm{p}} y_{\mathrm{o}} (L^{0,j}_{\mathrm{p:o:C}} + (y_{\mathrm{p}} - y_{\mathrm{o}}) L^{1,j}_{\mathrm{p:o:C}}) + \sum \sum \sum_{p \neq o \neq l} y_{\mathrm{p}} y_{\mathrm{o}} y_{\mathrm{l}} L^{0,j}_{\mathrm{p:o:l:C}} \quad \text{(C.1)}$$

$$G^{0,j}_{\mathrm{Z:VA}} = \sum y_{\mathrm{p}} G^{0,j}_{\mathrm{p:VA}} + RT \sum y_{\mathrm{p}} \ln y_{\mathrm{p}} + \sum \sum_{p \neq o} y_{\mathrm{p}} y_{\mathrm{o}} (L^{0,j}_{\mathrm{p:o:VA}} + (y_{\mathrm{p}} - y_{\mathrm{o}}) L^{1,j}_{\mathrm{p:o:VA}}) + \sum \sum \sum_{p \neq o \neq l} y_{\mathrm{p}} y_{\mathrm{o}} y_{\mathrm{l}} L^{0,j}_{\mathrm{p:o:l:VA}} \quad \text{(C.2)}$$

$$L^{0,j}_{\mathrm{Z:C:VA}} = \sum y_{\mathrm{p}} L^{0,j}_{\mathrm{p:C:VA}} + \sum \sum_{p \neq o} y_{\mathrm{p}} y_{\mathrm{o}} L^{0,j}_{\mathrm{p:o:C:VA}} \quad \text{(C.3)}$$

$$L^{1,j}_{\mathrm{Z:C:VA}} = \sum y_{\mathrm{p}} L^{1,j}_{\mathrm{p:C:VA}} + \sum \sum_{p \neq o} y_{\mathrm{p}} y_{\mathrm{o}} (y_{\mathrm{p}} - y_{\mathrm{o}}) L^{0,j}_{\mathrm{p:o:C:VA}} \quad \text{(C.4)}$$

$$\beta^{0,j}_{\text{Z:C}} = \sum y_{\text{p}} \beta^{0,j}_{\text{p:C}} + \sum \sum_{p \neq o} y_{\text{p}} y_{\text{o}} (\beta^{0,j}_{\text{p:o:C}} + (y_{\text{p}} - y_{\text{o}}) \beta^{1,j}_{\text{p:o:C}}) + \sum \sum \sum_{p \neq o \neq l} y_{\text{p}} y_{\text{o}} y_{\text{l}} \beta^{0,j}_{\text{p:o:l:C}} \quad \text{(C.5)}$$

$$\beta^{0,j}_{\text{Z:VA}} = \sum y_{\text{p}} \beta^{0,j}_{\text{p:VA}} + \sum \sum_{p \neq o} y_{\text{p}} y_{\text{o}} (\beta^{0,j}_{\text{p:o:VA}} + (y_{\text{p}} - y_{\text{o}}) \beta^{1,j}_{\text{p:o:VA}}) + \sum \sum \sum_{p \neq o \neq l} y_{\text{p}} y_{\text{o}} y_{\text{l}} \beta^{0,j}_{\text{p:o:l:VA}} \quad \text{(C.6)}$$

$$\beta^{0,j}_{\text{Z:C:VA}} = \sum y_{\text{p}} \beta^{0,j}_{\text{p:C:VA}} + \sum \sum_{p \neq o} y_{\text{p}} y_{\text{o}} \beta^{0,j}_{\text{p:o:C:VA}} \quad \text{(C.7)}$$

$$\beta^{1,j}_{\text{Z:C:VA}} = \sum y_{\text{p}} \beta^{1,j}_{\text{p:C:VA}} + \sum \sum_{p \neq o} y_{\text{p}} y_{\text{o}} (y_{\text{p}} - y_{\text{o}}) \beta^{1,j}_{\text{p:o:C:VA}} \quad \text{(C.8)}$$

$$Tc^{0,j}_{\text{Z:C}} = \sum y_{\text{p}} Tc^{0,j}_{\text{p:C}} + \sum \sum_{p \neq o} y_{\text{p}} y_{\text{o}} (Tc^{0,j}_{\text{p:o:C}} + (y_{\text{p}} - y_{\text{o}}) Tc^{1,j}_{\text{p:o:C}}) + \sum \sum \sum_{p \neq o \neq l} y_{\text{p}} y_{\text{o}} y_{\text{l}} Tc^{0,j}_{\text{p:o:l:C}} \quad \text{(C.9)}$$

$$Tc^{0,j}_{\text{Z:VA}} = \sum y_{\text{p}} Tc^{0,j}_{\text{p:VA}} + \sum \sum_{p \neq o} y_{\text{p}} y_{\text{o}} (Tc^{0,j}_{\text{p:o:VA}} + (y_{\text{p}} - y_{\text{o}}) Tc^{1,j}_{\text{p:o:VA}}) + \sum \sum \sum_{p \neq o \neq l} y_{\text{p}} y_{\text{o}} y_{\text{l}} Tc^{0,j}_{\text{p:o:l:VA}} \quad \text{(C.10)}$$

$$Tc^{0,j}_{\text{Z:C:VA}} = \sum y_{\text{p}} Tc^{0,j}_{\text{p:C:VA}} + \sum \sum_{p \neq o} y_{\text{p}} y_{\text{o}} Tc^{0,j}_{\text{p:o:C:VA}} \quad \text{(C.11)}$$

$$Tc^{1,j}_{\text{Z:C:VA}} = \sum y_{\text{p}} Tc^{1,j}_{\text{p:C:VA}} + \sum \sum_{p \neq o} y_{\text{p}} y_{\text{o}} (y_{\text{p}} - y_{\text{o}}) Tc^{1,j}_{\text{p:o:C:VA}} \quad \text{(C.12)}$$

Appendix D

Derivation of the solute drag model

If the potential well of Mn inside the interface can be modeled with a triangular potential like in Figure D.1Schematics of the interface and the potential well proposed by reference by the solute drag modelfigure.caption.60, where $2\Delta E = \mu_{\gamma}^{Mn} - \mu_{\alpha}^{Mn}$ is the difference in chemical potential of the substitutional atoms in ferrite and austenite, E_0 is the binding energy, and b is half of interface thickness. Then, the variation of μ^{Mn} across the interface will derive in a driving force for diffusion.

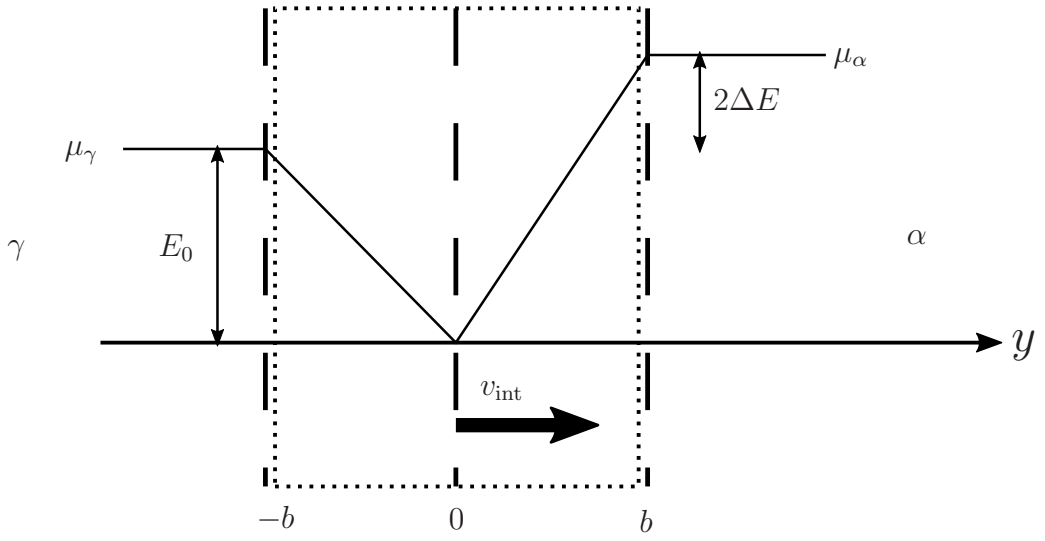

Figure D.1: Schematics of the interface and the potential well proposed by reference by the solute drag model

Then the governing equation for diffusion of alloying elements inside the migrating interface with a quasi-steady interface velocity (v_{int}) is given by:

$$\frac{d}{dx}[D^b \frac{dx}{dy} + \frac{D^b x}{RT} \frac{dE}{dy} + v_{int}\ x] = 0 \tag{D.1}$$

where x is the concentration of alloying elements, D^b is the boundary diffusion coefficient, R is the gas constant and T the temperature. The solution to equation D.1Derivation of the solute drag modelequation.D.0.1 in terms of three dimensionless parameters and one dimensionless variable is expressed below [104].

$$P = \frac{v_{\text{int}}\ 2\ b}{D^b} \tag{D.2}$$

$$a = \frac{D^b\ (\Delta E - E_0)}{RT\ v_{\text{int}}\ 2\ b} \tag{D.3}$$

$$b = \frac{D^b \ (\Delta E + E_0)}{RT \ v_{\text{int}} \ 2 \ b} \tag{D.4}$$

$$Y = \frac{y}{b} \tag{D.5}$$

$$\frac{x}{x_0} = 1 \ \text{ for } Y < -1 \tag{D.6}$$

$$\frac{x}{x_0} = \frac{1 + a \ e^{(-P(1+a)(Y+1))}}{1+a} \ \text{ for } -1 < Y < 0 \tag{D.7}$$

$$\frac{x}{x_0} = \frac{1 + (\frac{a(1+b)e^{(-P(1+a))}}{1+a} + \frac{b-a}{1+a})e^{(-P(1+b)Y)}}{1+b} \ \text{ for } 0 < Y < 1 \tag{D.8}$$

$$\frac{x}{x_0} = 1 + e^{(-PY)} \ (\frac{ae^{(-P(a+b+1))}}{1+a} + \frac{(b-a)e^{(-Pb)}}{(1+a)(1+b)} - \frac{be^P}{1+b}) \ \text{ for } Y > 1 \tag{D.9}$$

And ultimately, once the concentration profile is obtained the solute drag effect of Mn can be calculated using Cahn's equation [102]:

$$G^{diff} = \int_{-b}^{b} (x - x_0) \ \frac{dE}{dy} dy \tag{D.10}$$

Appendix E

Modification of the solute drag model

In this appendix, the derivation of equation 3.5Asymptotic Regimes of the Solute Drag Modelequation.3.4.5 in Chapter 3Kinetics of austenization during heating accounting for solute drag and Mn redistributionchapter.3, that modifies the ΔE term in the solute drag model, is presented. Equation 3.5Asymptotic Regimes of the Solute Drag Modelequation.3.4.5 was proposed due to the similarities to the heat transfer problem on a semi-infinite solid with constant surface convection. The closed form solution for the heat transfer problem can be expressed by the following equation [146]:

$$\frac{T(y,t)-T_i}{T_\infty - T_i} = \text{erfc}(\frac{y}{2\sqrt{\alpha t}}) - [\exp{(\frac{hy}{k} + \frac{h^2\alpha t}{k^2})}][\text{erfc}(\frac{y}{2\sqrt{\alpha t}} + \frac{h\sqrt{\alpha t}}{k})] \quad \text{(E.1)}$$

Where T_∞ and T_i are the fluid and the slab temperatures (defining the boundary conditions) respectively, h is the convection heat transfer coefficient, k is the thermal conductivity, and α the thermal diffusivity

In the present work, the solution to the diffusion problem is be expressed by:

$$\frac{C(y,t)-C_i}{C_\infty - C_i} = \text{erfc}(\frac{y}{2\sqrt{Dt}}) - [\exp{(\frac{hy}{D} + \frac{h^2 Dt}{D^2})}][\text{erfc}(\frac{y}{2\sqrt{Dt}} + \frac{h\sqrt{Dt}}{D})] \quad \text{(E.2)}$$

For the case of $y = 0$, analyzing the concentration at the α/interface, equation E.2Modification of the solute drag modelequation.E.0.2 yields

$$\Lambda = \frac{C(y,t)-C_i}{C_\infty - C_i} = 1 - [\exp{(\frac{h^2 Dt}{D^2})}][\text{erfc}(\frac{h\sqrt{Dt}}{D})] \quad \text{(E.3)}$$

where h, in the heat transfer case, represents the convection heat transfer coefficientdefined by the heat flux, q over the difference in temperature ΔT. Similarly, for the diffusion case, $h = J/\Delta C$, is defined by the flux of atoms across the interface over the difference in concentration.

With $J = D^b \frac{dC}{dx} = D^b \frac{\Delta C}{\delta}$, the value of h can be approximated as $h = D^b/\delta$

On the other hand, approximating the value of $t = L_c/v_{\text{int}}$ and using the diffusivity values of Mn in Austenite $D = D^\gamma_{\text{Mn}}$ equation E.3Modification of the solute drag modelequation.E.0.3 can be redefined as 3.5Asymptotic Regimes of the Solute Drag Modelequation.3.4.5:

$$\Lambda = 1 - [\exp(k_a)\ \text{erfc}(\sqrt{k_a})] \quad \text{(E.4)}$$

where the factor k_a in Chapter 3Kinetics of austenization during heating accounting for solute drag and Mn redistributionchapter.3 is defined by:

$$k_a = \frac{h^2\ D^\gamma_{\text{Mn}}\ t}{(D^\gamma_{\text{Mn}})^2}\ (\beta)^2 = \frac{(D^b)^2\ L_c\ (\beta)^2}{(\delta)^2\ D^\gamma_{\text{Mn}}} \quad \text{(E.5)}$$

Where β the adjustable parameter.